

Tarjei Vefring Stordal

Particle Deposition From Geothermal Supercritical Steam

Master's thesis in Mechanical Engineering

Supervisor: Erling Næss

Co-supervisor: Silje Bordvik

June 2021

Tarjei Vefring Stordal

Particle Deposition From Geothermal Supercritical Steam

Master's thesis in Mechanical Engineering
Supervisor: Erling Næss
Co-supervisor: Silje Bordvik
June 2021

Norwegian University of Science and Technology
Faculty of Engineering
Department of Energy and Process Engineering



Masteravtale

Background and objective

Geothermal energy represents a source of renewable energy with a vast exploiting potential for heating and/or energy production. Recently, heat extraction from superheated or supercritical water has been focused. Supercritical water from several kilometers deep water-bearing reservoirs is transported to the surface, where the high enthalpy steam is converted to electrical energy using steam turbines. This technology is in the development stage, and the potential is significant. Norway has the potential of taking a leading role in the international geothermal industry, due to the country's notable competence in geology and drilling technology. The thesis is a part of an ongoing study by the Department of Energy and Process Engineering at NTNU in cooperation with Equinor. The project is supported by The Research Council of Norway. The main objective is to establish numerical tools for particle transport and deposition using commercial software. The following tasks are to be considered:

1. A numerical model for particle transport to a solid wall in a turbulent gas flow field is to be established. Body forces and fluid-particle interaction shall be considered. The flow and temperature fields shall be verified against available literature data, and the impact of the implemented body forces shall be evaluated.
2. Calculations using the numerical model shall be performed, whereas the conditions shall be determined in cooperation with the Department. The results shall be presented and discussed, and they shall be validated with available data.
3. Based on points 1 and 2, the model shall be adapted to a particle-laden high pressure and high-temperature steam flow condition with an emphasis on nano-sized silica particles and in relevant flow geometries. The results shall be presented and discussed.
4. An experimental program for the investigation of the generation and subsequent deposition of nano-sized silica particles from superheated steam is being planned. The candidate shall participate in selected relevant activities during experiment design, execution, or analysis of the obtained results.
5. Suggestions for further work shall be made.

Abstract

Heat extraction from deep hot geothermal wells may lead to an order of magnitude higher power output than conventional geothermal wells (Fridleifsson et al. 2003). However, such energy potential cannot be exploited with current technologies. The reason for this is that precipitation of submicron-sized particles of SiO_2 from depressurised superheated water vapour is especially fast in the gaseous phase, resulting in subsequent high rates of deposition and scaling onto pipe surfaces and process equipment, which is problematic.

Numerical and experimental methods are conducted to explore dominant submicron particle transport mechanisms and to quantify deposition rates from superheated and supercritical water vapour in turbulent channel flows. In this work, a numerical model (PARTICLE) is established in the commercial software ANSYS® Fluent 20.2 for submicron particle tracking with the use of user-defined functions (UDFs). A boundary layer model and correction terms to the model for the instantaneous turbulent velocity fluctuations are implemented in the PARTICLE model to address spurious results in the default model in ANSYS Fluent. By employing the Reynolds stress equation model (RSM) for the turbulence mean flow simulation, the PARTICLE model was validated and showed very good agreements with experimental, numerical and empirical results in ambient conditions of air. The established PARTICLE model facilitates improved submicron particle deposition simulations using ANSYS Fluent. Subsequent application of the PARTICLE model at the geothermal conditions revealed overestimated diffusion rates for submicron particles compared to empirical correlations. Therefore, further validation of the employed models and the predicted concentration profiles in the geothermal conditions is emphasised.

Contributions to an experimental investigation on the precipitation, agglomeration and deposition of depressurised superheated and supercritical water vapour supersaturated with silicic acid were made. A calculation procedure is proposed to compare the experimental and numerical deposition results by including a particle size distribution from the numerical model of Bordvik, Næss et al. (2021). Validation with the results from this experimental investigation is recommended, as possible deviations from the numerical predictions might be related to repulsive wall bounding forces.

Sammendrag

Varmeutvinning fra dype varme geotermiske brønner kan føre til en størrelsesorden høyere effekt sammenlignet med konvensjonelle geotermiske brønner (Fridleifsson et al. 2003). Et slikt energipotensial kan imidlertid ikke utnyttes med dagens teknologi. Årsaken til dette er den spesielt raske utfelling av SiO_2 -partikler av submikron størrelse fra trykkavlastet overopphetet vanndamp, noe som resulterer i påfølgende høye avsetningshastigheter og beleggdannelse på røroverflater og prosessutstyr, noe som er problematisk.

Følgende arbeid består av numeriske og eksperimentelle metoder for å utforske dominerende transportmekanismer for partikler av submikron størrelse og for å kvantifisere avsetningshastigheter fra overopphetet og superkritisk vanndamp i turbulente strømningskanaler. I dette arbeidet er det etablert en numerisk modell (PARTICLE) i den kommersielle programvaren ANSYS[®] Fluent 20.2 for banefølgning av submikronpartikler ved bruk av brukerdefinerte funksjoner (UDF). En grenseskikt-modell og korreksjoner til modellen for øyeblikkelige turbulente hastighetssvingninger er implementert i PARTICLE-modellen for å adressere feil-genererte resultater i standardmodellen i ANSYS Fluent. Ved å bruke Reynolds stressligningsmodell (RSM) for hastighetsfeltet og de gjennomsnittlige turbulente hastighetssvingningene i en strømningskanal, ble PARTICLE-modellen ble validert og viste meget godt samsvar med eksperimentelle, numeriske og empiriske resultater fra litteraturen ved atmosfæriske luftforhold. Den etablerte PARTICLE-modellen muliggjør forbedrede simuleringer av submikron partikkelavsetninger ved bruk av ANSYS Fluent. Anvendelsen av PARTICLE-modellen ved geotermiske forhold avslørte overvurderte diffusjonshastigheter for submikronpartikler sammenlignet med empiriske korrelasjoner. Derfor blir ytterligere validering av de benyttede modellene og de resulterende konsentrasjonsprofilene i de geotermiske forholdene anbefalt for videre arbeid.

Bidrag til en eksperimentell studie av utfelling, agglomerering og avsetning av trykkreduert overopphetet og superkritisk vanndamp overmettet med ortokiselsyre er gjennomført. Det foreslås en beregningsprosedyre for å sammenligne eksperimentelle og numeriske resultater av avsetningshastighet ved å inkludere en partikkelstørrelsesfordeling fra den numeriske modellen til Bordvik, Næss et al. (2021). Validering med resultatene fra denne eksperimentelle studien anbefales, da mulige avvik fra de numeriske prediksjonene kan være relatert til frastøtende krefter på veggen.

Acknowledgements

I would like to express my deepest gratitude to my academic supervisor, Prof. Erling Næss, for continuous support, enthusiasm and guidance in forming and completing this master's thesis. Sincere gratitude to my co-supervisor, PhD Candidate Silje Bordvik, for the helpful support and discussions on the experimental investigation and for completing this thesis.

A sincere thanks also go to Morten Tjelta at IFE. Finally, I would like to thank my family and friends for being helpful and supportive during my time studying at the Norwegian University of Science and Technology.

Nomenclature

Latin Letters

\dot{m}	mass flow	kg/s
A	area	m ²
A	near-wall model constant	-
c	particle concentration	kg/m
C_μ	closure coefficient	-
C_c	Cunningham correction factor	-
C_D	drag coefficient	-
C_L	Lagrangian time scale constant	-
$C_l, A_\mu, A_\varepsilon$	constants in the enhanced wall treatment	-
c_p	constant pressure specific heat capacity	J/(kgK)
D	diffusion coefficient	m ² /s
d_h	hydraulic diameter	m
d_p	particle diameter	m
D_T	turbulent diffusion	m ² /s
d_{ij}	deformation rate tensor in eq. for Saffman lift force	1/s
e	internal energy per unit mass	J/kg
e	the position of the displaced origin in the roughness model	m
F_B	Brownian force	N
F_D	steady state drag force	N
F_i	force on a particle	N
F_L	lift force	N
F_{vdW}	van der Waals force	N
g	gravitational constant	m/s ²
h	channel height	-
h_N	convective mass transfer film coefficient	m/s
h_{htc}	heat transfer coefficient	W/(m ² K)

k	roughness height	m
k	turbulent kinetic energy	m^2/s^2
k_{th}	thermal conductivity	$\text{W}/(\text{mK})$
Kn	Knudsen number	-
L	length scale	m
l_μ, l_ε	length scales	m
L_e	eddy length scale	m
M	number of particles	-
m	mass	kg
Nu	Nusselt number	-
Pr	Prandtl number	-
q	heat flux	$\text{J}/(\text{sm}^2)$
R	specific gas constant	$\text{J}/(\text{kgK})$
r	radius	m
Re	Reynolds number	-
Re_τ	shear Reynolds number	-
Re_p	particle Reynolds number	-
Re_t	turbulent Reynolds number	-
Sc	Schmidt number	-
Sh	Sherwood number	-
Stk	Stokes number	-
T	Temperature	K
t	time	s
T_L	particle Lagrangian integral time scale	s
t_{cross}	particle crossing time	s
t_{int}	eddy interaction time	s
u	velocity	m/s
u^+	dimensionless velocity	-
u_τ	friction velocity	m/s
v	particle velocity	m/s
y	distance from the wall	m
y^+	dimensionless wall distance	-
V_d	deposition velocity	m/s
V_d^+	dimensionless deposition velocity	-

Greek Letters

α	thermal diffusivity	m^2/s
ϵ	turbulent dissipation rate	m^2/s^3
λ	mean free path	m
μ	dynamic viscosity	$\text{kg}/(\text{ms})$
μ_t	turbulent viscosity	$\text{kg}/(\text{ms})$
ν	kinematic viscosity	m^2/s
ω	specific dissipation	$1/\text{s}$
ρ	density	kg/m^3
σ_{ij}	stress tensor	N/m^2
σ_k	standard deviation of the roughness height	m
τ_e	eddy life time	s
τ_p	particle relaxation time	s
τ_w	wall shear stress	N/m^2
ζ_i	normally distributed random number	-
ζ_u	uniformly distributed random number	-
τ_p^+	dimensionless particle relaxation time	-

Subscripts

max	maximum value
min	minimum value
w,wall	wall
f	fluid
inj	injection
p	particle
ts	test section

Superscripts

'	fluctuating value
+	dimensionless variable
-	mean
\sim	normalised variable

Abbreviations

AR	aspect ratio
CFD	computational fluid dynamics
DLVO	theory of particle interactions named after Derjaguin and Landau, Verwey and Overbeek

DNS	direct numerical simulation
DPM	discrete phase model
DRW	discrete random walk
IDDP	Iceland Deep Drilling Project
MC-DRW	The conventional-DRW results from Mofakham and Ahmadi (2020)
MI-DRW	The improved-DRW results from Mofakham and Ahmadi (2020)
PDE	partial differential equation
RANS	Reynolds-averaged Navier-Stokes equations
RMS	root mean square
RSM	Reynolds-stress-transport-equation model
SC-DRW	The conventional-DRW with the PARTICLE code
SI-DRW	The improved-DRW with the PARTICLE code
SIMPLE	Semi-Implicit Method for Pressure Linked Equations
UDF	User-Defined-Function
UDM	User-Defined-Memory
UDML	User-Defined-Memory-Location

Contents

Masteravtale	iii
Abstract	iv
Sammendrag	v
Acknowledgements	vi
Nomenclature	vii
Contents	xi
Figures	xiii
Tables	xvi
Code Listings	xvii
1 Introduction	1
1.1 Motivation	2
1.2 Objectives	3
1.3 Scope of Work	3
1.4 Outline	4
2 Summary of the Project Work	5
2.1 Literature Review	5
2.2 Method	5
2.3 Concluding Remarks	6
3 Literature Review	7
4 Theory – Fluid Flow and Heat Transfer	9
4.1 Governing Equations	9
4.2 Turbulence Modelling	9
4.2.1 Turbulence Near the Wall	12
4.2.2 Quadratic Variation Near-Wall	12
4.2.3 Curve-Fitted DNS-data	13
4.3 Near-Wall Velocity Profiles	13
4.4 Heat Transfer in Fully Developed Turbulent Flows with Constant Heat Rates	14
5 Theory – Submicron Particle Transport and Deposition Mechanisms	15
5.1 Forces on Particles	15
5.1.1 General Carrier Flow Effects	15
5.1.2 Wall Bonding Forces	18
5.1.3 Phoretic Effects	18
5.1.4 Brownian Diffusion	20
5.1.5 Discrete and Continuous Random Walk Models	20
5.2 Deposition of Micron and Submicron Particles	23
5.2.1 Relevant Parameters	23
5.2.2 Particle Deposition Regimes	24
5.2.3 Experimental Data on Particle Deposition	24
5.2.4 Particle Semi-Empirical Model Predictions	24
5.2.5 An Alternative Presentation of the Results	27
6 Flow Modelling	28
6.1 Properties of Water Vapour	28
6.2 Computational Model	28

6.3	Simulation Setup	29
6.4	Geometry and Mesh	29
6.5	Boundary Conditions	30
6.6	Numerical Residuals	30
6.7	Grid Convergence	31
6.7.1	Aspect Ratio	32
7	Particle Model	34
7.1	Assumptions	34
7.2	Discrete Phase Model Implementation	34
7.2.1	Numerical Schemes and Time Step	34
7.2.2	Boundary Conditions	36
7.2.3	Surface Roughness	36
7.2.4	Particles	36
7.2.5	Particle Forces Implementation	37
7.3	Discrete Random Walk - Turbulent Dispersion of Particles	38
7.3.1	Implementation	38
7.3.2	Lagrangian Eddy-Time Scale	40
7.3.3	Concentration Profiles	41
7.3.4	Inclusion of a Boundary Layer Model	42
7.3.5	Deposition Velocity	44
8	Experimental Investigation	46
8.1	Theoretical Background	46
8.2	Aims and Objectives	47
8.3	Experimental Setup	48
8.4	Flow Rig Design	49
8.5	Experiments - Measurement Procedure	49
8.5.1	Measurements Techniques	50
8.5.2	Experiment Matrix	50
8.6	Calculations of the Results	51
8.6.1	Uncertainty Analysis	52
9	Results and Discussions	53
9.1	Flow Simulation	53
9.1.1	Near-Wall Profiles	53
9.1.2	Discussion	55
9.2	Particle Tracking	55
9.2.1	Concentration Profiles	55
9.2.2	Deposition Velocity	57
9.2.3	An Alternative Presentation of the Results	59
9.2.4	Sensitivity Analysis - Improved-DRW	60
9.2.5	Discussion	61
9.3	Experimental Measurements and Numerical Predictions	66
9.3.1	Measurement Results and Uncertainties	66
9.3.2	Particle Distribution and Calculation Procedure	66
9.3.3	Results	67
9.3.4	Discussion	68
10	Conclusions and Further Work	70
10.1	Concluding Remarks	70
10.2	Further Work	71
	Bibliography	73
A	Experiments	77
A.1	Experimental Procedure	77
B	Fluent Macros	80

Figures

1.1	The deep hot geothermal wells (left) are aimed to deliver water from reservoirs where water is at supercritical conditions due to the nearby magma heat source. Conventional geothermal wells are illustrated to the right. The illustration is taken from National Energy Authority of Iceland (2020).	1
1.2	Cross-section of stainless steel pipes: (left) partially clogged straight pipe, (middle, right) partially clogged outlet of bends. The figure is taken from Karlsdottir et al. (2014).	3
5.1	The thermophoretic coefficient, η_T , is expressed as a function of Kn for the interpolation formulas of Talbot et al. (1980) and Young (2011). Evaluated particle diameters are depicted with blue lines.	19
5.2	Comparison of typical velocity fluctuation histories for the DRW and CRW models. The figure is taken from Bocksell and Loth (2001).	21
5.3	Particle deposition regimes: (1) the diffusion-dominated regime, (2) the eddy-diffusion-impaction regime and (3) the inertia-dominated regime.	25
5.4	Deposition as $Sh/Sc^{1/3}$ evaluated at different Reynolds numbers. The experimental measurements of Shimada et al. (1993) and the Colburn analogy to heat transfer are also presented.	27
6.1	The present geometry utilised in the simulations. The illustration is not to scale.	29
6.2	The dimensionless wall-normal fluctuating velocity plotted versus the dimensionless wall distance for the different grids at $x = 50$ mm. For assessing the performance of the RSM model predictions, the empirical model suggested by Li and Ahmadi (1992)(see Section 4.2.2), DNS data (Moser et al. 1999) and empirical model by Matida et al. (2000) are also presented.	32
6.3	The dimensionless deposition velocity versus the dimensionless particle relaxation time for three grids of different aspect ratios. The performance is compared to the Colburn heat transfer analogy to mass transfer.	33
7.1	Illustration of the particle tracking with DPM in the geometry: (i) fluid inlet; (ii) linear particle injection; (iii) dispersed particles are allowed to develop a particle profile; (iv) test section inlet; (v) outlet, the concentration profile is captured. The illustration is not to scale.	35
7.2	The relative error of the analytic and trapezoidal schemes are evaluated based on the trapezoidal scheme with restricted time step of $\Delta t = \tau_p/2$	36
7.3	The default model in Fluent (a) takes a particle to be deposited when its mass point reaches the wall, whereas the new model (b) takes a particle to be deposited when the particle touches the wall, i.e. it is located $d_p/2$ from the wall. The roughness model (c), shifts the origin of the mean velocity by e and takes a particle to be deposited when it is located $\sigma_k + k - e + d_p/2$ from the wall (see expression (5.42)).	37
7.4	Particle variables at different superheated vapor condition (see Section 5.2.1).	38
7.5	Particle tracking in ANSYS Fluent. The red blocks represent the DRW-model implementation.	39
7.6	The Lagrangian integral time scale, T_L , as a function of y^+ over the half channel width.	40

7.7	The particle concentration profiles of finite-sized particles of 1 μm (left) and 10 nm (right) produced by the different random walk models found in Mofakham and Ahmadi (2019). In the current study, the conventional-DRW (red, dotted) and improved-DRW (black) are compared. The figure is taken from Mofakham and Ahmadi (2019).	42
7.8	Concentration profiles at outlet over the channel width for the SC-DRW (red, dotted)- and SI-DRW(black) models (below). Concentration profiles at outlet at different y^+ for the SC-DRW (red, dotted)- and SI-DRW(black) models (upper).	43
7.9	Comparison of the dimensionless deposition velocity predictions by different DRW-models with experimental, earlier numerical results and a heat transfer analogy.	44
7.10	The dimensionless deposition velocity versus the dimensionless particle relaxation time for $p = 50$ bar compared to the numerical correlation of Fan and Ahmadi (1993), the experimental correlation of Papavergos and Hedley (1984) and the Colburn analogy to heat transfer. The simulation results are based on different boundary layer models for the wall-normal fluctuating velocity; No model, Equation 4.20 and Equation 4.19	45
8.1	Illustration of particle precipitation, agglomeration and deposition: (i) high pressure zone; (ii) pressure drop and $SSI \gg 1$ leading to precipitation of particles; (iii) Agglomeration and system moves towards equilibrium; (iv) Particles grow bigger and system is in quasi-equilibrium. The particle size and the geometry is not to scale.	47
8.2	Schematic diagram of the experimental setup. The blue box represents the autoclave.	48
8.3	Illustration of the functionality of the Equilibar, where the regulator reduces the pressure from the inlet to the outlet based on the reference pressure. The figure is taken from Equilibar (2021).	49
8.4	Picture of the rig at IFE.	50
8.5	(a) The precipitated concentration of amorphous silica in [mg/h] for the two test sections, and (b) the SSI evaluated at different geothermal conditions, according to modelling results from Bordvik, Næss et al. (2021).	51
9.1	Dimensionless cross-sectional profiles of mean and turbulent flow variables at the location of the particle injection ($x_{inj} = 50\text{mm}$) versus the dimensionless wall distance, y^+ . The results are compared with DNS data.	54
9.2	Concentration profiles for particles diameters of 1 nm to 500 nm, simulated at $p = 50$ bar conditions. In (a) to (e), the normalised concentration are presented versus the normalised half channel width, $\xi = y/h$. In (f), the normalised concentration is presented versus the dimensionless wall distance, y^+ , for the five particle sizes.	56
9.3	The dimensionless deposition velocity versus the dimensionless particle relaxation time for $p = 50$ bar compared to the numerical correlation of Fan and Ahmadi (1993), the experimental correlation of Papavergos and Hedley (1984) and the Colburn analogy to heat transfer.	57
9.4	The dimensionless deposition velocity versus the dimensionless particle relaxation time for $p = 150$ bar compared to the numerical correlation of Fan and Ahmadi (1993), the experimental correlation of Papavergos and Hedley (1984) and the Colburn analogy to heat transfer.	58
9.5	The dimensionless deposition velocity versus the dimensionless particle relaxation time for $p = 275$ bar compared to the numerical correlation of Fan and Ahmadi (1993), the experimental correlation of Papavergos and Hedley (1984) and the Colburn analogy to heat transfer.	58
9.6	The dimensionless deposition velocity versus the dimensionless particle relaxation time for $p = 50$ bar compared to the numerical correlation of Fan and Ahmadi (1993), the experimental correlation of Papavergos and Hedley (1984) and the Colburn analogy to heat transfer.	59
9.7	The dimensionless deposition velocity versus the dimensionless particle relaxation time for $p = 50$ bar when the effect of thermophoresis is included. The results are compared with the numerical correlation of Fan and Ahmadi (1993), He and Ahmadi (1998) and the Colburn analogy to heat transfer.	59

9.8	(a) The present numerical results, theoretical predictions with Equation 5.43, the Colburn analogy to heat transfer and experimental results of Shimada et al. (1993) are presented for $Sh/Sc^{1/3}$ versus the Reynolds number. (b) A detailed view on the present numerical results at different geothermal conditions (coloured) and particle diameters (marked).	60
9.9	The results of the sensitivity analysis of $d_p = 100$ nm for $p = 50$ bar for the cases I-V. (a) The normalised concentration profile versus the dimensionless wall distance. (b) The dimensionless deposition velocity versus the dimensionless particle relaxation time.	61
9.10	Predicted particle size distributions in the two test sections in the experimental rig. The particle size distribution is presented versus the mass concentration (a) and versus the number of particles concentration (b).	67
9.11	Deposition rates based on the present numerical results and the predicted particle size distribution, in test section 1 (a) The effective dimensionless deposition velocity versus the particle relaxation time for the present numerical results and the empirical correlation of Fan and Ahmadi (1993). (b) The deposition rate [mg/h] versus the particle diameter.	68
9.12	Presentation of the dimensionless deposition velocities from present experimental measurements (including uncertainties), predicted by the PARTICLE model and calculated based on the predicted particle size distribution of Bordvik, Næss et al. (2021). The horizontal bars represent the span of particles in the distribution in Figure 9.11a. Empirical results and a heat transfer analogy are included for comparison.	69
9.13	The results from the preliminary experimental investigation is presented with the alternative presentation of deposition rate ($Sh/Sc^{1/3}$). Here, the upper experimental data point is from test section 1 and the lower from test section 2.	69
A.1	Picture of the rig at IFE.	78
A.2	Three-dimensional model of the rig.	78
A.3	Dimensions of the test rig in [mm] from the Equilibar (left) to the manual control valves (right).	79
A.4	Picture of the autoclave, located inside the oven in Figure A.1.	79

Tables

6.1	Water vapour properties utilised in the fluid flow model, from the International Association for the Properties of Water and Steam (Wagner and Kretzschmar 2008).	28
6.2	Grid refinement	31
6.3	Grid convergence index	31
6.4	Aspect ratio grids	32
7.1	Properties of silica used in the simulations. The data are collected from Bergman et al. (2011).	37
8.1	Experiment matrix with the test section conditions. The performed experiment is presented in bold mode.	51
8.2	Predictions of generation and agglomeration of particles by Bordvik, Næss et al. (2021). The mean concentration, \bar{c}_{SiO_2} , is a measure of the dispersed solid particles in the flow at the inlet of the section.	52
8.3	Descriptions of the uncertainties related to the measured variables.	52
9.1	Uncertainty estimates for the dimensionless deposition velocity, V_d^+	66

Code Listings

B.1 PARTICLE model: UDFs 80

1 | Introduction

Geothermal energy is a renewable energy source with great potential for heating and power generation. In the last decade, research has progressed on deep hot geothermal wells in magmatic areas, where geothermal fluids may reach supercritical conditions. The energy potential per well is very high in these environments since the thermal efficiency is proportional to temperature. However, there are some technology gaps, both with respect to drilling and utilisation. This master's thesis is related to the fouling problem observed in geothermal pipes during flow tests by Iceland Deep Drilling Project (IDDP).

This master's thesis (from here on, the present study) is a continuation of the project work of Stordal (2020) and the master's thesis of Paulsen (2020). The findings in the project work are summarised in Chapter 2. The present study is part of an ongoing study by the Department of Energy and Process Engineering at NTNU in cooperation with Equinor on the IDDP. The Research Council of Norway supports the project.

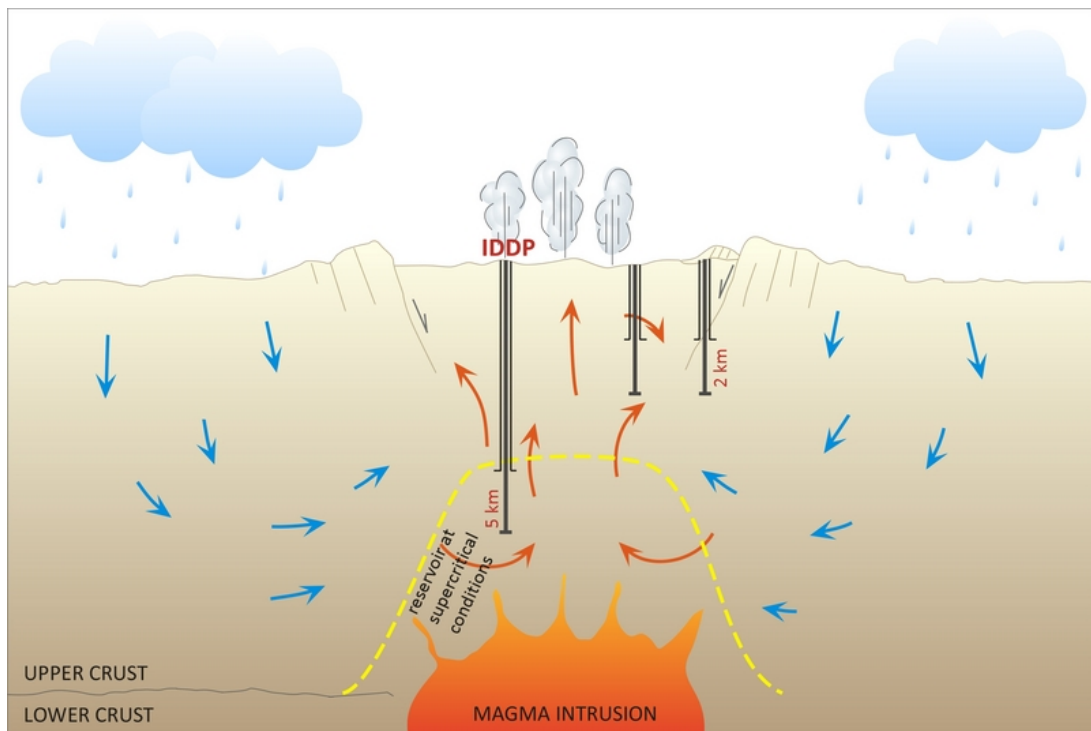


Figure 1.1: The deep hot geothermal wells (left) are aimed to deliver water from reservoirs where water is at supercritical conditions due to the nearby magma heat source. Conventional geothermal wells are illustrated to the right. The illustration is taken from National Energy Authority of Iceland (2020).

1.1 Motivation

Deep hot geothermal wells are characterised by temperatures and pressures above critical conditions of water in reservoirs nearby a magmatic heat source, as illustrated in Figure 1.1. The conditions in the reservoir can reach 500°C and 350bar, and this is also the base case in the ongoing study at NTNU. For such supercritical conditions, water properties can vary from liquid-like to gas-like based on their temperature and pressure. Conventional geothermal wells produce liquid water or a two-phase mixture of saturated vapour and liquid of lower temperature and pressure. Some conventional vapour-dominated geothermal fields deliver superheated steam (Ellis and Anliker 1981), which can potentially extract more power with better thermodynamic efficiency and lower operational cost (Chauhan 2019). For the production of supercritical steam, which has higher enthalpy and mass per unit volume rate, modelling results from Albertsson Fridleifsson et al. (2003) showed that an order of magnitude higher power output could be extracted from these plants compared to a conventional geothermal field.

However, such energy potential cannot be exploited with the current technologies. Precipitation of solids and subsequent scaling was shown to be a significant problem for deep hot geothermal wells in the flow tests on the IDDP-1 well (Karlsdottir et al. 2014). Scaling is also a common issue in conventional and high-enthalpy wells. In particular, solid SiO₂ is present in geothermal plants across the world, and it is the most troublesome mineral in high-enthalpy applications (van den Heuvel et al. 2018; von Hirtz 2016). This is related to the high content of silicon (Si) in the Earth's crust. In superheated and supercritical geothermal steam production, precipitation is especially fast due to the fluid properties in the gaseous phase.

For the reservoir conditions of 500°C and 350bar, the equilibrium concentration of silica in water is estimated to be 244mg/kg (Fournier and Potter II 1982b). This concentration is considerable in gaseous form and occurs due to increased silica solubility with pressure near the supercritical region. The geothermal fluid may contain even more dissolved silica in the presence of fluorine and chlorine in the geothermal composition (Fridriksson et al. 2015; Karlsdottir et al. 2014). When the superheated steam or supercritical water is brought through the wellhead and into the process plant, the fluid is prone to several pressure drops. Fournier and Potter II (1982a) demonstrated that the solubility of silica in water vapour is a function of the fluid density and temperature. In contrast, silica solubility in geothermal liquid brines is only related to temperature. Therefore, as the density is drastically reduced over pressure drops, the solubility of silica in the fluid drops as well. At this stage, the geothermal fluid is supersaturated with silica and precipitation of solid silica occurs. The silica particles are carried upstream in the superheated flow while agglomerating to bigger particles. The particles are deposited on surfaces of different process components, e.g. steam turbines, causing scaling Chauhan (2019). Deposits on turbine blades and nozzles may distort the shape of the blades, causing roughness, uneven flow conditions and events, and increased losses.

The particle generation model of Bordvik, Næss et al. (2021) of the kinetics of silica particles in superheated water vapour indicate that the rate of precipitation is faster than if in a liquid phase. The initially generated particles (nucleus) are here estimated to be of $\mathcal{O}(1\text{ nm})$, where the nucleus size depends on the rate of supersaturation. Higher rates results in smaller particles (Bordvik and Næss 2020). Karlsdottir et al. (2014) have performed on-site experiments of depressurised geothermal steam at the IDDP-1 project facility. The dry superheated steam was reported to be supersaturated with silica, causing the test unit to clog after only 24 days of testing. Figure 1.2 shows partially clogged cross-sections of the pipe at different locations of the test rig after 24 days. Clogging is also a common challenge in geothermal power plants when reinjecting the geothermal fluid back into the ground, causing costly interventions and need for recompletions (Bordvik and Næss 2020).

Conventional methods of dealing with silica precipitation and scaling reduce the super-heat and therefore the utilisation efficiency of the system. The fouling issues must be addressed before the utilisation of such resources can be achieved. Therefore, studies on the kinetics, dispersion and deposition of submicron silica particles are essential to facilitate new technologies. As part of the IDDP project, Chauhan (2019) investigated the deposition mechanisms of silica particles in a superheated turbulent geothermal steam flow. He performed a computational study and an experimental investigation, which showed an increase in deposition velocity with particle diameter for micrometre scale particle sizes. However, the investigation lacked descriptions and studies on submicron particle deposition, which geothermal plants from deep hot geothermal wells are prone to. The submicron particles dispersed in the



Figure 1.2: Cross-section of stainless steel pipes: (left) partially clogged straight pipe, (middle, right) partially clogged outlet of bends. The figure is taken from Karlsdottir et al. (2014).

superheated steam behave differently than the micron-sized particles studied by Chauhan (2019), as the smaller particles are more susceptible to diffusion mechanisms. Investigations on larger particles are also more common in the literature on conventional geothermal liquid brines (Brown 2011; Kokhanenko 2014). In general, there are few references to experimental measurements of submicron particle deposition in particle-laden flows in the literature. Most experimental and numerical research on particle-laden flows with a gaseous medium as a carrier phase is employed with air. More specifically, no references to experiments nor numerical studies on the deposition and transport of submicron silica particles in turbulent superheated and supercritical water vapour are found in the literature.

In this study, numerical investigations on dispersion-, transport- and deposition mechanisms of submicron silica particles in turbulent flows of superheated and supercritical steam are performed. In addition, submicron particle deposition from turbulent superheated and supercritical steam flows is studied experimentally. It is hereby made clear that only contributions to the experimental investigation was made. Most of the planning and design of the experimental rig were performed by my supervisor and Prof. Erling Næss and my co-supervisor and PhD Candidate, Silje Bordvik.

The scientific question reduces to:

What are the dominant deposition mechanisms for submicron particles in a turbulent superheated steam flow and what deposition velocities can be expected for particles generated from the superheated steam supersaturated with silicic acid?

1.2 Objectives

The objective of this master's thesis is to establish a numerical model for transport and deposition of submicron particles in a turbulent gas flow using ANSYS® Fluent Release 20.2. Model improvements must be made to better the physical applicability for submicron particles, especially the model for turbulent dispersion of particles. The improved model will then be adopted to geothermal conditions of water vapour provided by the Department. Dominant deposition mechanisms will be characterised and the deposition velocities at different conditions will be quantified. In addition, contributions were made on an experimental investigation on the generation and subsequent deposition of submicron particles from superheated and supercritical steam to validate the numerical model.

1.3 Scope of Work

Submicron particle transport in turbulent flows is complex. Fluid-particle interactions are elaborate, and simplifications have to be made in order to describe particle behaviour. The model implementation reduces to a description of distinct particle transport mechanisms and this is a drawback of representing the particle interactions numerically. As all physical contributions cannot be included, the numerical model

is limited by the included particle transport models. However, as the model is validated and verified with experimental measurements and other numerical models, the simplifications can be justified.

In the present study, some general and common assumptions are made:

- The intricate drag forces over the amorphous silica particles are assumed to be steady-state, and the particles are represented by smooth spheres.
- Implications of secondary flow effects in pipe flows are omitted, and the domain is represented by a straight channel.
- The particle deposition predictions are on the initial stage of the fouling process.
- The complexity related to particle-particle interactions (agglomeration) is omitted in the deposition model.

Further simplifications and limitations in the present work are presented when needed.

1.4 Outline

Chapter 2 summarises the project work, which is the background and basis of this thesis. Chapter 3 introduces relevant literature on numerical simulations of submicron particle deposition in turbulent flows. Chapter 4 presents the theory on turbulent fluid flows and heat transfer in a channel flow, with emphasis on the wall region. Chapter 5 describes the dominant transport and deposition mechanisms for submicron particles and presents relevant and state-of-the-art models for these mechanisms. In Chapter 6, the fluid flow method is presented, and the numerical grid is verified. Chapter 7 presents the particle model implementations, and the particle model is verified with numerical models. Chapter 8 describes the experimental investigation. The theoretical background, the experimental setup, the construction of the rig and the performed experiments are described. In Chapter 9, the fluid flow and particle deposition results are presented and discussed. Chapter 10 consists of a conclusion from the discussions and recommendations for further work.

2 | Summary of the Project Work

This master's thesis is a continuation of Paulsen (2020) and the project work of Stordal (2020). The latter can be received upon request. In the following chapter, the most important findings in the project work are summarised.

2.1 Literature Review

Tian and Ahmadi (2007) compared different numerical model predictions of deposition of nano- and micro-particles in straight turbulent duct flows with a Reynolds number of 6667. The different turbulence models and the predicted wall-normal velocity fluctuations near the wall were related to discrepancies in the particle deposition predictions from experimental data. Here, the anisotropic Reynolds stress equation turbulence model (RSM) produces a lower wall-normal fluctuating velocity component than the simpler, isotropic $k-\varepsilon$ turbulence model, and it predicts lower deposition rates closer to the experimental data. Gao et al. (2012) performed a similar comparison of simulation methods in ANSYS Fluent and paid special attention to the near-wall treatment of RANS turbulence models. The simulated Reynolds number based on the mean flow and the channel width was 6658. The two-equation $k-\omega$ *SST* turbulence model performed similarly to the anisotropic RSM with regards to the deposition velocity, both over-predicting the deposition velocity for submicron particles.

2.2 Method

The chosen fluid phase was air, as the deposition mechanisms of gaseous media are assumed to be similar and extensive work regarding experimental and numerical studies on particle deposition with air is found in the literature.

Mathematical Approaches

The dilute phase is assumed not to affect the fluid phase due to the low volume fraction of particles, as the concentration of silica per kg water is reported to be 245 mg/kg (Fournier and Potter II 1982b). Elghobashi (1994) proposed the term one-way coupling for such flows, where only the fluid phase is assumed to affect the particle motion.

There are two common mathematical approaches for simulating the particulate phase in a fluid flow: The Euler-Euler approach and the Euler-Lagrangian approach. The two approaches only differ in the simulation method of the particulate phase:

In the Euler-Euler approach, the particulate phase is considered as a continuum under some restrictions and conditions (Elghobashi and Abou-Arab 1983). The conservation equations are similar to those of the carrier phase. This approach is the first applied to calculate particle deposition and is the most computational efficient of the two approaches (Guha 2008). It faces challenges with, e.g. implementing the physically correct boundary treatment, handling discontinuities in the particle phase concentration and model tuning with empirical data is often required (Guha 2008). In addition, the literature on the Euler-Euler approach is weaker as the commercial computational codes more widely offer the Euler-Lagrangian approach for simulating dispersed particle-laden flows of small particles.

In the Lagrangian approach, the individual particle trajectory is computed by solving the particle momentum equation. In order to reduce the computational cost, the particulate phase is represented with a number of particle streams. Guha (2008) points out that this approach is unlikely to become a practical method for engineering calculations due to computational intensive and expensive calculations (especially for small particles in a turbulent field), but a good research tool for understanding the flow physics. Elghobashi (1994) concluded that the Lagrangian approach is the most suitable for the one-way coupling regime. Fluent (2021b) makes a similar recommendations for particulate phase volume fractions less than 10%.

The Lagrangian approach is also widely used in literature on submicron particles. Hence implementation methods and validation are more available. The works of Qian Chen and Ahmadi (1997), Fan and Ahmadi (1993), Li and Ahmadi (1992), Mofakham and Ahmadi (2020), Ounis and Ahmadi (1990), Ounis, Ahmadi and J. B. McLaughlin (1991), Ounis, Ahmadi and J. B. McLaughlin (1993) and Tian and Ahmadi (2007) have all employed this approach, so have Gao et al. (2012) and Kallio and Reeks (1989). The former work at NTNU by Paulsen (2020) and Tandberg (2017) have also used the Lagrangian particle tracking approach. This was also the chosen approach in the project work.

Modelling Assumptions

The numerical model was performed in ANSYS® Fluent Release 20.1 with the $k-\omega$ *SST* turbulence model. The deposition of particles was assumed to be initial (mono-layer), i.e. an influence from a wall layer of silica on the particle deposition was not evaluated. In addition, the particles were modelled as non-rotating spheres and injected with a linear distribution into the flow. At the test section inlet, the particle distribution is assumed fully developed. Particle agglomeration was not examined, and the particle-particle interaction was neglected (Elghobashi 1994).

2.3 Concluding Remarks

The $k-\omega$ *SST* turbulence model was found to overestimate the near-wall normal fluctuating component, and a better modelling approach for this velocity component is emphasised, e.g. Reynolds stress equation model. A parameter study was performed to determine the dominant deposition mechanisms of submicron particles. The Brownian motion, thermophoresis and the Lagrangian time scale constant, C_L , related to the discrete random walk model (DRW), were all concluded to be of significance on the particle deposition velocity. Gravitational orientation and lift forces are found to be insignificant for submicron particles. In addition, unsteady forces, buoyancy forces and the effect of a fluid flow pressure gradient on particle motion can be neglected for submicron silica particles dispersed in water vapour due to the high particle-to-fluid density ratio.

3 | Literature Review

The numerical model established in the master's thesis is based on the model developed and findings in the project work of Stordal (2020), where a more extensive literature review was performed. The most important findings are described in the summary of the project work (see section 2.1). During the initial thesis work, two main challenges with the default model in ANSYS Fluent were discovered. Firstly, The wall-normal mean fluctuating velocity ($\overline{v'^2}$) in the vicinity of the wall was overpredicted by the Reynolds stress Transport Model (RSM), leading to non-physical enhanced deposition. Secondly, the default particle model for generating the instantaneous velocity fluctuation in ANSYS Fluent, the so-called conventional-discrete random walk model (DRW), produced a spurious drift of particles towards the wall, leading to particle accumulation in the near-wall region and enhanced deposition. The literature study below focuses especially on improvements to address these challenges.

Overestimation of the wall-normal fluctuating velocity in the vicinity of a wall is a common issue when employing the Reynolds stress transport model (RSM) and two-equation models, e.g. $k-\omega$ SST. Therefore, implementation of a near-wall correction, named a boundary layer model, is common in the literature (Dehbi 2008; Gao et al. 2012; H. Lu and L. Lu 2015; Tian and Ahmadi 2007). H. Lu and L. Lu (2015) imposed a boundary layer model in the vicinity of the wall ($y^+ < 4$, where y^+ is the dimensionless wall distance) for the wall-normal fluctuating velocity in a turbulent duct air flow using user-defined functions (UDFs) in ANSYS Fluent. The model overpredicts the deposition velocity for submicron particles by a factor between two and five compared to the numerical model of Tian and Ahmadi (2007) and up to a magnitude compared to the empirical equation of Wood (1981). Dehbi (2008) included a boundary layer model near the wall ($y^+ < 100$) in a three-dimensional turbulent pipe flow for the three fluctuating velocity components and the dissipation rate in ANSYS Fluent. The fluid medium was ambient air. The model predictions for deposition were significantly improved with the boundary layer model for micron-sized particles. However, the model does not suppress the so-called "spurious drift" of tracer particles towards the wall region, and unphysical high particle concentrations are predicted near the wall.

Mofakham, Ahmadi and J. McLaughlin (2018) performed DNS simulations for particle sizes from 10nm to 80 μ m with corresponding $\tau_p^+ \in [2.2 \cdot 10^{-6}, 142]$. This work concluded that submicron particle distribution in the near-wall region is made random by Brownian motion. Submicron particles have a small particle relaxation time and follow fluid particle trajectories in the core flow. Henceforth, a uniform concentration profile parallel to the channel wall is expected for submicron particles.

The spurious drift of particles is related to turbulent dispersion and is introduced by the random walk models for the instantaneous turbulent velocity (Bocksell and Loth 2001; MacInnes and Bracco 1992; Strutt and Lightstone 2006). The conventional discrete random walk model (DRW) is the default model in ANSYS Fluent on particle dispersion in turbulent flows. Several authors applies the DRW on submicron particles (Dehbi 2008; Gao et al. 2012; H. Lu and L. Lu 2015; Tian and Ahmadi 2007), even though it is not recommended for submicron particle tracking in the theory guide of Fluent (2021b). Mofakham and Ahmadi (2020) showed that the conventional DRW is susceptible to spurious drift of submicron particles. To attenuate the spurious drift and improve the particle deposition predictions, determination of the Lagrangian time scale constant, C_L , is crucial, according to Milojević (1990). This constant is flow-dependent, and it is shown to affect the deposition velocity for submicron particles (Stordal 2020). Mozafari (2014) performs a numerical calibration method on higher Reynolds number flows, which improves particle dispersion compared to experimental data. Longmire (2007) implemented UDFs in ANSYS Fluent to include boundary layer models for the wall-normal fluctuating velocity and the

Lagrangian time scale for predictions of deposition in bends ($y^+ < 200$). The UDF code utilises the same theory as the conventional DRW model, i.e. the spurious drift is not adjusted. However, the proposed algorithm showed satisfactory results and is made freely available. Further developments and modifications on the code are to be required for predictions on submicron particle transport and deposition.

More recently, Mofakham and Ahmadi (2020) proposed an improved DRW based on the findings first suggested by Monin and Yaglom (1971). In the paper of Mofakham and Ahmadi (2020), the conventional and improved-DRW were compared with regards to the particle concentration profile and deposition velocities. In the proposed model, the spurious drift is suppressed by the inclusion of drift terms. Mofakham and Ahmadi (2020) utilise the $v^2 - f$ turbulence model in OpenFOAM, which aims at solving the wall-normal fluctuating component correctly near the wall. In low-Re flows, this model predicts this component similar to experimental and DNS data. The results from OpenFOAM were then used in an in-house Matlab particle tracking code. The improved-DRW produces more realistic particle concentration profiles, especially for the lowest Stokes number particles (10 nm and 1 μm), and the deposition velocities correlate better with experimental data.

4 | Theory – Fluid Flow and Heat Transfer

In the following chapter, the turbulence models for solving the governing equations are introduced. In this regard, emphasis is put on near-wall turbulence. A simple correlation for the heat transfer is also presented. The scales for nondimensionalising all parameters in the present study are the characteristic velocity, u_τ , the characteristic length, ν/u_τ , and the characteristic time ν/u_τ^2 . Here, $u_\tau = \sqrt{\tau_w/\rho}$ is the friction velocity, and τ_w , ρ and ν are the wall shear stress, density and kinematic viscosity, respectively.

4.1 Governing Equations

The governing equations of a channel flow are those of mass, momentum and energy conservation. A derivation of these equations can be found in White (2019). Here, the equations are written in integral form, integrated over an arbitrary control volume, Ω . Furthermore, the Einstein summation convention is employed. In the current study, the flow field is assumed incompressible and steady. Then, the continuity equation reads

$$\int_{\Omega} \left(\frac{\partial u_i}{\partial x_i} \right) d\Omega = 0, \quad (4.1)$$

with u_i the fluid velocity component in the x_i direction. The momentum equation reads

$$\int_{\Omega} \rho_f \left(\frac{\partial}{\partial x_j} (u_i u_j) \right) d\Omega = \int_{\Omega} \frac{\sigma_{ij}}{x_j} d\Omega \quad (4.2)$$

where the body forces are neglected, and ρ_f is the fluid density. The stress tensor σ_{ij} is for a Newtonian fluid given by

$$\sigma_{ij} = p\delta_{ij} - \mu \left(\frac{\partial u_i}{\partial x_j} + \frac{\partial u_j}{\partial x_i} \right). \quad (4.3)$$

Here, p is the static pressure, μ is the dynamic viscosity of the fluid and δ_{ij} is the Kronecker-Delta function. By considering the internal energy per unit mass e as only sensible thermal energy, we can formulate the equation for conservation of energy as

$$\int_{\Omega} \left(\rho_f \frac{\partial}{\partial x_j} (u_j e) \right) d\Omega = \int_{\Omega} \left(- \frac{\partial q_j}{\partial x_j} - \sigma_{ij} \frac{\partial u_i}{\partial x_j} \right) d\Omega, \quad (4.4)$$

where q_j is the heat flux in the x_j direction and σ_{ij} is again the stress tensor.

4.2 Turbulence Modelling

When performing brute-force calculations, or direct numerical simulations (DNS), one would solve the governing equations directly for the fluid variables, e.g. u_i , p and ρ . In other words, the equations are

numerically solved without any turbulence model. Such simulations are not feasible for industrial applications, as the computational cost of DNS is very high. Averaging techniques are therefore used. In the simulations performed and presented in this study, the Reynolds Averaged Navier-Stokes (RANS) equations are solved, which are a set of equations arising from applying a Reynolds decomposition and subsequent time-averaging of the flow variables. For a scalar ϕ the time-averaged quantity $\bar{\phi}$ is

$$\bar{\phi} = \lim_{T \rightarrow \infty} \frac{1}{T} \int_{-T/2}^{T/2} \phi dt, \quad (4.5)$$

when ϕ is averaged over the time interval $t \in [-T/2, T/2]$. The Reynolds decomposition divides a variable into two parts, the average and a fluctuating part, such that $\phi = \bar{\phi} + \phi'$, with ϕ' being the fluctuating component.

It has been shown in the project work of Stordal (2020) that the assumption of isotropic turbulence in the near-wall region lead to inaccurate predictions of particle deposition. A better modelling methodology is, according to Tian and Ahmadi (2007), to abandon the isotropic eddy-viscosity hypothesis and model a more realistic anisotropic fluid flow field. This significantly affect the predictions of the near-wall turbulence velocity fluctuations. Tian and Ahmadi (2007) employed the Reynolds stress transport model (RSM) with good predictions of deposition, hence DNS and Large Eddy Simulations (LES) are deemed unnecessary in the present study. The RSM is the most elaborate type of RANS turbulence model in many commercial computational fluid dynamics (CFD) codes, and include anisotropy of the velocity fluctuations. Anisotropic turbulence is modelled by separate transport equations for the individual Reynolds-stress components:

$$-\rho \overline{u'_i u'_j} = \rho \cdot \begin{bmatrix} \overline{u'_1{}^2} & \overline{u'_1 u'_2} & \overline{u'_1 u'_3} \\ \overline{u'_2 u'_1} & \overline{u'_2{}^2} & \overline{u'_2 u'_3} \\ \overline{u'_3 u'_1} & \overline{u'_3 u'_2} & \overline{u'_3{}^2} \end{bmatrix}$$

The above Reynolds-stress components are those of three dimensions, and by the symmetry of the matrix, this leads to six equations to be solved. The two dimension case reduces to four equations of Reynolds-stress components:

$$-\rho \overline{u'_i u'_j} = \rho \cdot \begin{bmatrix} \overline{u'_1{}^2} & \overline{u'_1 u'_2} & \\ \overline{u'_2 u'_1} & \overline{u'_2{}^2} & \\ & & \overline{u'_3{}^2} \end{bmatrix}.$$

The $\overline{u'_3{}^2}$ needs to be calculated, as it is included the equation for the turbulent kinetic energy, k . In addition, a scale-determining equation is required in the RSM for the closure of the equations. This is typically the turbulent dissipation rate, ε , or the specific turbulent dissipation rate, ω . In total, seven partial differential equations (PDEs) are solved for this turbulence model in a three-dimensional domain and five PDEs for a two-dimensional domain.

The equations employed in the RSM model are exact and derived from the Navier-Stoke equation. Assuming no system rotation, a negligible buoyancy production and no body forces, the transport

equations for the Reynolds stresses, may be written as:

$$\begin{aligned}
\frac{D\rho\overline{u'_i u'_j}}{Dt} = & \underbrace{-\rho\left(\overline{u'_i u'_k} \frac{\partial u_j}{\partial x_k} + \overline{u'_j u'_k} \frac{\partial u_i}{\partial x_k}\right)}_{P_{ij} = \text{Production due to Mean Strain}} \\
& + \underbrace{p' \left(\frac{\partial u'_i}{\partial x_j} + \frac{\partial u'_j}{\partial x_i} \right)}_{\phi_{ij} = \text{Pressure-Strain Correlation}} \\
& - \underbrace{\frac{\partial}{\partial x_k} \left[\overline{\rho u'_i u'_j u'_k} + \overline{p'(\delta_{kj} u'_i + \delta_{ik} u'_j)} \right]}_{D_{T,ij} = \text{Turbulent Diffusion}} \\
& + \underbrace{\frac{\partial}{\partial x_k} \left[\mu \frac{\partial}{\partial x_k} (\overline{u'_i u'_j}) \right]}_{D_{M,ij} = \text{Molecular Diffusion}} - \underbrace{2\mu \frac{\partial u'_i}{\partial x_k} \frac{\partial u'_j}{\partial x_k}}_{\varepsilon_{ij} = \text{Dissipation}}
\end{aligned} \tag{4.6}$$

Here, the left-hand side represents the change of Reynolds stresses for a fluid element. On the right-hand side, the molecular diffusion, $D_{M,ij}$ and the production due to mean strain, P_{ij} , are exact equations and do not require any modelling. However, the three terms ε_{ij} , ϕ_{ij} and $D_{T,ij}$ need to be modelled to close the equations of RSM (Fluent 2021b). In particular, the modelling of the pressure strain and the dissipation-rate terms is challenging and compromises RSM predictions' accuracy. Below, the models of the terms mentioned above are described as in the theory guide of Fluent (2021b). The dissipation is modelled as

$$\varepsilon_{ij} = \frac{2}{3} \delta_{ij} \varepsilon, \tag{4.7}$$

where the scalar ε is obtained from the transport equation of ε , similar to the $k - \varepsilon$ equations (see Fluent (2021b) and White (2019)). This model is simplified by the use of Kolmogorov's local isotropy hypothesis. This holds away from the wall, but near the wall ($y^+ < 20$, where $y^+ = yu_\tau/\nu$ is the dimensionless wall distance) $\varepsilon_{12} \neq 0$ and the model predictions will possibly deviate from DNS data (Jovanović et al. 1995; Perot and Natu 2004). The turbulent viscosity is modelled as

$$\mu_t = C_\mu \rho \frac{k^2}{\varepsilon}. \tag{4.8}$$

Furthermore, the turbulence diffusion is modelled as

$$D_{T,ij} = \frac{\partial}{\partial x_k} \left(\frac{\mu_t}{\sigma_k} \frac{\partial \overline{u'_i u'_j}}{\partial x_k} \right), \tag{4.9}$$

which is a simplification by ANSYS Fluent to address numerical instabilities (Fluent 2021b). Here, $\sigma_k = 0.82$.

The pressure-strain components tend to redistribute energy between the different normal Reynolds stresses. It can be demonstrated that the pressure-strain, ϕ_{ij} , do not change the turbulent kinetic energy, i.e. the sum of the normal pressure-strain components equal to zero ($\phi_{ii} = 0$) (Andersson 1988). Pressure-strain can be modelled in different ways. The ε -based RSM model performs better for straight channels, and in this approach, a linear and a quadratic relation for the pressure-strain can be employed (Fluent 2021b). In this study, it is important to resolve the viscous sublayer, and the near-wall enhanced wall treatment is emphasised by the literature (D'Auria 2017; Mofakham and Ahmadi 2020; Tian and Ahmadi 2007). Therefore, only the linear relation for pressure strain can be chosen here, which reads,

$$\phi_{ij} = \phi_{ij}^{slow} + \phi_{ij}^{rapid} + \phi_{ij}^{wall}. \tag{4.10}$$

Here, ϕ_{ij}^{slow} is called the return-to-isotropy term, ϕ_{ij}^{rapid} is the rapid pressure-strain term, and ϕ_{ij}^{wall} is the wall-reflection term. The latter is responsible for redistributing the normal stresses in the near-wall

region by dampening the wall-normal stresses and enhancing the stresses parallel to the wall. Note that the wall-reflection term is calibrated for channel flow and flat plates involving a single wall, i.e. geometries like axisymmetric pipes and curvilinear ducts are not calibrated for, and the term may be excluded with respect to accuracy. In addition, low-Reynolds number modifications by Launder and Shima (1989) are applied on the linear pressure-strain model when the enhanced wall treatment is selected. However, discrepancies for v' are expected compared to DNS data very close to the wall ($y^+ < 8$) (Launder and Shima 1989).

The reader is referred to the ANSYS Theory Guide of Fluent (2021b) and White (2019) for further derivations on turbulence modelling of the equations mentioned above.

4.2.1 Turbulence Near the Wall

Tian and Ahmadi (2007) emphasised the importance of near-wall turbulence predictions on particle deposition simulations. Therefore, the two-layer zonal model of the RSM in ANSYS Fluent for the enhanced wall treatment is presented here. This near-wall approach is based on the work by H. Chen and Patel (1988) and aims to resolve the viscous sublayer and the buffer layer of flow. Henceforth, Fluent (2021b) recommend a non-varying y^+ -value of unity. The two layers represent a viscosity-affected region and a fully turbulent region, demarcated by the wall-distance based turbulent Reynolds number, defined as

$$Re_t = \frac{y\sqrt{k}}{\nu_f}. \quad (4.11)$$

For a $Re_t < 200$, in the near-wall region, the equation for the turbulent dissipation rate ε is replaced by the algebraically modelled ε_{wall}

$$\varepsilon_{wall} = \frac{k^{3/2}}{l_\varepsilon}, \quad (4.12)$$

and the turbulent viscosity μ_t is modelled

$$\mu_t = C_\mu \rho \sqrt{k} l_\mu. \quad (4.13)$$

where $C_\mu = 0.09$. The above equations are included in the models for dissipation, ε_{ij} , and turbulent diffusion, $D_{T,ij}$, in the transport equations for the Reynolds stresses (Equation 4.6). In Equations (4.12) and (4.13), the damping of the wall effects is taken into account by the length scales,

$$l_\mu = C_l y (1 - e^{-(Re_t/A_\mu)}) \quad (4.14)$$

and

$$l_\varepsilon = C_l y (1 - e^{-(Re_t/A_\varepsilon)}). \quad (4.15)$$

The damping of Equation 4.14 and Equation 4.15 is maximum at the wall and decreases with distance from the wall. The turbulence parameters (ε and μ_t) are blended from the near-wall layer to the fully turbulent region with these functions until Re_t reaches 200. In the fully turbulent region the RSM turbulence model is employed. The constants in Equation 4.14 and Equation 4.15 are $C_l = \kappa C_\mu^{3/4}$, $A_\mu = 70$ and $A_\varepsilon = 2C_l$. The reader is referred to the Fluent (2021b) theory guide for further details on blending functions.

4.2.2 Quadratic Variation Near-Wall

Theoretically, the root mean square (RMS) velocity fluctuations normal to the wall, v' , follow a quadratic variation. Following the derivation of Sveningsson (2003), the fluctuating velocities in the vicinity of the wall can be expanded accordingly

$$\begin{aligned} u' &= a_0 + a_1 y + a_2 y^2 \dots \\ v' &= b_0 + b_1 y + b_2 y^2 \dots \\ w' &= c_0 + c_1 y + c_2 y^2 \dots \end{aligned} \quad (4.16)$$

The coefficients (a_m, b_m and c_m) in the above equation can be functions of anything but y and are zero if averaged. The no-slip condition at the wall gives $a_0 = b_0 = c_0 = 0$. Furthermore, no-slip gives $(\partial u/\partial x)_{y_{wall}} = (\partial w/\partial z)_{y_{wall}} = 0$. By continuity, $(\partial v/\partial y)_{y_{wall}} = 0$ and b_1 too must be equal to zero. The behaviour of the RMS velocity fluctuations are found by squaring and averaging the expressions for the fluctuating components:

$$\begin{aligned}\overline{u'^2} &= \overline{a_1^2} y^2 + \mathcal{O}(y^3) \\ \overline{v'^2} &= \overline{b_2^2} y^4 + \mathcal{O}(y^5) \\ \overline{w'^2} &= \overline{c_1^2} y^2 + \mathcal{O}(y^3)\end{aligned}\tag{4.17}$$

This trend of variation was first mentioned in Hinze (1975) and was later verified by experimental measurements and DNS simulations of Kim et al. (1987). As a result, Ounis, Ahmadi and J. B. McLaughlin (1993) recommend

$$\sqrt{\overline{v'^2}} \propto y^2 \text{ as } y \rightarrow 0.\tag{4.18}$$

$$v'^+ = Ay^{+2} \text{ for } y^+ < 4.\tag{4.19}$$

Here, $A = 0.008$ is suggested. v'^+ and y^+ are the dimensionless wall-normal fluctuating velocity and the dimensionless wall distance, respectively. It has been shown in numerous articles that bad estimates of v' significantly affects the particle deposition velocity predictions, emphasising proper estimates close to the wall (Gao et al. 2012; Li and Ahmadi 1992; Ounis, Ahmadi and J. B. McLaughlin 1993; Stordal 2020; Tian and Ahmadi 2007).

4.2.3 Curve-Fitted DNS-data

Matida et al. (2000) has curve-fitted the DNS-data of Dreeben and Pope (1997) as a function of the dimensionless wall distance, y^+ . In this study, the wall-normal velocity fluctuation is of special interest:

$$v'^{++} = \frac{0.0116y^{+2}}{1 + 0.203y^+ + 0.0014y^{+2.421}}.\tag{4.20}$$

The results are obtained at $Re = 13,000$ based on the channel height. The expression is valid up to $y^+ = 200$.

4.3 Near-Wall Velocity Profiles

The presence of walls and the no-slip condition makes the velocity and temperature profiles complex and difficult to reproduce analytically as well as numerically. For simplicity, the flow close to walls is separated into different regions based on the dominant physical mechanisms of the flow. White (2019) explains an inner layer, where viscous shear dominates, an outer layer, where turbulent shear dominates, and an overlapping layer, where both types of shear are important. Spalding (1961) has constructed a single composite formula that cover the inner wall region from the *viscous sublayer* ($y^+ \leq 5$), through the *buffer layer* ($5 \leq y^+ \leq 30$) and the *log-law* region ($y^+ \geq 30$) to where the outer layer begins to be significant (usually $y^+ > 100$)

$$y^+ = u^+ + e^{-\kappa B} \left[e^{\kappa u^+} - 1 - \kappa u^+ - \frac{(\kappa u^+)^2}{2} - \frac{(\kappa u^+)^3}{6} \right],\tag{4.21}$$

where White (2019) adopted the data correlations of Coles and Hirst (1968), who used the values $\kappa = 0.41$ and $B = 5.0$. In the Equation (4.21) above, u^+ is the dimensionless streamwise velocity.

4.4 Heat Transfer in Fully Developed Turbulent Flows with Constant Heat Rates

For fully developed velocity and temperature profiles with constant heat rate per unit tube length, the empirical equation found in the textbook of Kays and Crawford (2011) is a good approximation for the Nusselt number in a turbulent pipe flow, for $Pr \approx 1$. The Nusselt number is then defined as

$$Nu = 0.022Pr^{0.5}Re^{0.8} \quad Re < 10^5, \quad (4.22)$$

where

$$Nu = \frac{h_{ht}L}{k_f}, \quad Pr = \frac{\nu}{\alpha} = \frac{\mu c_p}{k_f} \quad \text{and} \quad Re = \frac{\bar{u}L}{\nu}.$$

Here, Nu is the Nusselt number, Pr is the Prandtl number and Re is the Reynolds number. Further, h_{htc} is the heat transfer coefficient, L is a length scale, \bar{u} is the mean fluid velocity and k_f , ν , c_p and ρ are the respective, thermal conductivity, kinematic viscosity, specific heat rate and density of the fluid. In this study, the length scale, L , is the channel height, h . From Equation 4.22 above, the heat rate is calculated simply by

$$q = h_{htc}(T_w - T_{bulk}). \quad (4.23)$$

5 | Theory – Submicron Particle Transport and Deposition Mechanisms

A particle dispersed in a turbulent gas flow is influenced by many forces, wherein some dominate the particle's trajectory, and some are insignificant. The latter forces can be neglected to simplify numerical simulations. In the project work of Stordal (2020), most of the forces and mechanisms known from the literature were described, especially forces and mechanisms related to particle deposition. Models of them were introduced and discussed. In the following chapter, only the dominant and utilised force models in the numerical simulations are presented. For further investigation on forces and other deposition mechanisms acting on small particles dispersed in turbulent channel flows, the reader is referred to Crowe (2006) and Stordal (2020).

5.1 Forces on Particles

Particles suspended in a fluid flow may have a relative motion for several reasons. This relative motion can be related to mechanisms and forces acting on the particle. The magnitude of these depends on the fluid properties, flow properties and the properties of the particle. The mechanisms can be arranged as

- * General carrier flow effects
- * Wall bounding forces
- * Phoretic effects
- * Brownian diffusion

In the following section, the mechanisms and forces a particle is subjected to in a carrier flow are described, and relevant models are presented.

5.1.1 General Carrier Flow Effects

In the employed Lagrangian approach, the trajectory of the particle streams are computed by simultaneously integrating

$$\frac{dx_i}{dt} = v_i \quad (5.1)$$

and the equation of motion for the particle. Here, v_i and x_i represents the particle velocity and position in the i 'th direction, respectively. The equation of motion for a submicron spherical particle dispersed into a carrier fluid in a turbulent flow field can be written as

$$m_p \left(\frac{dv_i}{dt_p} \right) = F_{D,i} + F_{L,i} + F_{B,i} + F_i. \quad (5.2)$$

Here, m_p is the particle mass. Equation 5.2 describes the particle force balance as it moves along the trajectory. The term on the left-hand side is the inertia force acting on the particle due to its acceleration. The terms on the right-hand side are respectively steady-state drag, lift force, Brownian force (see Section 5.1.4 and other body forces.

Drag Forces

The drag force acting on the particles is "steady-state" when there is no acceleration of the relative velocity between the particle and the carrier fluid. The force is evaluated with the drag coefficient through the following equation (Crowe, Sommerfeld et al. 1998)

$$F_{D,i} = \frac{1}{2} \rho_f C_D A |u_i - v_i| (u_i - v_i), \quad (5.3)$$

where ρ_f is the density of the carrier fluid, C_D is the drag coefficient, v_i is the local velocity of the particle, and A is the representative area of the particle. A is often set to the projected area of the particle.

$$u_i = \bar{u}_i + u_i' \quad (5.4)$$

is the local velocity of the fluid, represented by the local mean velocity and the local fluctuating velocity, respectively. The local mean velocity taken from the RSM flow field solution, whereas the latter is modelled by the DRW model (see Section 5.1.5). In this expression of the drag force, the Faxen correction term is neglected, given the submicron size of the particle size examined in this study (Ounis and Ahmadi 1990).

In this study, the particles are assumed to be spherical for simplicity. The drag coefficient depends on the particle size, d_p , and the particle Reynolds number, which is defined as

$$Re_p = \frac{d_p |u_j - v_j|}{\nu_f}, \quad (5.5)$$

where ν_f is the fluid kinematic viscosity. For low particle Reynolds numbers, the drag coefficient varies inversely with Re_p , which is defined as the Stokes flow regime:

$$C_D = \frac{24}{Re_p C_c}, \quad (5.6)$$

where C_c is the correction for rarefied gas, described below. For particle Reynolds numbers approaching and exceeding unity, Crowe (2006) recommended the correlation of Schiller and Nauman (1933)

$$C_D = \frac{24}{Re_p C_c} (1 + 0.15 Re_p^{0.687}), \quad (5.7)$$

in the range $1 < Re_p < 800$.

Crowe, Sommerfeld et al. (1998) presented some correlations on how turbulent intensity affects drag coefficient in sub-critical turbulent flow, i.e. relative low particle Reynolds number. However, the standard drag curve is recommended due to the lack of validation and experimental data of these correlations.

Turbulent Dispersion

By assuming a one-way coupling between the fluid flow and the Lagrangian particles, the fluid flow turbulence only affects the particle behaviour and not the other way around. Hence, the results from the steady Reynolds stress transport model for the turbulence establishes the basis for how particles are affected by the eddies. One of the limitations of solving the RANS equations is the resulting mean values of the Reynolds stresses. Consequently, the instantaneous fluctuating components of the fluid flow need to be modelled. In other words, the first term on the right-hand side of Equation 5.4 is known, and the second term needs to be modelled. The two most commonly used modelling approaches are the discrete random walk (DRW) and the continuous random walk (CRW). These are introduced in Section 5.1.5.

Rarefied Gas Effects

In a particle-laden flow where the particle diameter, d_p , is approaching the same order of magnitude as the mean free path of the gas, λ , the gas surrounding a particle may not be considered to be a continuum. Therefore, drag forces on the particle are different from continuum flows. The degree of rarefaction is characterised by the Knudsen number:

$$Kn = \lambda/d_p. \quad (5.8)$$

Four different rarefied gas regimes are described in the project work of Stordal (2020). In Crowe (2006), the mean free path of air is defined as (Crowe, Drossinos et al. 2006),

$$\lambda_{air} = \lambda_{0,ref} \left(\frac{101}{p} \right) \left(\frac{T}{293} \right) \left(\frac{1 + 110/293}{1 + 110/T} \right), \quad (5.9)$$

where, T and p are the mean temperature and pressure of the fluid flow, respectively. Here, $\lambda_{0,ref} = 0.0664 \mu\text{m}$ for ambient conditions. For other gases, like water vapour, determining the mean free path from kinetic theory is difficult according to Crowe, Drossinos et al. (2006) and Guha (1997). A good approximate formula is presented,

$$\lambda = \frac{\mu_f}{p} \left(\frac{\pi RT}{2} \right)^{1/2}. \quad (5.10)$$

Here, R is the specific gas constant of the fluid and μ_f is the dynamic viscosity of the fluid. In general, in the regimes where the Knudsen number is approaching and exceeding unity, a correction factor is employed:

$$C_c = 1 + Kn \left(2.514 + 0.8e^{-(0.55/Kn)} \right) \quad (5.11)$$

where C_c is the Cunningham correction factor. The correction expression is presented by Davies (1945) and this definition is utilised by Fluent (2021b) and Tian and Ahmadi (2007), among others. In this paper, the slip correction (C_c) to the rarefaction of the gas is assumed to give good results for drag forces, even in the free molecular regime ($Kn > 10$), as outlined in the project work (Stordal 2020).

Lift Forces

The lift force is considered as a general carrier flow effect. This force is related to the effect of gravity, and therefore often depends on the orientation and direction of the flow. As a result of the no-slip condition and velocity gradient in the near-wall region, it exists a velocity difference over the particle. This results in a lift force directed towards the wall.

Saffman (Saffman 1965; Saffman 1968) introduced an expression for the shear-induced lift force, which is referred to as the "Saffman lift force" in literature. Li and Ahmadi (1992) examine submicron spherical particles in a turbulent channel flow and employed a generalisation of the original expression, defined as

$$\frac{F_{L,i}}{m_p} = \frac{\rho_f 2K \nu_f^{1/2} d_{ij}}{\rho_p d_p (d_{lk} d_{kl})^{1/4}} (u_j - u_j^p), \quad (5.12)$$

where $K = 2.594$ and d_{ij} is the deformation rate tensor defined as

$$d_{ij} = \frac{1}{2} \left(\frac{\partial u_i}{\partial x_j} - \frac{\partial u_j}{\partial x_i} \right). \quad (5.13)$$

The lift force is restricted to small Re_p (Fluent 2021b; Li and Ahmadi 1992). In addition, Li and Ahmadi (1992) requires that the shear field is substantial compared to the slip velocity, i.e. $Re_p < \sqrt{Re_\tau}$, in order for the lift force to be significant. Here, $Re_\tau = u_\tau L / \nu$, with L as a length scale. Calculations on the effect of F_L generally show enhanced deposition velocity, especially in the eddy diffusion-impaction regime Guha (2008). However, since the direction of the Saffman lift force depends on the relative velocity, it is highly influenced by gravity, and the direction of it, as examined in Guha (1997) and Tandberg (2017).

One of the assumptions made by Saffman (1965) in the derivation of his results was the presence of an unbounded shear flow, in other words, the results is not derived for a wall bounded shear flow (Guha 2008). Nevertheless, it is included in the calculations of Li and Ahmadi (1992) and Tian and Ahmadi (2007) in bounded shear flows, as it offers good estimations for small particles.

5.1.2 Wall Bonding Forces

Near the wall, body forces emerge, e.g. electrostatic forces and van der Waals forces. These are forces that act throughout the volume of the particle, in contradiction to contact forces that act on the particle surface. The wall bounding forces are dominant in the vicinity of the wall but are cumbersome to determine correctly. Below, a leading model theory is presented.

The DLVO Theory

The surface charges of silica particles are complex. Monomers have a neutral charge, whereas nuclei and polymers have an overall negative surface charge. Therefore, monomers are the dominant growth species, and the nuclei and polymers attachment to surfaces and other particles will be limited by electrostatic repulsion (van den Heuvel et al. 2018). If a layer of silica particles are deposited on the wall, further deposition of silica can be limited by electrostatic repulsion.

The DLVO theory attempts to model the combination of the attractive and repulsive forces on a particle suspended in a liquid solution. It predicts a probability for two particles to form a bond. Near the wall, deposited particles of silica bond together and interactions between dispersed particles and the wall can be modelled as particle-particle interactions. These interactions mainly consist of long-range electrostatic repulsion forces, as the silica particles carry the same surface charge and inter-molecular (van der Waals) attraction. In order for a particle to deposit on the wall, it must overcome the potential barrier related to the electrostatic surface tension, or the so-called electrical double layer forces (Kokhanenko 2014). The DLVO interaction potential is given as

$$V_{DLVO} = V_{vdW} + V_{EDL} \quad (5.14)$$

where V_{vdW} is the attractive van der Waals potential and V_{EDL} is the repulsive electrostatic potential. The van der Waals potential is a function of the Hamaker constant for the interaction of the silica particles in water vapour. A reference to this constant for silica particles in steam is not found in the literature, and it is preferably determined experimentally. Likewise, the electrical potentials of the particle and the wall, or the zeta potentials, need to be determined experimentally to give reasonable estimates to V_{EDL} . In other words, the DLVO interaction potential is cumbersome and complex to determine correctly. In addition, this theory is based on liquid as a carrier fluid, and potential discrepancies with water vapour as carrier fluid is not established in the literature.

Kokhanenko (2014) attempts to include the DLVO theory in the numerical model to determine the deposition velocity of silica particles dispersed in liquid water. Here, the DLVO interaction potential was estimated based on typical values for zeta potentials in geofluids, and the Hamaker constant was determined theoretically. Based on these estimates, the numerical model predicted five orders of magnitude lower deposition velocity for the silica particles than experimental measurements. Kokhanenko (2014) related these discrepancies to the uncertainties related to the rebounding effect of the wall bounding forces. In the present numerical study, these wall bounding forces are not included.

Generally, it is assumed that at pH below 7 the repulsive force between the 2.5 nm particles is very low. The repulsive force will increase as the particle size increase, reducing the collision efficiency.

5.1.3 Phoretic Effects

Thermophoretic Forces

Particles suspended in a fluid with a temperature gradient tend to migrate from the hotter regions towards the colder regions. This transport is due to local temperature differences over the particle, where the hotter region contains fluid molecules with higher energy and momentum than the colder region. This "bombardment" results in a macroscopic transport of particles in the direction of the decreasing temperature (Crowe, Drossinos et al. 2006). The thermophoretic force is defined in Fluent (2021b) as follows

$$\frac{F_{th,i}}{m_p} = -\eta_T \frac{1}{m_p T} \frac{\partial T}{\partial x_i}, \quad (5.15)$$

where η_T is the thermophoretic coefficient and $\frac{\partial T}{\partial x_i}$ is the thermal gradient in the i 'th direction. The two most important parameters for the magnitude of the thermophoretic coefficient are the thermal conductivity ratio, $\Lambda = k_p/k_f$, and the Knudsen number, Kn .

In the present study, interpolation formulas for η_T are employed, which are expressions valid for a wide spectre of Knudsen numbers. The two formulations of Talbot et al. (1980) and Young (2011) are introduced in the project work (Stordal 2020). The variation of these formulations with Kn is illustrated in Figure 5.1. Here, the thermal conductivity ratio is set to 28, for the case considered ($p = 50$ bar). The particles sizes evaluated in this study is depicted with blue lines. In the figure, the two expressions estimate similar η_T for $Kn > 1$. Large discrepancies between the models are, however, observed for $0.01 < Kn < 0.6$. For the particles considered, the expression of Talbot et al. (1980) predicts the highest thermophoretic coefficient for $d_p = 5$ nm and 20 nm.

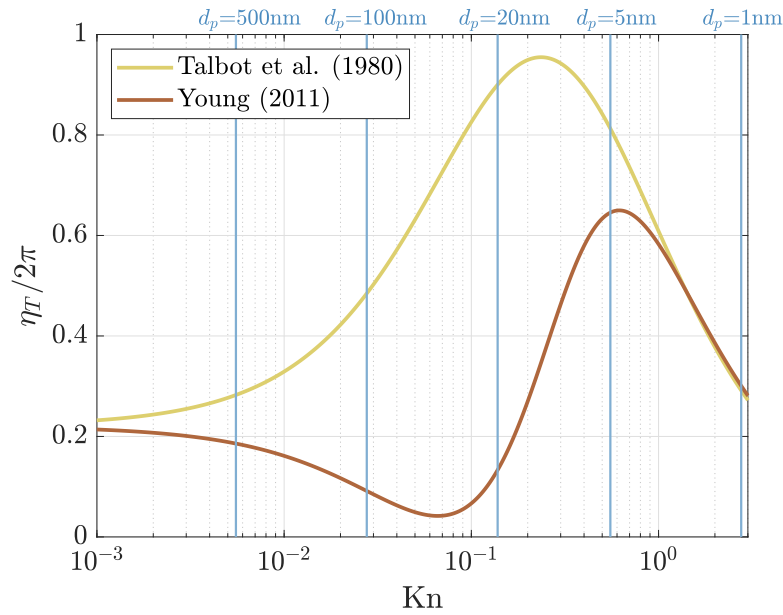


Figure 5.1: The thermophoretic coefficient, η_T , is expressed as a function of Kn for the interpolation formulas of Talbot et al. (1980) and Young (2011). Evaluated particle diameters are depicted with blue lines.

There are two main reasons why thermophoresis is accounted for in the present study. Firstly, geothermal production pipes can have severe temperature gradients, which need to be accounted for numerical modelling (Fridriksson et al. 2015; Karlsdottir et al. 2014). Secondly, experiments may be performed with small thermal gradients, and its effect on deposition need to be accounted for in the models. Additionally, the thermal conductivity of superheated water vapour is higher than the thermal conductivity of air at ambient conditions. This results in a lower value for the thermal conductivity ratio, Λ , which is related to higher effects of thermophoresis (Kleinmans et al. 2018).

Turbophoresis

Particles of submicron size are often characterised by small Stokes numbers, which is defined in Equation 5.32. The low inertia of the particles makes the particle trajectory identical to fluid streamlines. If a turbulent flow is fully mixed, a normalised concentration profile of unity is expected (Mofakham, Ahmadi and J. McLaughlin 2018).

For larger particles with Stokes number approaching unity, inertia is more significant, and the particle trajectory can depart from the fluid streamline. The probability of a particle being thrown towards or away from the wall at a specific location is the same. However, due to the magnitude of turbulent intensity, the probability of a particle being thrown away from a region with low turbulent intensity, e.g. the wall region, is less than the probability of a particle being thrown into the wall region from a region with high turbulent intensity, e.g. the core region. In total, this leads to a net macroscopic

particle transport towards the wall, against the gradient of turbulent intensity Guha (1997). This particle transport mechanisms is called turbophoresis and is dominant in the eddy-diffusion impaction regime (Guha 2008) (see Figure 5.3). Consequently, the deposition regime of the particle can be characterised by the particle concentration profile.

5.1.4 Brownian Diffusion

The particles are subjected to the dominant turbulent dispersion in the core flow of a turbulent fluid flow. However, near the wall, where the turbulent intensity tends to vanish, the Brownian diffusion becomes the dominant transport mechanism for submicron particles (Qian Chen and Ahmadi 1997; Ounis, Ahmadi and J. B. McLaughlin 1993).

The dispersed particles in the vicinity of the wall are observed to have a random motion called Brownian motion due to the high number of collisions with the fluid phase molecules. Brownian motion is a diffusive mechanism on a macroscopic scale since it results in particle flux from high to low concentration regions. Diffusion of particles can be described by Fick's law in terms of the number of particles diffused,

$$J_{p,i} = -D \frac{\partial n_p}{\partial x_i}. \quad (5.16)$$

Here, $J_{p,i}$ is the the number flux in the i 'th direction [particles/ m^2/s], D is the diffusion coefficient and n_p the number of particle concentration. The diffusion coefficient is increasing for smaller particles, D being inverse proportional to the particle diameter and proportional of the Cunningham correction factor, C_c . Crowe (2006) defines the diffusion coefficient of small particles as

$$D = \frac{k_B T C_c}{3\pi\mu_f d_p}, \quad (5.17)$$

where $k_B = 1.381 \cdot 10^{-23} \text{J/K}$ is the Boltzmann's constant, μ_f and T is the dynamic viscosity and temperature of the fluid, respectively, and d_p being the particle diameter. In the Lagrangian approach, the Brownian diffusion is often modelled as an acceleration imposed on particle trajectories. From Fluent (2021b),

$$\frac{F_{bi}}{m_p} = \zeta_i \sqrt{\frac{\pi S_0}{\Delta t}}. \quad (5.18)$$

Here, the F_{bi} is modelled as a Gaussian white noise random process, where ζ_i are independent zero-mean Gaussian random numbers. The spectral intensity of the Brownian force is given by (Fluent 2021b; Tian and Ahmadi 2007)

$$S_0 = \frac{216\nu_f k_B T_f}{\pi^2 \rho_f d_p^5 S^2 C_c}, \quad (5.19)$$

where $S = \rho_p/\rho_f$ is the density ratio. Notice that $F_b \sim d_p^{-5/2} C_c^{-1/2}$, meaning that the magnitude increases significantly with smaller particle sizes and decreases with the fluid rarefaction.

5.1.5 Discrete and Continuous Random Walk Models

The stochastic DRW and CRW are two widely accepted approaches to generate the instantaneous fluid velocity fluctuations. In the DRW model, the generated instantaneous velocity fluctuation is kept constant during the lifetime of an eddy. When this eddy lifetime has elapsed, a new velocity fluctuation is produced, independent of the previous one. In other words, velocity fluctuations are discontinuous in time in this approach. The CRW model bypasses the discrete result by using the Langevin equation. Then, effects of instantaneous fluid velocity fluctuations on particle trajectories can be simulated (Mofakham and Ahmadi 2019). The two different model approaches are depicted in Figure 5.2.

Although the CRW model introduces turbulent fluctuations more similar to experimental data, the performance of the most accurate DRW and CRW models by Mofakham and Ahmadi (2020) are roughly identical. The CRW is more computationally intensive than DRW (Bocksell and Loth 2001), and it is not standard in ANSYS Fluent. Therefore, code implementation is needed, a code that is neither open

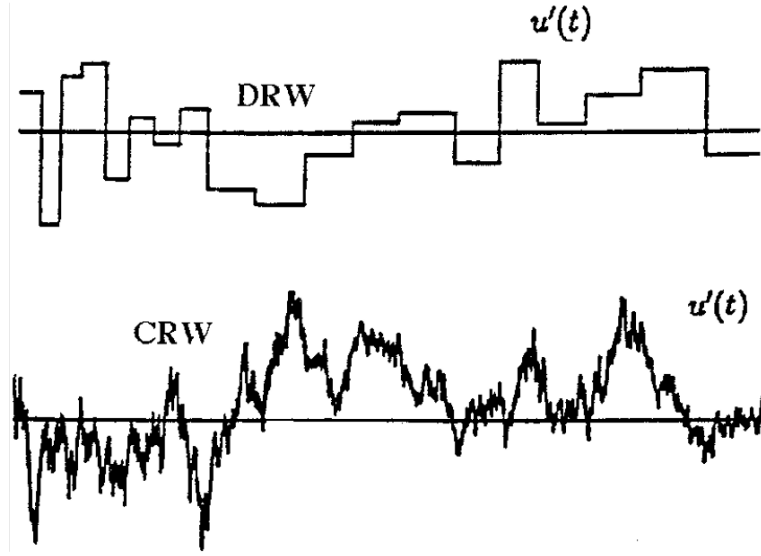


Figure 5.2: Comparison of typical velocity fluctuation histories for the DRW and CRW models. The figure is taken from Bocksell and Loth (2001).

source nor self-evident. In this study, the DRW approach is employed, with the aim of improving the accuracy compared to the conventional-DRW, which is standard in ANSYS Fluent. Model developments can be done by introducing the proposed improved-DRW of Mofakham and Ahmadi (2020) using a User Defined Function (UDF). The included UDFs in this study are inspired by the conventional-DRW UDF implementation of Longmire (2007). The two different discrete random walk models are used and compared in this study for including the effects of the turbulent fluctuations on the particle dispersion and deposition.

The DRW is also called an eddy lifetime model. The modelled eddies are characterised by

- Gaussian distributed random instantaneous velocity fluctuations: u' , v' and w'
- a time scale, τ_e

Here, u' , v' and w' are the respective instantaneous fluctuating velocities in the x , y and z direction and τ_e is the lifetime of an eddy.

Conventional-Discrete Random Walk

In ANSYS Fluent, the instantaneous velocity fluctuations, that prevail during the eddy lifetime, are modelled assuming they obey a Gaussian probability distribution. In the i -direction, it yields,

$$u_i'^{n+1} = \zeta_i \gamma_i, \quad (5.20)$$

where ζ_i are independent Gaussian random numbers with zero mean and unit variance, and $\gamma_i = \sqrt{u_i'^2}$ are the mean velocity fluctuations as obtained from the RSM simulation. The time scale, τ_e , is related to each eddy and can be defined as a random variation or a constant. As a constant,

$$\tau_e = 2T_L, \quad (5.21)$$

where the T_L is the particle Lagrangian integral time scale, which, for the k - ε turbulence model variations, can be expressed as (Fluent 2021b)

$$T_L = C_L \frac{k}{\varepsilon}. \quad (5.22)$$

Here, the ε is the turbulent dissipation rate, and k is the turbulent kinetic energy. The value of the C_L is not universal and is obtained by experimental data (Gao et al. 2012) or with a calibration methodology (Mozafari 2014). As a random variation about T_L , the eddy time scale is defined as

$$\tau_e = -T_L \ln \zeta_u, \quad (5.23)$$

where ζ_u is a uniformly distributed random number between 0 and 1. In the present study, the constant relation is employed, as Tian and Ahmadi (2007) reported no improvement with Equation 5.23 compared to Equation 5.21, but additional computational cost. Along the particle path, γ_i varies and is updated each time-step based on the particle position. Similarly, τ_e is updated as k/ε varies. A new stochastic eddy is generated by Equation 5.20 after the eddy interaction time, t_{int} . In Fluent (2021b), this is defined as

$$t_{int} = \min(\tau_e, t_{cross}) \quad (5.24)$$

where t_{cross} is the particle crossing time which is the time a particle needs to cross an eddy as a result of its slip velocity (Mofakham and Ahmadi 2020). The particle eddy crossing time is defined as

$$t_{cross} = -\tau_p \ln \left[1 - \left(\frac{L_e}{\tau_p |u_j - v_j|} \right) \right], \quad (5.25)$$

where τ_p is the particle relaxation time, L_e is the eddy length scale and $|u_j - v_j|$ is the magnitude of the relative velocity. The t_{cross} is essential for estimating the interaction between the particle and the carrier fluid. For low inertia particles, i.e. submicron particles, the particle eddy crossing time is often long. Therefore, calculating the eddy lifetime, τ_e , plays a dominant role in calculating the particle-fluid-interaction time. For higher inertia particles, the particle-fluid-interaction time is shorter than the eddy lifetime since such particles will likely depart from the fluid streamline. Modelling this interaction time is essential for predicting the concentration profile and deposition on the wall correctly (Fluent 2021b).

Observe that, $\tau_e \sim C_L$, which is not a universal constant. Milojević (1990) reported that $C_L \in [0.0675, 0.205]$ and that the determination of this constant is critical. The Lagrangian time scale constant influences the dispersion of particles across the channel low. For a high value, the particle interacts longer with the eddy and is dispersed to a higher degree, whereas for a low value, the particle is less dispersed. The reported interval of C_L is based on experiments of Snyder and Lumley (1971) on lab-scale, i.e. lower Reynolds numbers. For higher Reynolds turbulent flows, Mozafari (2014) reported that application of calibration methods leads to changes of the time-scale values of up to 94%, so that $C_L \in [0.01, 0.29]$. Most of the current literature either employ the default value or utilise calibration methods to determine the time scale constant. As indicated, a universal value for a turbulent channel flow is not found.

Improved-Discrete Random Walk

The stochastic random walk models were originally developed for homogeneous turbulent flows. By employing these models for predicting particle dispersion in inhomogeneous turbulent flows, a spurious mean drift of particles toward regions with smaller turbulence intensity occurs (Bocksell and Loth 2001; MacInnes and Bracco 1992; Mofakham and Ahmadi 2020; Wilson et al. 1981). As a consequence, a higher concentration of particles is observed in the near-wall region. The improved-DRW model by Mofakham and Ahmadi (2020) incorporates a mean drift velocity correction term, $\overline{u_i^{m+1}}$ in Equation 5.20 to rectify this issue:

$$u_i^{m+1} = \zeta_i \gamma_i + \overline{u_i^{m+1}}, \quad (5.26)$$

where

$$\overline{u_i^{m+1}} = \overline{u_i^m} + \frac{1}{1 + Stk} \left(\underbrace{\gamma_i \frac{\partial \gamma_i}{\partial x_j}}_{(A)} - \underbrace{\frac{\gamma_i^2}{T_L} \frac{\partial T_L}{\partial x_j}}_{(B)} \right) \Delta t. \quad (5.27)$$

The mean fluctuating velocity components, $\sqrt{u_i'^2}$, are here represented by γ_i . Stk is the Stokes number (see Equation 5.32) and Δt is the particle time step. In Equation 5.27, term (A) is included to improve the distribution of particles in inhomogeneous turbulent flows and is a function of the turbulence velocity gradient. Term (B) is included to reduce the effects of time-scale inhomogeneities and is a function of the

gradient of the Lagrangian time scale. Stk is the Stokes number and is introduced below in Equation 5.32. The drift term in Equation 5.27 is calculated during the lifetime of an eddy. It is summed over the time steps until the particle residence time reaches the eddy interaction time. A new random number ζ_i is then generated, and a new drift term is evaluated.

In addition, Mofakham and Ahmadi (2020) use the expression of Kallio and Reeks (1989) for the Lagrangian integral time scale:

$$T_L^+ = \begin{cases} 10 & \text{if } y^+ \leq 5 \\ 7.122 + 0.5731y^+ - 0.00129y^{+2} & \text{if } 5 < y^+ < 200 \end{cases} \quad (5.28)$$

The expression is widely used and curve-fitted based on experimental data by Laufer (1953) from a fully developed turbulent pipe flow. Moreover, Equation 5.28 varies with the turbulence kinetic energy, k , the dissipation rate, ε , and lastly it varies with the wall-normal turbulent Reynolds number, as introduced by Sato and Yamamoto (1987). In addition, measurements of the near-wall region and studies of turbulent burst events have indicated that the time scale is approximately constant for $y^+ \leq 5$ (Kallio and Reeks 1989).

5.2 Deposition of Micron and Submicron Particles

5.2.1 Relevant Parameters

Particle Relaxation Time

The particle relaxation time, also called the velocity response time, is a time scale representing the adjustment of the particle velocity to a changing fluid velocity. It is related to the acceleration time from a still situation to reaching the fluid velocity. For a spherical submicron particle, the rarefied gas effect must be taken into account, introducing the Cunningham correction factor, C_c , in the definition. The particle relaxation time is commonly defined as

$$\tau_p = \frac{\rho_p d_p^2}{18\mu_f} C_c, \quad (5.29)$$

where ρ_p and d_p are density and diameter of the particle, respectively. μ_f is the dynamic viscosity of the carrier fluid. Furthermore, the dimensionless relaxation time is

$$\tau_p^+ = \frac{\tau_p u_\tau^2}{\nu_f}, \quad (5.30)$$

where u_τ is the friction velocity and ν_f is the kinematic viscosity of the fluid.

Deposition Velocity

Particle deposition is often described as a dimensionless deposition velocity. Based on the expression presented by Kallio and Reeks (1989), we obtain

$$V_d^+ = \frac{hU_{avg}}{2u_\tau \Delta x} \ln \frac{M_{in}}{M_{out}} \quad (5.31)$$

for a straight two-dimensional channel. Here, h is the channel height, U_{avg} is the mean fluid velocity, u_τ is the friction velocity, Δx is the channel increment in the stream-wise direction, and M_{in} and M_{out} is the respective number of particles in and out of the increment. This expression for the dimensionless deposition velocity is used in this study. The reader is referred to the project work of Stordal (2020) for the derivation of the expression.

Stokes Number

The Stokes number relates the response time of the particles to the characteristic time associated with the flow field: $Stk = \tau_p / \tau_f$. For $Stk \ll 1$, the response time of the particles is short compared to the

flow, i.e. the particles have time to respond to changes in the flow and will follow the streamlines. On the contrary, if $Stk \gg 1$, the particles do not have the time to respond to the changes in the flow. Hence the particle velocity will not be affected by the changes in the fluid flow. The Stokes number is defined as the ratio of the particle stopping distance to a characteristic length, L , (Crowe 2006):

$$Stk = \frac{S_L}{L} = \frac{u_{avg}\tau_p}{d_h}. \quad (5.32)$$

Here, u_{avg} is the averaged fluid velocity. For the channel flow examined in this study, the chosen characteristic length, L , is the hydraulic diameter, d_h .

Schmidt Number

The Schmidt number is defined as the ratio of momentum diffusivity to mass diffusivity and is a dimensionless number related to the thickness of the concentration boundary layer, defined as

$$Sc = \frac{\nu_f}{D}, \quad (5.33)$$

where D is the diffusion coefficient found in expression (5.17) .

5.2.2 Particle Deposition Regimes

In Figure 5.3, the logarithmic variation of the dimensionless deposition velocity, V_d^+ , is plotted against the logarithmic variation of the dimensionless relaxation time, τ_p^+ . Based on the literature, here from the empirical results of Fan and Ahmadi (1993) and the experimental results collected by Papavergos and Hedley (1984), three different particle deposition regimes can be drawn. These results are introduced in the subsections below. The trends in the three regimes are related to the mechanisms dominating the particle motion in the near-wall region. For short particle relaxation times, the particles are dominated by turbulent and Brownian diffusion in the vicinity of the wall. This first region is therefore termed the diffusion-dominated regime. The second regime is called the eddy-diffusion-impaction regime. Here, the particles grow large enough for the eddies to transfer momentum onto the particles from the core flow. The particles of high inertia are 'thrown' into the viscous sublayer towards the wall. This effect is increasing with particle mass; hence the deposition velocity is increasing with particle diameter. In the third regime, the inertia-dominated regime, the particles are dominated by inertia imposed by the turbulent fluctuations in the core and high deposition rates are observed.

5.2.3 Experimental Data on Particle Deposition

Experimental measurements on particle deposition in the diffusion-dominated regime are scarce in the literature. Papavergos and Hedley (1984) collected and reviewed earlier experimental measurements of particle deposition in horizontal and vertical flows. The data collection of vertical flow measurements are depicted in Figure 5.3 as red dots. Shimada et al. (1993) performed deposition measurements in a 6 mm pipe flow for Reynolds number ranging between 4120 and 9550 with particle sizes from 10 to 43 nm. The pipe roughness in the experiments is not reported. The data points are collected from figure 9 in the paper of Shimada et al. (1993), recalculated, made dimensionless by known variables and presented in Figure 5.3. The temperature is assumed to be $T = 25^\circ\text{C}$. The experimental data from Chauhan (2019) on horizontal particle deposition measurements in superheated water vapour are also included in Figure 5.3. The experimental conditions are described in Chapter 8. Chauhan (2019) investigated deposition from 1 to 20 μm .

5.2.4 Particle Semi-Empirical Model Predictions

Wood (1981) used an Eulerian calculation method to develop good estimates of the deposition velocity in smooth surfaces:

$$V_d^+ = \frac{3\sqrt{3}}{29\pi}(Sc)^{-2/3} + 4.5 \times 10^{-4}\tau_p^{+2}. \quad (5.34)$$

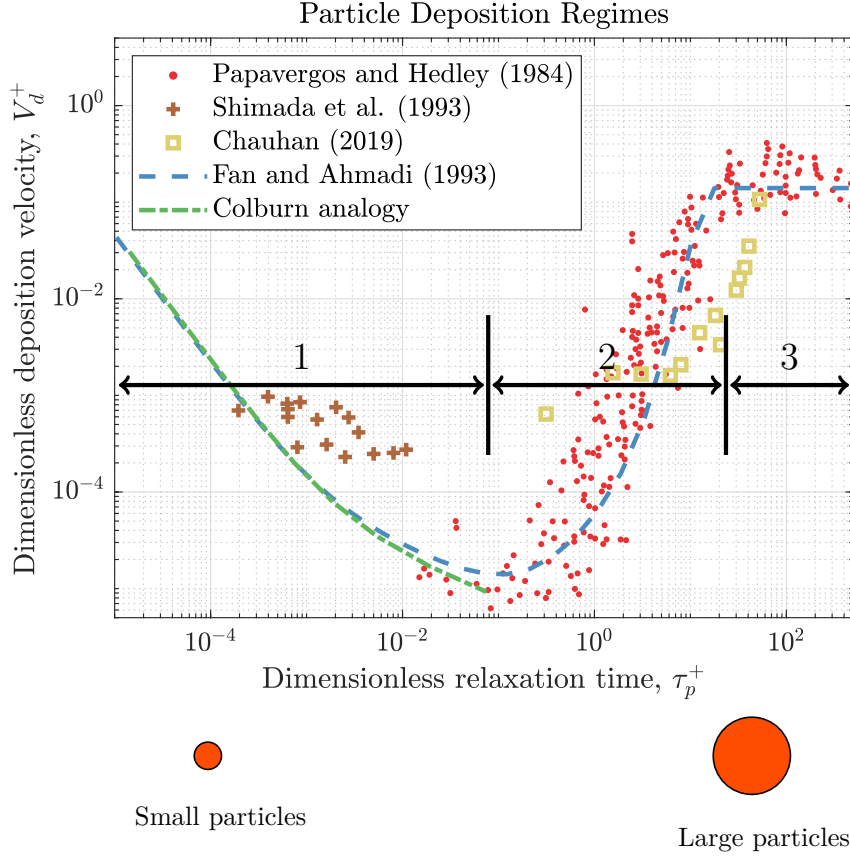


Figure 5.3: Particle deposition regimes: (1) the diffusion-dominated regime, (2) the eddy-diffusion-impaction regime and (3) the inertia-dominated regime.

Here, Sc is the Schmidt number from expression (5.33) and τ_p^+ the dimensionless particle relaxation time found in expression (5.30). This empirical equation is widely used in the literature and is valid for $\tau_p^+ < 10$, i.e. in the diffusion-dominated and eddy-diffusion-impaction regimes. Further development in literature leads to the model of Fan and Ahmadi (1993) of vertical ducts. Here, the effects of surface roughness and gravity along the flow have been included in the model, which reads

$$V_d^+ = \begin{cases} 0.084Sc^{-2/3} + \frac{1}{2} \left[\frac{(0.64k^+ + \frac{g^+}{2})^2 + \frac{\tau^{+2}g^+L_1^+}{0.01085(1+\tau^{+2}L_1^+)}}{3.42+\tau^{+2}g^+L_1^+/0.01085(1+\tau^{+2}L_1^+)} \right]^{\frac{1}{1+\tau^{+2}L_1^+}} \times \left[1 + 8e^{-(\tau^+-10)^2/32} \right] \frac{0.037}{1 - \tau^{+2}L_1^+ \left(1 + \frac{g^+}{0.037} \right)}, & \text{if } V_d^+ < 0.14 \\ 0.14, & \text{otherwise} \end{cases} \quad (5.35)$$

where k^+ , d^+ and g^+ are the dimensionless surface roughness, particle diameter and gravity, respectively. $L_1^+ = 3.08/(Sd^+)$ for S being the particle-to-fluid density ratio. It is clear from Figure 5.3 that the correlation of Fan and Ahmadi (1993) follows the trend of the experimental data collected by Papavergos and Hedley (1984) well for $\tau_p^+ < 10^{-2}$.

Analogy to Heat Transfer

The basic mechanisms and mathematics of heat, mass and momentum transfer are quite similar when diffusion is the dominant mechanism. The Colburn J-factor analogy is a successful and widely used

analogy between heat, momentum and mass transfer. Here, the relationship between heat and mass is written as,

$$\frac{Sh}{Re \cdot Sc^{1/3}} = \frac{Nu}{Re \cdot Pr^{1/3}}, \quad (5.36)$$

where Sc is given in expression 5.33 and Sh is the Sherwood number, also called the mass transfer Nusselt number. It is defined as

$$Sh = \frac{h_N}{D/L}, \quad (5.37)$$

where h_N is the convective mass transfer film coefficient, used to calculate the mass transfer, D is mass diffusivity, as defined in Equation 5.17 and L is a length scale. Nu is the Nusselt number from Colburns formulation for the for fully-developed turbulent flow, given as (Colburn 1993)

$$Nu = 0.023Pr^{1/3}Re^{0.8}. \quad (5.38)$$

The expressions (5.38) and (5.36) are valid for $Pr_f > 0.6$ and $Re > 10,000$ (Geankoplis 2003). The Colburns analogy is depicted in Figure 5.3 in the diffusion regime, and included as a reference to the results obtained in Chapter 9. Here, the dimensionless deposition velocity is obtained by

$$V_d^+ = \frac{h_N}{u_\tau}. \quad (5.39)$$

Thermophoresis

He and Ahmadi (1998) introduced an additional term to the empirical expression (5.35) to account for thermophoresis. In dimensional terms, it reads

$$U_{th} = \frac{F_{th}}{m_p} \tau_p, \quad (5.40)$$

where U_{th} is the additional deposition velocity enhanced by the thermophoretic force. Here, F_{th} is based on the formulation of Talbot et al. (1980) and the temperature gradient at the wall is evaluated as

$$\left. \frac{dT}{dy} \right|_w \approx \frac{u_\tau^2 (T_{bulk} - T_w)}{\nu_f (U_{avg} - 5u_\tau)}. \quad (5.41)$$

Here, T_{bulk} is the free-stream temperature, T_w is the wall temperature and U_{avg} is the mean streamwise velocity. The temperature gradient through the viscous sublayer is here assumed to follow the Prandtl analogy between heat transfer and friction coefficient (He and Ahmadi 1998).

Surface Roughness

The dimensionless sand-grain surface roughness is proven to be an influential deposition parameter for submicron particles. Even within the region for $k^+ < 2.25$, defined as hydrodynamically smooth in Fluent (2021b), significantly higher deposition rates for τ_p^+ from 0.01 to 10 were reported by Fan and Ahmadi (1993), Guha (2008) and Wood (1981).

Equation 5.35 takes the effect of slightly rough walls into account ($k^+ < 1.5$). This expression of Fan and Ahmadi (1993) is based on numerical modelling of a three-dimensional channel flow, including a flow model for near-wall turbulence structures. When shifted a certain distance, the mean flow conditions in a turbulent boundary layer near a slightly rough wall is assumed similar to that of smooth walls. Fan and Ahmadi (1993) simulated the Eulerian fluid flow field based on smooth walls and implemented a particle model to account for surface roughness. Here, the particles were taken as deposited when the particle trajectory (mass centre) reached

$$y_{rough} = k + \sigma_k - e + d_p/2. \quad (5.42)$$

Above, k is the averaged roughness height, σ_k is the standard deviation of the roughness element, e is the position of the displaced origin and d_p is the particle diameter. Fan and Ahmadi (1993) employed $e = 0.53k$ and $\sigma_k = 0.17k$. As $k \rightarrow 0$, Equation 5.42 reduces to the model for smooth walls, $y = d_p/2$.

5.2.5 An Alternative Presentation of the Results

Particle deposition results are commonly presented as a function of V_d^+ and τ_p^+ . Due to the geothermal conditions investigated in the present study, comparisons and validations with experiments performed at ambient pressures in air are not applicable. This has to do with higher diffusion rates in the cases considered, leading to lower Schmidt numbers (see Equation 5.33). In the diffusion-dominated region, as τ_p^+ becomes very small, the empirical correlations is only a function of the Schmidt number (see Equation 5.35 and Equation 5.34). Thus, by neglecting the second term in Equation 5.34, it can be shown that

$$\frac{Sh}{Sc^{1/3}} = \frac{3\sqrt{3}}{29\pi} \sqrt{\frac{C_f}{2}} Re. \quad (5.43)$$

By making this assumption, the Equation 5.43 is only valid in the diffusion-dominated regime. The results by evaluating Reynolds numbers in the range 4,000 to 11,000, the experimental measurements of Shimada et al. (1993) and the Colburn analogy using this expression, are presented in Figure 5.4. Here, the experimental measurements fit well to the theoretical predictions. The numerical and experimental results will also be evaluated using Equation 5.43 (see Chapter 9).

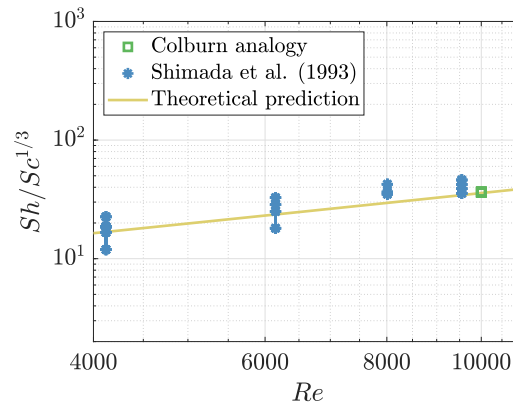


Figure 5.4: Deposition as $Sh/Sc^{1/3}$ evaluated at different Reynolds numbers. The experimental measurements of Shimada et al. (1993) and the Colburn analogy to heat transfer are also presented.

6 | Flow Modelling

In the following chapter, implementation methods, numerical residuals and grid independence of the fluid modelling in ANSYS Fluent are presented and discussed.

6.1 Properties of Water Vapour

To reduce the risk of case-sensitive results, the properties of water vapour were decided to be constant, i.e. not vary with temperature and local pressure differences. Three of the conditions presented in the experiment matrix (Table 8.1) were focused on in the numerical simulations, including the maximum and minimum pressures. The properties of water vapour implemented in the simulations for the three conditions are given in Table 6.1.

Table 6.1: Water vapour properties utilised in the fluid flow model, from the International Association for the Properties of Water and Steam (Wagner and Kretzschmar 2008).

Conditions	Properties	Units	Values
$T = 325 \text{ }^\circ\text{C}$ $p = 50 \text{ bar}$	ρ	kg/m^3	20.5
	c_p	J/kgK	2854
	k_{th}	W/mK	0.0537
	μ	$\text{Pa} \cdot \text{s}$	2.10×10^{-5}
$T = 406 \text{ }^\circ\text{C}$ $p = 150 \text{ bar}$	ρ	kg/m^3	62.4
	c_p	J/kgK	4013
	k_{th}	W/mK	0.0793
	μ	$\text{Pa} \cdot \text{s}$	2.53×10^{-5}
$T = 471 \text{ }^\circ\text{C}$ $p = 275 \text{ bar}$	ρ	kg/m^3	114.3
	c_p	J/kgK	4820
	k_{th}	W/mK	0.1099
	μ	$\text{Pa} \cdot \text{s}$	3.04×10^{-5}

6.2 Computational Model

For realistic simulation results of deposition velocity of submicron particles, an accurate calculation of the wall-normal component of the turbulence velocity in the near-wall region has proven to be essential (Stordal 2020; Tian and Ahmadi 2007). Therefore the most elaborate RANS model, the Reynolds stress transport model (RSM), is employed in this study, introducing anisotropic turbulence. A drawback with this model is the higher computational time compared to the two-equation RANS models.

In the literature, the $v^2 - f$ turbulence model outperforms the RSM model on predicting the wall-normal turbulence velocity in the wall vicinity (Mofakham and Ahmadi 2020; Zhang and Chen 2009). The $v^2 - f$ turbulence model aims at predicting the quadratic variation of the wall-normal velocity fluctuation by including transport equations for v'^2 and the production of it. By employing the open-source software OpenFOAM, Mofakham and Ahmadi (2020) showed that the $v^2 - f$ turbulence model performs much better in the vicinity of the wall compared to the RSM. However, the chosen commercial software, ANSYS Fluent, does not license this model anymore, according to their supplier in Norway, EDRMedeso.

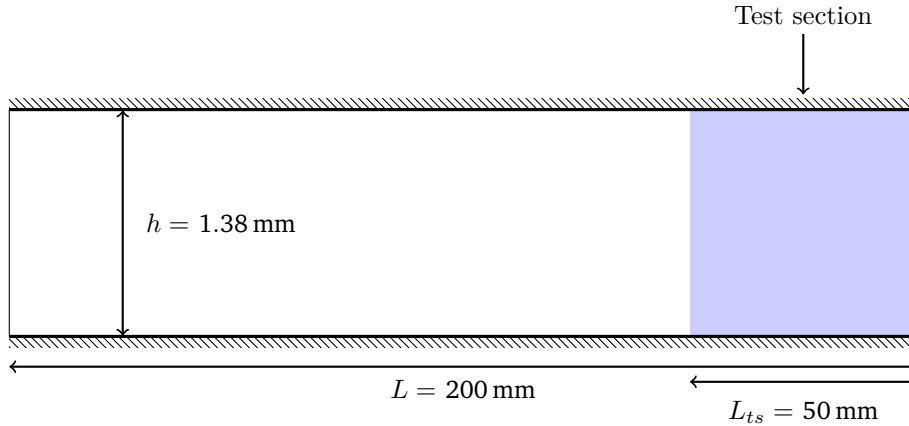


Figure 6.1: The present geometry utilised in the simulations. The illustration is not to scale.

As a consequence, the RSM turbulence model is employed. A boundary layer model for the wall-normal fluctuating velocity is added in the boundary layer in the PARTICLE model to correct for possible discrepancies. In the RSM, the linear pressure-strain model is utilised for the pressure-strain correlation (see Section 4.2), allowing the use of the enhanced wall treatment.

6.3 Simulation Setup

The simulation approach of computing an incompressible, pressure-driven, turbulent channel flow is well-known. A pressure-based steady-state solver was employed in the current simulation, as the flow is assumed incompressible and with constant density. For the pressure-velocity coupling, the Semi-Implicit Method for Pressure Linked Equations (SIMPLE) algorithm was employed. For spatial discretisation, the PRESTO!-scheme was used on the pressure, and a second-order upwind scheme was used on the remaining variables. The least-squares cell-based method is used on gradients, e.g. construct gradients at cell faces. The default values for under-relaxation has been employed in the final solutions.

6.4 Geometry and Mesh

The geometry is illustrated in Figure 6.1. It is constructed to be similar to the experiments employed in this study (see Chapter 8): $h = 1.38 \text{ mm}$ and $L_{ts} = 50 \text{ mm}$. To ensure fully developed flow and particle profiles, the total length of the geometry is $L = 200 \text{ mm}$. Most particle deposition experiments are conducted in channel flows. Henceforth, this geometry is chosen for validation purposes. In addition, this simplifies the simulation method. The Reynolds number based on average velocity and the channel width is 10,000 for all conditions, which indicates a turbulent flow. Although the experiments were originally planned to be conducted at Reynolds number 7,000 to 10,000, a similar Reynolds number for all cases are desired for verification purposes, e.g. working with one mesh for all the conditions. The shear Reynolds number is defined as

$$Re_{\tau} = \frac{u_{\tau}(h/2)}{\nu}, \quad (6.1)$$

and is about 305 for the three cases considered in the present study. This geometry is a so-called mini-channel, where the fluid flow can be assumed to follow conventional turbulent channel flow relations (Dutkowski 2008).

The enhanced wall treatment requires the first cell to be at $y^+ \approx 1$. This first cell height was estimated based on friction coefficient correlations and iterated until $y^+ \approx 1$ was reached. A grid-independent solution was ensured by comparing solutions of varying mesh resolutions. Here, the coarsest and finest mesh contains 775,000 and 63,500 number of cells, respectively. Furthermore, the particle deposition was simulated for different aspect ratios (AR) to check for consistency. The meshes were structured and

consisted of quadrilateral cells and were constructed with ANSYS Meshing Solutions. A grid convergence study is conducted in Section 6.7.

The complexity regarding flow modelling in three dimensions have not been considered in this study, e.g. the secondary flows associated with three-dimensional flows in pipes. The modelling is easier to validate and simplify by considering a two-dimensional channel flow, as fewer parameters can influence the results. Henceforth, particle dispersion and deposition modelling results are more easily trusted. In addition, the computational time is more applicable considering two dimensions.

6.5 Boundary Conditions

The inlet was set to be a velocity-inlet, and at the outlet, a pressure-outlet was imposed, i.e. the outlet is set to have zero gauge pressure and a von Neumann boundary condition. Velocity and temperature profiles based on a fully developed turbulent channel flow were set as inlet condition to develop the solution faster and reduce the computational time of the simulation. The profiles are collected from Tandberg (2017), and implemented with user-defined functions (UDFs), based on the `DEFINE_PROFILE` macro in Fluent (2021a). In addition, the turbulence intensity ($I = 0.16(Re)^{-1/8}$) and hydraulic diameter ($d_h = 2w$ for a two-dimensional channel flow) were set as inlet conditions to initiate k and ε . From Fluent (2021b):

$$k = \frac{3}{2}(UI)^2. \quad (6.2)$$

$$\varepsilon = \frac{k^{3/2}}{0.07d_h} C_\mu^{3/4}, \quad (6.3)$$

where $C_\mu = 0.09$ and U is the mean fluid flow derived from the Reynolds number and fluid properties. Based on k and ε , the boundary conditions for the Reynolds stresses, $\overline{u_i' u_j'}$, are derived. The reader is referred to Fluent theory guide (Fluent 2021b) for further information.

A constant heat rate was set at the walls as a thermal boundary condition and was estimated according to the procedure in Section 4.4. A constant heat rate boundary condition imposes a constant temperature gradient in the flow. Since the thermophoretic force is proportional to the temperature gradient (see Chapter 5), this should be constant along the channel walls to ensure unbiased results.

6.6 Numerical Residuals

In order to achieve a converged solution, the errors from solving the governing equations on the discretised forms have to be checked. These errors are called numerical residuals. In addition, average quantities were checked for convergence. The velocity profile at the outlet, the Reynolds stresses along the channel and the axial shear stress on the wall were checked for convergence. These quantities were averaged with area weights, as the velocity should generally fulfil the mass balance (continuity). The total pressure at the inlet was also checked for convergence. The pressure at the inlet is related to the pressure drop over the channel since a zero gauge pressure boundary condition is imposed at the outlet. The pressure drop results from energy dissipation and should therefore satisfy the macroscopic energy balance, which is related to the mass flux, and the inlet pressure is therefore mass-weighted. The flow simulation solution is taken to be converged when the residuals fall below the convergence criteria of 10^{-6} and when the average quantities mentioned above are constant. The latter is often limiting and delay convergence. At convergence, the normalised mass imbalance

$$\frac{\sum \dot{m}_{in} - \sum \dot{m}_{out}}{\sum \dot{m}_{in}} \quad (6.4)$$

was also checked, which in general remained below 10^{-10} . Since the expression (6.4) should be equal to zero due to mass conservation, this result can be interpreted as a confirmation of convergence.

6.7 Grid Convergence

The grid convergence can show how much the solution is affected by the grid refinement. The high gradients related to the no-slip condition at the wall require refinement in the boundary layer of the flow. Before choosing the simulation grid, a verification method must be performed to ensure that the near-wall grid cells are sufficiently small. Different meshes have been constructed with various cell sizes (N_{tot}) and growth rate listed in Table 6.2. N_x and N_y are the representative number of cells in the streamwise and the wall-normal direction. In addition, the mean wall shear stress over the test section ($x = 150 \text{ mm}$ to 200 mm) and the maximum value for the wall-normal velocity fluctuation at $x = 150 \text{ mm}$ are monitored for the different meshes for comparison. The mean wall shear stress is related to the energy dissipation, and the normal velocity fluctuation is critical for getting reasonable particle dispersion and deposition results. The wall coordinate is set to unity in all three grids, i.e. $y^+ \approx 1$ in the first cell.

Table 6.2: Grid refinement

Mesh	$h_{cell} [\text{m}]$	N_{tot}	N_y	N_x	Growth rate	$v'_{rms,max} [\text{m/s}]$	$\bar{\tau}_{wall} [\text{N/m}^2]$
Fine (1)	3.3×10^{-5}	248,000	99	2,500	1.05	5.827	57.16
Medium (2)	4.9×10^{-5}	115,000	70	1,640	1.10	5.828	57.17
Coarse (3)	6.6×10^{-5}	63,000	50	1,250	1.20	5.848	57.40

In Table 6.2, the values of the coarsest mesh differs relatively much compared to the three finest meshes. However, the absolute changes in the two monitored variables are small. Following the procedure of Celik et al. (2008) on the three coarsest meshes, the order of method is high: $p_{grid} = 10.2, 9.4$ for the $v'_{rms,max}$ and $\bar{\tau}_{wall}$, respectively. In Table 6.2, h_{cell} is the representative cell based on the channel area and the total number of cells. The grid refinement factor is defined as $r = h_{course}/h_{fine}$, where h is a representative cell of a course and fine mesh, respectively. Celik et al. (2008) recommends $r > 1.3$, and in this study, $r_{21} = 1.47$ and $r_{32} = 1.35$. The fine-grid convergence index is a standardised parameter for the numerical uncertainty and to determine the grid convergence quality. It is given as

$$GCI = \frac{F_S |e_r|}{r_{21}^{p_{grid}} - 1}, \quad (6.5)$$

where $F_S = 1.25$ is the recommended safety factor and e_r is the relative error between two grids. In Table 6.3, the grid convergence indexes are presented for the two variables, $v'_{rms,max}$ and $\bar{\tau}_{wall}$. The last refinement, represented by GCI_{12} , has a small impact on the solution, hence the small index. This indicates that further refinement is not necessary. One of the assumptions in the theory outlined in Celik et al. (2008) is that the grid values are within the asymptotic range. The constraint is verified if the following holds:

$$GCI_{23} \cong r_{21}^{p_{grid}} GCI_{12}. \quad (6.6)$$

This is checked in the last column of Table 6.3. It is concluded that the asymptotic range of convergence is achieved.

Table 6.3: Grid convergence index

Variable	GCI_{12}	GCI_{23}	$\frac{GCI_{23}}{r_{21}^{p_{grid}} GCI_{12}}$
$v'_{rms,max}$	0.0004%	0.02%	0.9998
$\bar{\tau}_{wall}$	0.0008%	0.03%	0.9998

As an additional check of grid convergence, the crucial dimensionless wall-normal fluctuating velocity in the near wall region is plotted for the different grids at $x = 50 \text{ mm}$ in Figure 6.2. To clarify the RSM model predictions, the empirical model suggested by Li and Ahmadi (1992) (see Section 4.2.2), DNS data for $Re_\tau = 395$ from Moser et al. (1999) and empirical model by Matida et al. (2000) obtained for DNS data for $Re = 13000$ are included in the figure. Figure 6.2 illustrates the similar solutions obtained by

the different meshes and also the discrepancy of the RSM model compared to DNS data. See Section 6.2 for further discussions on the latter.

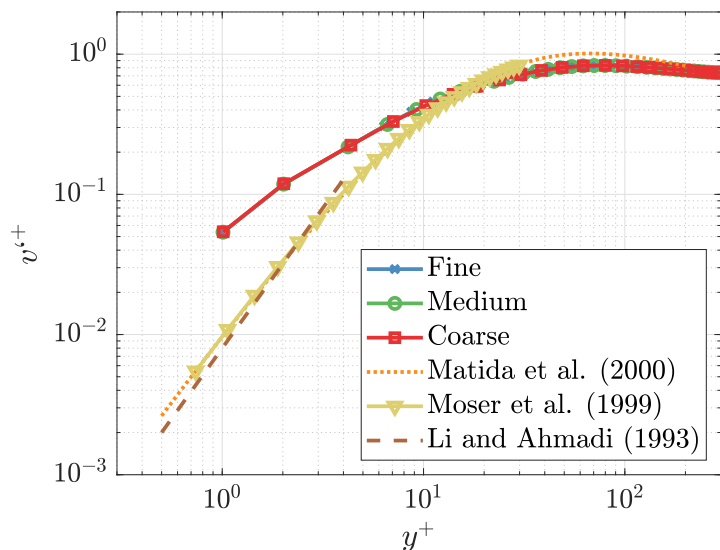


Figure 6.2: The dimensionless wall-normal fluctuating velocity plotted versus the dimensionless wall distance for the different grids at $x = 50$ mm. For assessing the performance of the RSM model predictions, the empirical model suggested by Li and Ahmadi (1992) (see Section 4.2.2), DNS data (Moser et al. 1999) and empirical model by Matida et al. (2000) are also presented.

As a conclusion to the grid convergence, the medium mesh with 70 cells in the normal direction (N_y) is deemed sufficient in this study.

6.7.1 Aspect Ratio

The cell aspect ratio is defined as the ratio of the maximum length to the minimum length in the cell. For a quadratic cell, $AR = \sqrt{1+1}/1 = \sqrt{2}$. The meshes presented in Table 6.2 were set to have an aspect ratio (AR) of four times a quadratic cell at the centre of the flow, resulting in a maximum aspect ratio of 26. Dehbi (2008) discussed particle tracking results obtained with vertical pipe meshes with different aspect ratios for $Re = 50,000$. With 30 times smaller cell count, the stretched mesh fluid flow results were almost identical to the base case. However, the agreement with the particle deposition tracking for micron-sized particles was not as good with the high aspect ratio mesh compared to the base case. This hypothesis is tested in this study.

Table 6.4: Aspect ratio grids

N_x	Centre cell AR	Maximum AR	$v'_{rms,max}$	$\bar{\tau}_{wall}$
6,672	$1 \cdot \sqrt{2}$	6.5	5.832	57.20
1,168	$4 \cdot \sqrt{2}$	26	5.828	57.17
834	$8 \cdot \sqrt{2}$	52	5.826	57.16

In Table 6.4, the number of cells are varied in the x-direction, resulting in different aspect ratios. For each mesh, the the two variables $v'_{rms,max}$ and $\bar{\tau}_{wall}$ are monitored, as in the GCI. In Figure 6.3, the dimensionless deposition velocity is plotted against the dimensionless relaxation time for particle sizes of 1 nm, 10 nm and 100 nm.

Similar to Dehbi (2008), the fluid flow results for changing the AS are almost identical. So is the particle tracking results, especially for the smallest particles. The discrepancy is increasing for bigger particles. However, since $d_p = 500$ nm is the biggest particle tracked in this study, this possible bias is concluded to be of negligible effect. In addition, as N_x increases, so is the number of particle iterations and

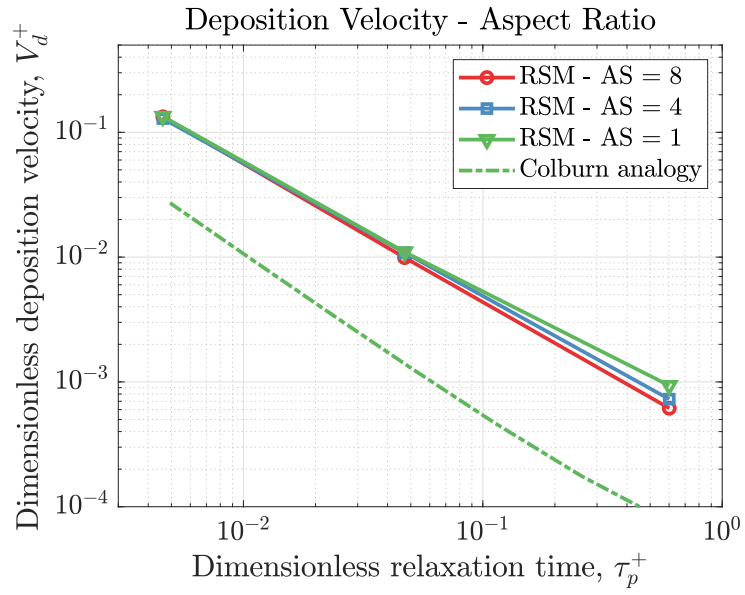


Figure 6.3: The dimensionless deposition velocity versus the dimensionless particle relaxation time for three grids of different aspect ratios. The performance is compared to the Colburn heat transfer analogy to mass transfer.

the overall computational cost. The more computationally efficient mesh with $AR = 8$ is deemed sufficient in this study, resulting in $N_{tot} = 56,000$.

7 | Particle Model

In the following chapter, some assumptions and implementation methods of the particle model are presented. The developed model for particle tracking in ANSYS Fluent consists of UDFs and is named PARTICLE for clarity.

7.1 Assumptions

Modelling of particle dispersion and deposition is complex. In order to provide a trustworthy result without too large uncertainties, simplifications of the system and the physics in it have to be made. The assumptions included below are described in Chapter 2.

7.2 Discrete Phase Model Implementation

In the Discrete Phase Model (DPM) in ANSYS Fluent, predictions of dilute phases with one-way coupling are possible. In this model the particles are simulated as moving mass points, and transport mechanisms and relevant forces are implemented (Fluent 2021b). The particulate phase is solved by tracking a large number of the so-called particle streams. Each particle stream trajectory is computed independently, and represents a big number of particles following the same trajectory. In this case, the number of particle streams tracked are significantly less than the actual particles dispersed in the geothermal water vapor flow. The modelling problem is therefore reduced to quantifying the number of particle trajectories that escape the geometry through the outlet and the number of particle trajectories that are aborted in the test section due to a contact with the walls.

The particle tracking methodology in the current geometry is illustrated in Figure 7.1. Here, the particles are depicted as red circles, the test section is coloured blue and h represents the channel height. The numbering ((i)-(v)) represents: (i) the fluid inlet; (ii) the location ($x_{inj} = 50 \text{ mm}$) of the particle injection; (iii) particle transport, where dispersed particles are allowed to develop a particle profile; (iv) the test section inlet; (v) the outlet, where also the concentration profile is captured. Over the length of the test section, L_{ts} , deposition is measured. For more details on the boundary conditions for the particulate phase, see Section 7.2.2.

In (ii), the simulated particles are included in the fluid flow as a grouped injection the DPM model. The particles are injected with linear spacing and are initiated with the velocity and temperature similar to the cell values they are located, by making use of the UDF `DEFINE_DPM_INJECTION_INIT` from Tandberg (2017).

7.2.1 Numerical Schemes and Time Step

The governing equations of the Lagrangian particle tracking approach, as described in Chapter 5, are solved numerically. The set of ordinary differential equations are solved with only one numerical scheme, as the UDFs implemented in the PARTICLE model are not prepared for utilising the default scheme combination in Fluent. As a consequence, the accuracy control cannot be employed and the numerical accuracy needs to be of special attention. In addition, the PARTICLE model is not made applicable for parallel computing, which can limit the computer resources and can potentially restrict statistical significance of the results.

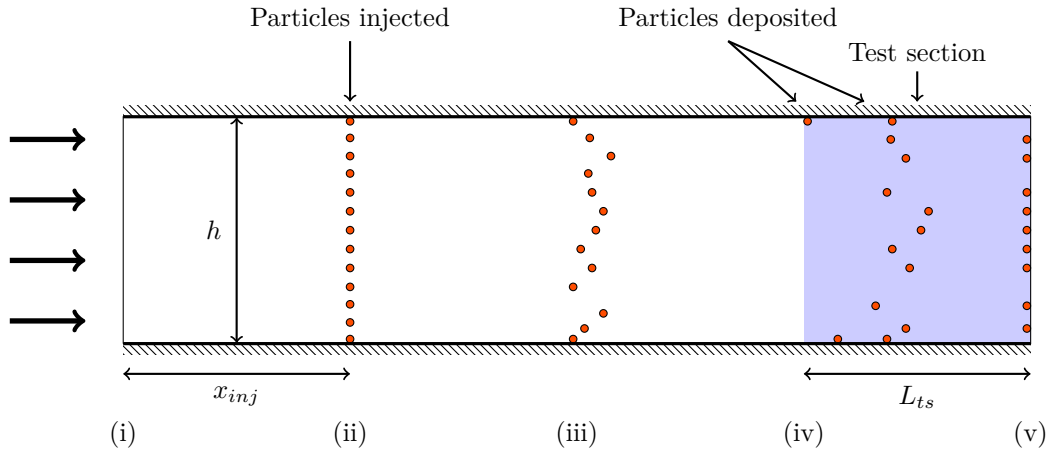


Figure 7.1: Illustration of the particle tracking with DPM in the geometry: (i) fluid inlet; (ii) linear particle injection; (iii) dispersed particles are allowed to develop a particle profile; (iv) test section inlet; (v) outlet, the concentration profile is captured. The illustration is not to scale.

To obtain an accurate and stable numerical solution can sometimes be complicated. In this study the trapezoidal and analytic numerical schemes in ANSYS Fluent DPM were employed. The first scheme is of higher order and uses a semi-implicit trapezoidal integration, which is more accurate but requires more computational time. The latter scheme is of lower order and uses an analytical integration and is faster computationally. Over the integration time step, the analytic scheme assume constant forces.

The documentation of how the particle time step is determined is scarce Fluent (2021b). If not controlled by a UDF, by experience the DPM model sets the trapezoidal scheme time step to $\mathcal{O}(\tau_p)$ (particle dependent) and the analytic scheme time step to $\mathcal{O}(\tau_e/100)$, with $\tau_e \approx 10^{-4}$. τ_p at different conditions are presented in Figure 7.4a. As a consequence, computations with the analytical scheme are much faster than the trapezoidal scheme. In the literature, Dehbi (2008) chose the integration time step to be one-tenth of the eddy lifetime (τ_e). The effect of an even smaller time step was reported to be negligible by Dehbi (2008). Matida et al. (2000) reduced the time step until no changes was observed in the results in order to ensure an unbiased solution.

Each particle diameter size was simulated with minimum 10,000 representative particle trajectories. In addition, minimum 100 deposited particles in the test section or minimum 100 escaped particles at outlet were required.

The particle deposition in 50 bar superheated water vapor condition are simulated for the analytical, the trapezoidal and a controlled time-step trapezoidal numerical schemes. In the latter scheme, the time step is restricted to be $\Delta t < \tau_p/2$. Figure 7.2 presents the relative error of the dimensionless deposition velocity simulated with the analytical and trapezoidal scheme compared to the time-step controlled trapezoidal scheme, i.e. the finest time step is used as benchmark. It should be noted that for the $d_p = 5$ nm only simulation results with the trapezoidal and analytical scheme was produced, and for $d_p = 1$ nm only simulation results with the analytical scheme was produced, due to the enormous computational time related to the small time steps ($\mathcal{O}(10^{-10})$).

No change of deposition velocity was observed for further reduction in the time step. In general, the relative error with the analytic scheme is large, increasing with particle size. The effect of large time steps and the nature of a lower order scheme intensifies deposition of particles with higher inertia. The higher order trapezoidal scheme has an overall lower relative error, but similarly the error increases with particle size. The computational cost is higher with the finest time-step. Henceforth, the accuracy of the trapezoidal scheme is deemed sufficient in this study. As the computational costs related to simulation tracking of the smallest particles are enormous, the analytical scheme is deemed sufficient for $d_p = 1$ and 5nm.

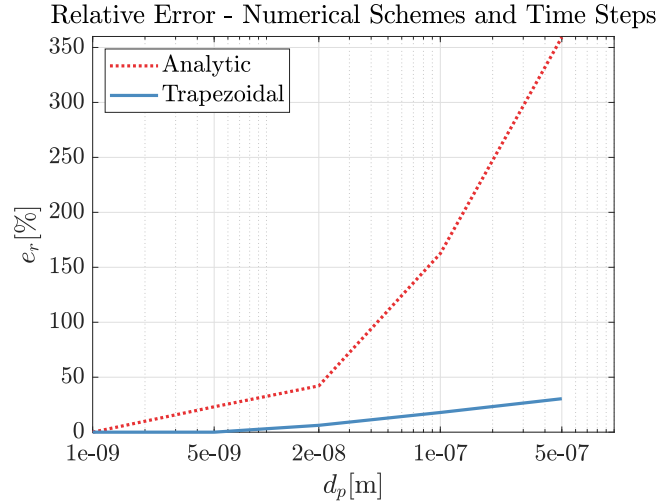


Figure 7.2: The relative error of the analytic and trapezoidal schemes are evaluated based on the trapezoidal scheme with restricted time step of $\Delta t = \tau_p/2$.

7.2.2 Boundary Conditions

The particles are assumed to stick to the wall once they reach the wall, i.e. the effects of particle rebound and resuspension are neglected. This assumption is common in numerical simulations of submicron particles in the literature (Chauhan 2019; Gao et al. 2012; Mofakham and Ahmadi 2020; Tian and Ahmadi 2007). Tandberg (2017) investigates rebound effects of particles on the wall, and by employing $Re = 6,000$ channel flow with $u_\tau = 0.35\text{m/s}$, it is concluded that particles with $d_p < 20\ \mu\text{m}$ will remain deposited once attached to the wall. Hence, this assumption is deemed applicable to the range of particle sizes evaluated in the present study.

The UDF `DEFINE_DPM_BC` from Tandberg was used at the wall in the test section, enabling visualisation of the deposited particles along the wall in MATLAB. In addition, constant deposition of particles along the walls can be ensured in MATLAB, validating the assumption of a fully developed particle profile. The deposition velocity is calculated based on the number of particles transported into the test section and the number of deposited particles in the test section of the channel (from 150 mm to 200 mm). As the particles are simulated as mass points in DPM, the `DEFINE_DPM_BC` is not called before the mass point is at the wall. Therefore, to exclude a possible bias, the new model in the UDF `DEFINE_DPM_DRAG` assumes a particle to stick if its mass point is located closer than the particle radius, $d_p/2$, to the wall. This is a more realistic deposition boundary condition, and the default model in Fluent (a) and the implemented model (b) are illustrated in Figure 7.3.

At the outlet, a similar UDF is employed, where the position of where particles leave the domain is marked. Based on this data, a particle concentration profile can be constructed and validated.

7.2.3 Surface Roughness

The roughness of the pipe employed in the experimental study (see Chapter 8) is $k = 1.5\ \mu\text{m}$, resulting in $k^+ = 0.7$ for the three conditions considered and within the valid limit of slightly rough walls for expression Equation 5.35. In addition, this low pipe roughness makes the roughness model of Fan and Ahmadi (1993) applicable. By modifying the boundary condition presented in Figure 7.3 (b), the roughness model presented in Section 5.2.4 can be implemented and tested. This boundary model is illustrated in Figure 7.3 (c).

7.2.4 Particles

The rate of which particles are deposited on a surface in a fluid flow is closely related to the particle sizes. The particles sizes focused in this study is based on the hitherto unpublished generation and agglomeration model of Bordvik, Næss et al. (2021), which shows that geothermal process equipment

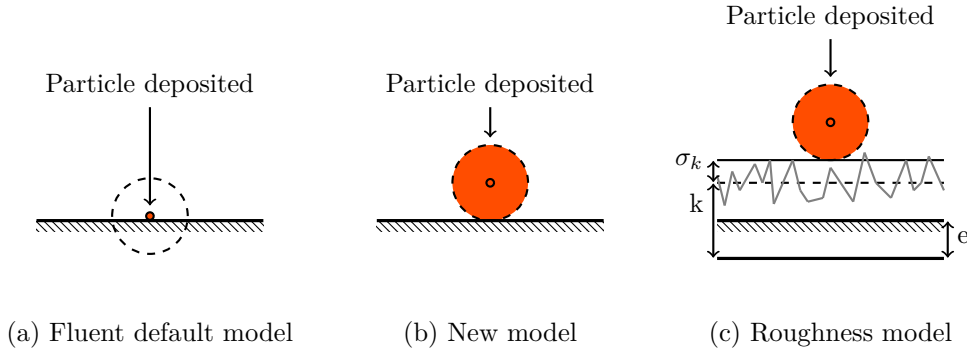


Figure 7.3: The default model in Fluent (a) takes a particle to be deposited when its mass point reaches the wall, whereas the new model (b) takes a particle to be deposited when the particle touches the wall, i.e. it is located $d_p/2$ from the wall. The roughness model (c), shifts the origin of the mean velocity by e and takes a particle to be deposited when it is located $\sigma_k + k - e + d_p/2$ from the wall (see expression (5.42)).

are prone to deposition of submicron particles sizes down to $\mathcal{O}(1 \text{ nm})$. For simplicity, coagulation and agglomeration of the particles are neglected, i.e. mechanisms including particle collisions and results of it. The particles were set to have the properties of silica, as presented in Table 7.1. The particle diameters ranged between 1 nm and 500 nm.

The Knudsen numbers, Kn , and the particle relaxation times, τ_p for the different particle sizes evaluated are presented in Figure 7.4.

Table 7.1: Properties of silica used in the simulations. The data are collected from Bergman et al. (2011).

Properties	Values
ρ_p	2160 kg/m ³
$k_{th,p}$	1.5 W/mK
$c_{p,p}$	44 J/kg · K

7.2.5 Particle Forces Implementation

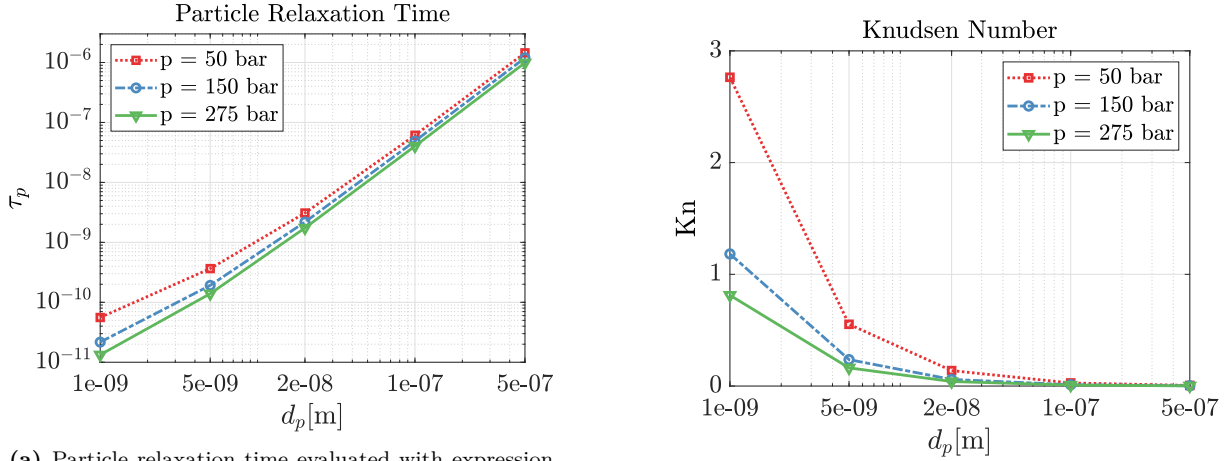
The general carrier effects and the deposition mechanisms on particles in a turbulent flow were introduced in the Chapter 5. The implemented models are presented below.

Brownian Forces

In Fluent, the implementation of the Brownian motion is only intended for laminar simulations, i.e. for particles that obey the Stokes-Cunningham drag law ($Re_p \ll 1$). In order to include a drag law for particles with $Re_p \gg 1$, an UDF for the Brownian motion is implemented in `DEFINE_DPM_BODY_FORCE` and is taken from the project work of Stordal (2020). The implemented model is presented in Section 5.1.4.

Drag Forces

Both expressions (5.6) and (5.7) for the drag coefficient are employed in the particle model, demarcated by the particle Reynolds number. As the expression of Schiller and Nauman (1933) is valid for $Re_p > 1$ and the Stokes drag formulation is satisfactory up to $Re_p < 0.7$ (Crowe 2006), the limit of Stokes drag is set to $Re_p = 1$. The combination of these drag force expressions is not default in Fluent and the formulations are implemented in the UDF `DEFINE_DPM_DRAG` (see Code listing B.1).



(a) Particle relaxation time evaluated with expression (5.29) at different conditions for the evaluated particle sizes.

(b) Knudsen number evaluated with expression (5.8) at different conditions for the evaluated particle sizes.

Figure 7.4: Particle variables at different superheated vapor condition (see Section 5.2.1).

Lift Forces

The Li and Ahmadi (1992) generalisation of the Saffman lift force as introduced in expression (5.13), is a built-in functionality in ANSYS Fluent. This model is valid as $\sqrt{Re_\tau} \approx 25 \gg Re_p$ for the superheated steam cases, and is employed in the predictions, although the effects are assumed to be negligible for submicron particles Stordal (2020).

Thermophoresis

The Talbot formulation for the thermophoretic coefficient, which is default in ANSYS Fluent, is employed for the thermophoresis simulations. Simulations with a temperature difference of 10 K were performed. This corresponds to a temperature gradient at the wall of 3891 K/cm using Equation 5.41, and a total temperature gradient of 145 K/cm. Simulations were performed with high resolution tracking in order to include interpolation of the thermal gradient, giving rise to better estimates of the thermophoretic force. In that case, no significant changes in the deposition velocity were observed.

7.3 Discrete Random Walk - Turbulent Dispersion of Particles

In this section, the performance of the two DRW models introduced in Section 5.1.5 are compared, verified and validated with theory. Their relative influence on the particle concentration profiles at the outlet and deposition on the wall are compared and validated with literature. These models are from here named the SI-DRW, or the improved-DRW by Stordal, and the SC-DRW, or the conventional-DRW by Stordal. In addition, the comparison are performed in a reproduced case, using the conditions of Mofakham and Ahmadi (2020) in order to verify the code (hereby Ahmadi-channel). The respective model results from Mofakham and Ahmadi (2020) are named the MI-DRW (the improved-DRW) and the MC-DRW (the conventional-DRW)

7.3.1 Implementation

In Figure 7.5, a simplified flow chart of the particle tracking in ANSYS Fluent Discrete Phase Model (DPM) is illustrated. The red boxes in the chart represent the implemented SI-DRW model. The purple boxes represent the DPM particle tracking. SI-DRW and SC-DRW differ in (I) in Figure 7.5, where τ_e and u_i' are generated and updated.

The conventional-DRW model (the SC-DRW model), which is default in Fluent, can easily be implemented in the DPM model. The SI-DRW is implemented with several UDFs, by making modifications

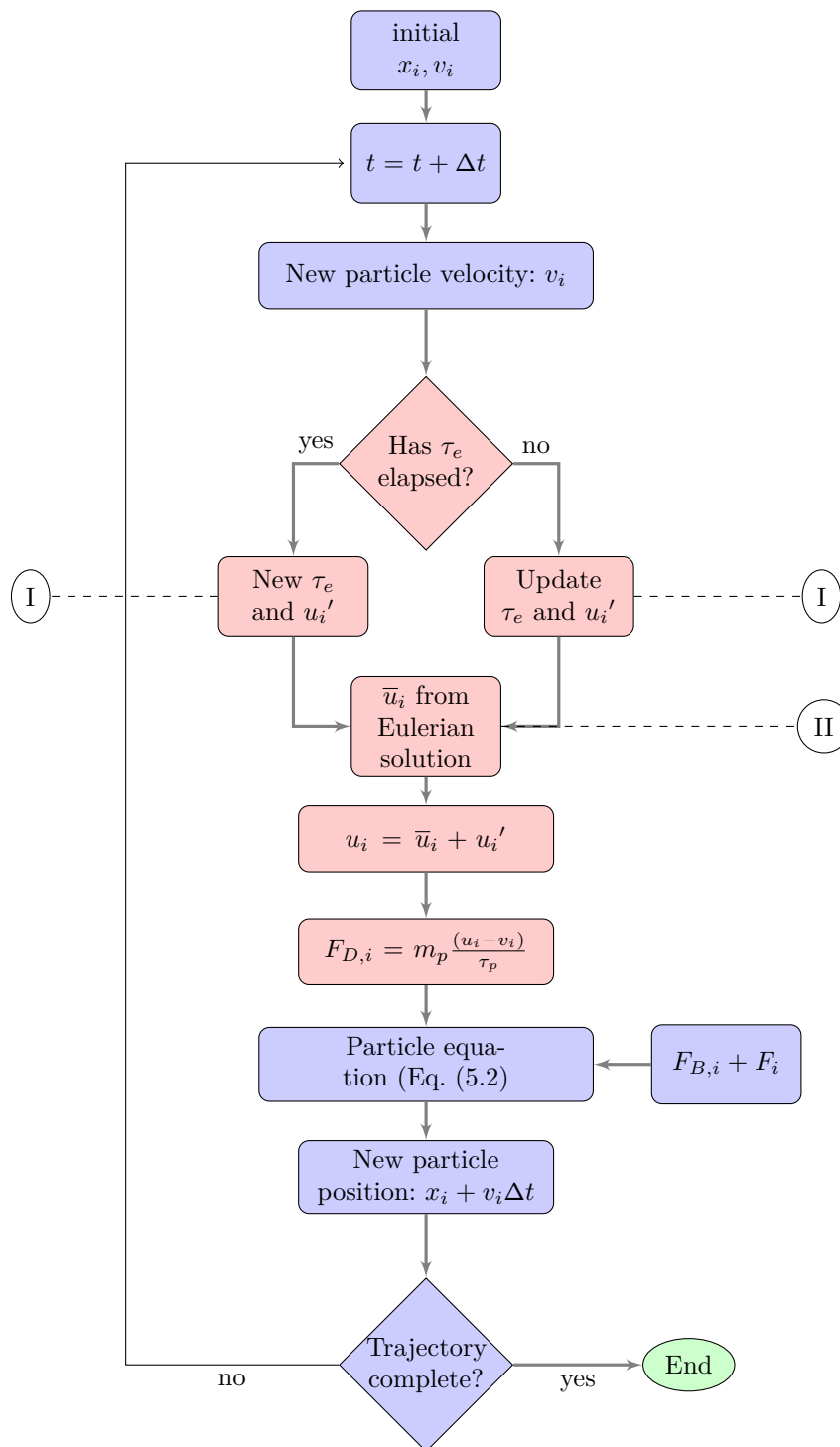


Figure 7.5: Particle tracking in ANSYS Fluent. The red blocks represent the DRW-model implementation.

on the conventional-DRW model implemented as UDFs by Longmire (2007). Using this method, an instantaneous turbulent fluctuating velocity is generated in the particle cell location and therefore induce a drag force on the particle, as the relative velocity changes (see Equation 5.3). This is implemented with the `DEFINE_DPM_DRAG` UDF. The code can be found in the Appendix: Code listing B.1. In the code, only the essential wall-normal direction of Equation 5.27 is evaluated for correction. As no spurious drift is associated with the stream-wise and span-wise direction, the conventional discrete random walk is employed in these directions.

Mofakham and Ahmadi (2020) have not elaborated their method to evaluated the gradients in the correction terms in Equation 5.27. Flow gradients are often accessible Fluent macros for UDFs, but the gradients for the mean turbulent fluctuating velocities are not optional (Fluent 2021a). Therefore the gradients are evaluated based on the DNS data of the Lagrangian integral time scale (Equation 5.28) and the wall-normal turbulence velocity component (Equation 4.20). The derivatives are found by

$$\frac{d\gamma_2}{dx_2} = \frac{d(\gamma_2/u_\tau)}{d(yu_\tau/\nu)} \frac{u_\tau^2}{\nu} = \frac{d\gamma_2^+}{dy^+} \frac{u_\tau^2}{\nu}; \quad (7.1)$$

$$\frac{dT_L}{dx_2} = \frac{d(T_L/u_\tau)}{d(yu_\tau/\nu)} \frac{1}{u_\tau} = \frac{dT_L^+}{dy^+} \frac{1}{u_\tau}. \quad (7.2)$$

Based on the wall-normal particle location, the correction term is updated for every time step, so is γ_i in expression (5.20).

7.3.2 Lagrangian Eddy-Time Scale

Good estimates of the fluid-particle interaction time is important, but difficult to measure in in-homogeneous flows. In Fluent (2021b), the Lagrangian integral time scale, T_L , is a function of the turbulent kinetic energy, k , and the turbulent dissipation rate, ε , which is consistent with the literature. With this method, the fluid simulation results are the basis for T_L . For the case of $Re = 10,000$, the Lagrangian eddy-time scale in Equation 5.22 is evaluated over the particle half-channel for $C_L = 0.3$ and $C_L = 0.2$. The results are presented in Figure 7.6. The curve-fitted expression (5.28) of Kallio and Reeks (1989) is based on experimental data of k and ε and includes a variation with the turbulent Reynolds number. The near-wall variation are therefore deemed more physical (see Section 5.1.5).

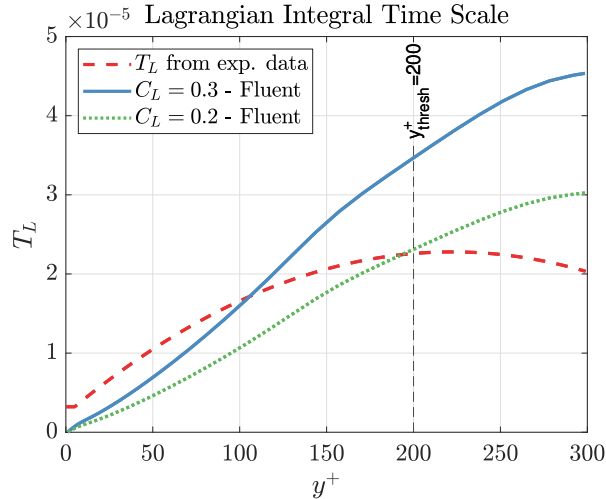


Figure 7.6: The Lagrangian integral time scale, T_L , as a function of y^+ over the half channel width.

There are significant discrepancies between the two approaches in the near-wall region and in the core region of the flow ($y^+ > 200$). The Fluent approach tend to zero in the wall vicinity, whereas the experimental data are constant for $y^+ < 5$. In the project work of Stordal (2020), the simulated deposition velocity deviated with a factor of five within the experimental limits of C_L . Therefore, the choice of model approach will influence the simulation results. Measurements in the present study showed

that the curve-fitted expression from Kallio and Reeks (1989) produces simulation results more similar to experimental and numerical results from the literature.

For the SI-DRW, the curve-fitted expression (5.28) is therefore utilised if the particles are closer than the threshold $y^+ < 200$ from the wall. Elsewhere, the Fluent expression with $C_L = 0.2$ is used to avoid discontinuity. In the SC-DRW, C_L is set to 0.3, as recommended by Fluent (2021b).

Note that the eddy time in expression (5.21) is proportional to the Lagrangian integral time scale, and is updated for every time step. Therefore, as a particle is transported towards the wall, the total eddy time is reduced as T_L decreases. Higher dissipation near the wall reduces the energy in the turbulent eddies faster, hence the lifetime of the eddy mitigates.

7.3.3 Concentration Profiles

The Stokes number (see Equation 5.32) relates to the response time of the particle velocity to fluid velocity changes. The particle relaxation time, τ_p , for the submicron particles in the current study is very small. Henceforth, $Stk \ll 1$ for all the examined particles. The particles will then behave like fluid tracers and follow the streamlines. In this case, mass transfer relations govern particle motion, in other words turbulent and molecular (Brownian motion) diffusion. Due to the random nature of turbulence, the particles should be randomly distributed in a fully turbulent flow, meaning that a dimensionless concentration profile should be around unity over the channel width. However, the particle concentration at the wall is zero and the Brownian motion is dominant in the near-wall region, resulting in a concentration gradient for these small particles (Mofakham, Ahmadi and J. McLaughlin 2018), e.g. $d_p = 10$ nm.

For bigger particles, inertia effects should be taken into account, the Brownian motion becomes of less significance and the turbulent mixing is dominant closer to the wall. Therefore, increasingly higher particle concentrations near the wall are expected for bigger particles, e.g. $d_p = 1$ μm .

In the figures below, the different predictions of the normalised concentration profiles are presented.

- The improved and conventional models of Mofakham and Ahmadi (2020), MC-DRW (red, dotted) and MI-DRW (black), are presented in Figure 7.7
- The improved and conventional models performed here, SC-DRW (red, dotted) and SI-DRW (black) are presented in Figure 7.8

In Figure 7.7, the concentration profiles from the in-house MATLAB particle tracking code by Mofakham and Ahmadi (2020) with MI-DRW and MC-DRW are presented for the 10 nm and 1 μm particle sizes. Here it is evident that MI-DRW predicts concentration profiles according to the theoretical descriptions of mass transfer. In contrast, the MC-DRW produces an spurious accumulation of particles in the near-wall region.

By reconstructing the geometry, fluid and particle conditions from Mofakham and Ahmadi (2020), the PARTICLE model can be verified. Note that the mesh employed in this study has $y^+ \approx 1$, whereas Mofakham and Ahmadi (2020) used $y^+ < 0.1$ with the $v^2 - f$ turbulence model. In Figure 7.8, the normalised concentration profile results from the SI-DRW and SC-DRW are presented in a similar manner. In addition, the normalised concentration over the half channel width is also illustrated here. In all the figures, the red dotted line represents the conventional-DRW and the black solid line represents the improved-DRW. The normalised concentration is defined as

$$\tilde{c} = \frac{c/h_{cell}}{\bar{c}}, \quad (7.3)$$

where c is the local concentration of particles at the outlet, h_{cell} is the wall-normal height of the cell and \bar{c} is the mean concentration over the channel height.

Firstly, the SI-DRW predicted with the PARTICLE model are quite similar to the MI-DRW for small y^+ . The main discrepancy between the code implementations is at $y^+ > 100$, where more consistent concentration profiles closer to unity are produced by the MI-DRW model.

Indeed, the MI-DRW and the SI-DRW models produce the same trends in the concentration profiles. The SI-DRW in the PARTICLE model clearly results in concentration profiles more similar to the theoretical behaviour of submicron particles, in contrast to the SC-DRW. However, some discrepancies are observed for $y^+ > 30$. Compared to the theory and Figure 7.7, the SI-DRW overestimates the concentration $y^+ > 30$ and underestimates the concentration closer to the core region $y^+ > 80$. This is possibly

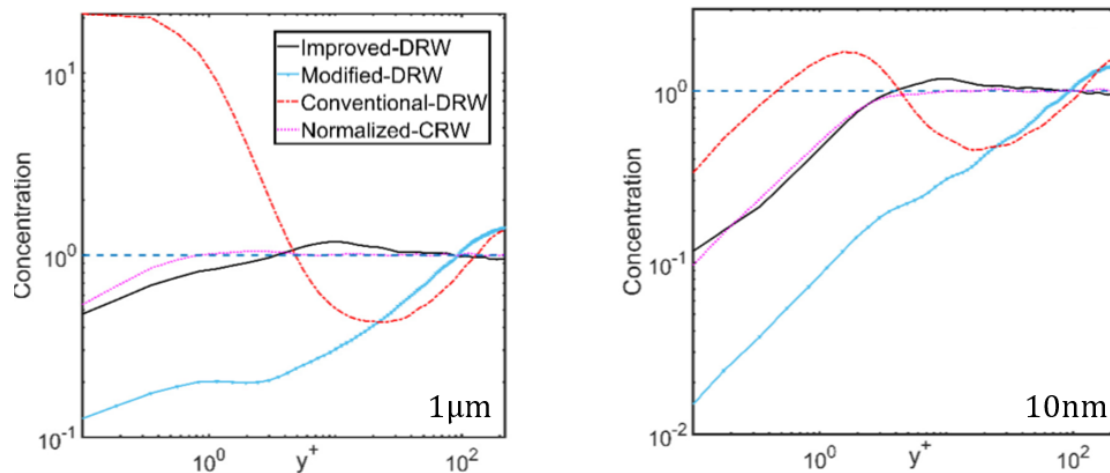


Figure 7.7: The particle concentration profiles of finite-sized particles of $1\ \mu\text{m}$ (left) and $10\ \text{nm}$ (right) produced by the different random walk models found in Mofakham and Ahmadi (2019). In the current study, the conventional-DRW (red, dotted) and improved-DRW (black) are compared. The figure is taken from Mofakham and Ahmadi (2019).

related to a systematic difference between the implementations, as a similar discrepancy is observed between the SC-DRW and SI-DRW.

7.3.4 Inclusion of a Boundary Layer Model

In addition to making modifications to the DRW model, the PARTICLE model include a boundary layer model. The RSM model do not produce the desired wall-normal fluctuating velocity in the vicinity of the wall, as presented in Figure 9.1b. The effect of the wall-normal fluctuating velocity on the deposition velocity is widely reported in the literature (Gao et al. 2012; Ounis, Ahmadi and J. B. McLaughlin 1993; Tian and Ahmadi 2007). Therefore, correction to this crucial component is implemented in the improved-DRW model.

High resolution tracking of the particles refines the particle tracking with interpolation methods, but requires additional computational time in the simulations. When utilised, interpolation of flow properties are performed based on particle location from the cell centres. However, if not utilised, cell centre values of flow properties, e.g. v' , are the input to the DPM ((II) in Figure 7.5) irrespective of the particle location in the cell. This could especially have an enhanced effect near the wall, where the gradients are significant. Therefore, a continuous expression of the crucial wall-normal fluctuating velocity near the wall would be effective, meaning a boundary layer model. There are two advantages with this boundary layer model:

- The unphysical enhancement of particle deposition related to overestimation of v' near the wall is extinguished.
- The increased accuracy related to high resolution tracking and heavy interpolation of flow properties is made less significant and avoidable.

Li and Ahmadi (1992) recommend the expression (4.19) for particles within $y^+ < 4$. Dehbi (2008) employed expression (4.20) as a boundary layer model in simulations of micron-sized particles. The boundary layer model also included curve-fitted DNS data for dissipation and the streamwise and spanwise mean fluctuating velocity components. Therefore, the input to the improved-DRW ((II) in Figure 7.5) inside the boundary layer is from the curve-fitted DNS-data and not from the $k-\omega$ SST fluid solution employed by Dehbi (2008). In that way, Dehbi (2008) could account for turbulence anisotropy near the wall, even though the turbulence model assume the turbulence to be isotropic. These two boundary layer models are implemented into the PARTICLE model and compared in Section 7.3.5.

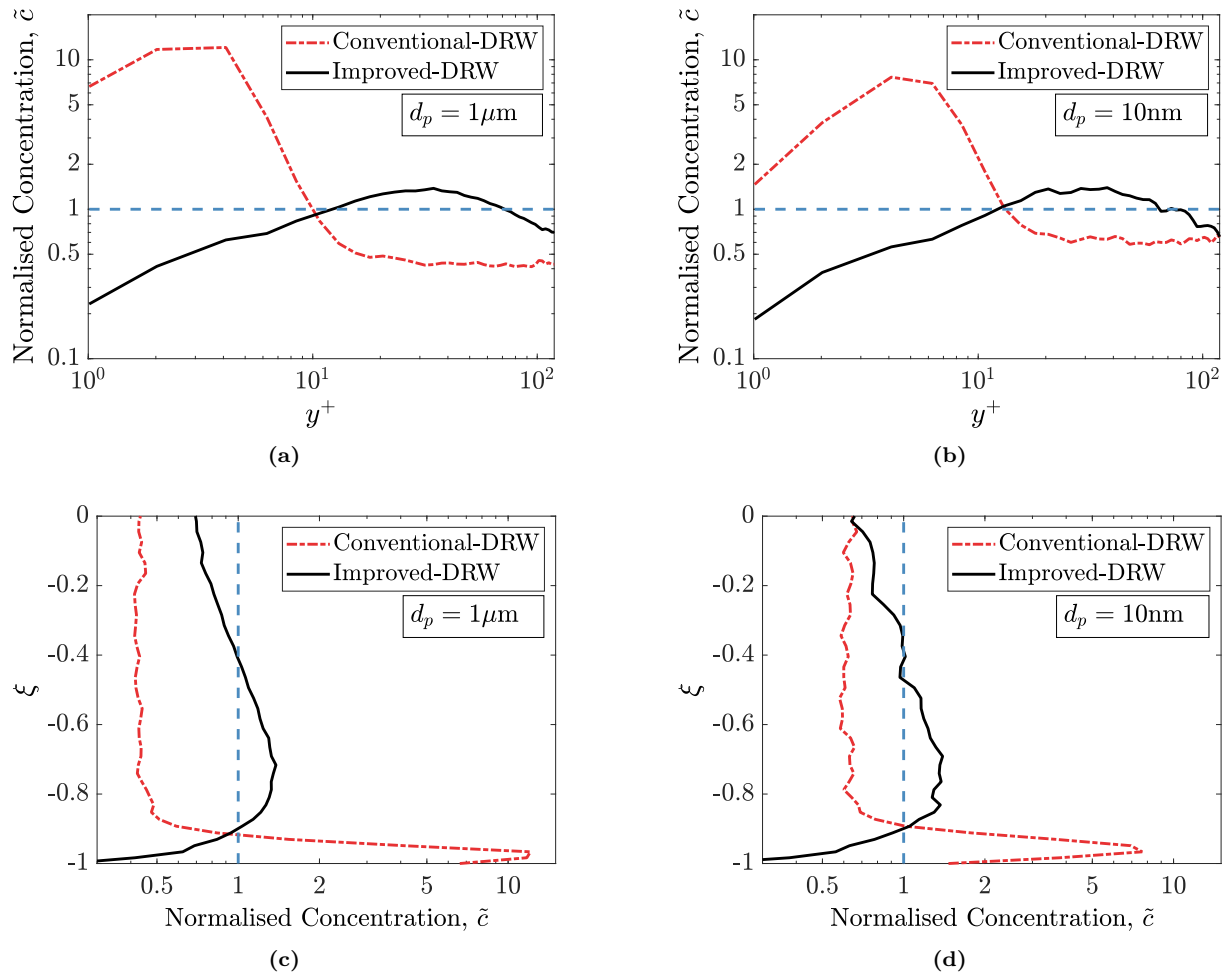


Figure 7.8: Concentration profiles at outlet over the channel width for the SC-DRW (red, dotted)- and SI-DRW (black) models (below). Concentration profiles at outlet at different y^+ for the SC-DRW (red, dotted)- and SI-DRW (black) models (upper).

7.3.5 Deposition Velocity

The dimensionless deposition velocity, V_d^+ , in Figure 7.9 is plotted versus the dimensionless relaxation time, τ_p^+ . Predictions for 10nm to 1 μ m particles are performed with SI-DRW and SC-DRW in the Ahmadi-channel. Here, the near wall correction of Li and Ahmadi (1992) were employed, in addition to Brownian motion. The results of Mofakham and Ahmadi (2020) (MC-DRW and MI-DRW) are included for comparison, as well as curve-fitted data of experimental data from Papavergos and Hedley (1984), earlier numerical results of Fan and Ahmadi (1993) and the Colburn heat transfer analogy.

From the figure, we observe that the SC-DRW and the MC-DRW behave very differently for the 10nm and 1 μ m particles. This might be related to the different near-wall concentration profiles. However, this was not further investigated. Figure 7.9 shows that the SI-DRW predictions are in agreement with the experimental and numerical predictions. In general, it gives very good predictions of the deposition velocity and better predictions than the SC-DRW. The SI-DRW is therefore chosen in the present study and implemented into the PARTICLE model.

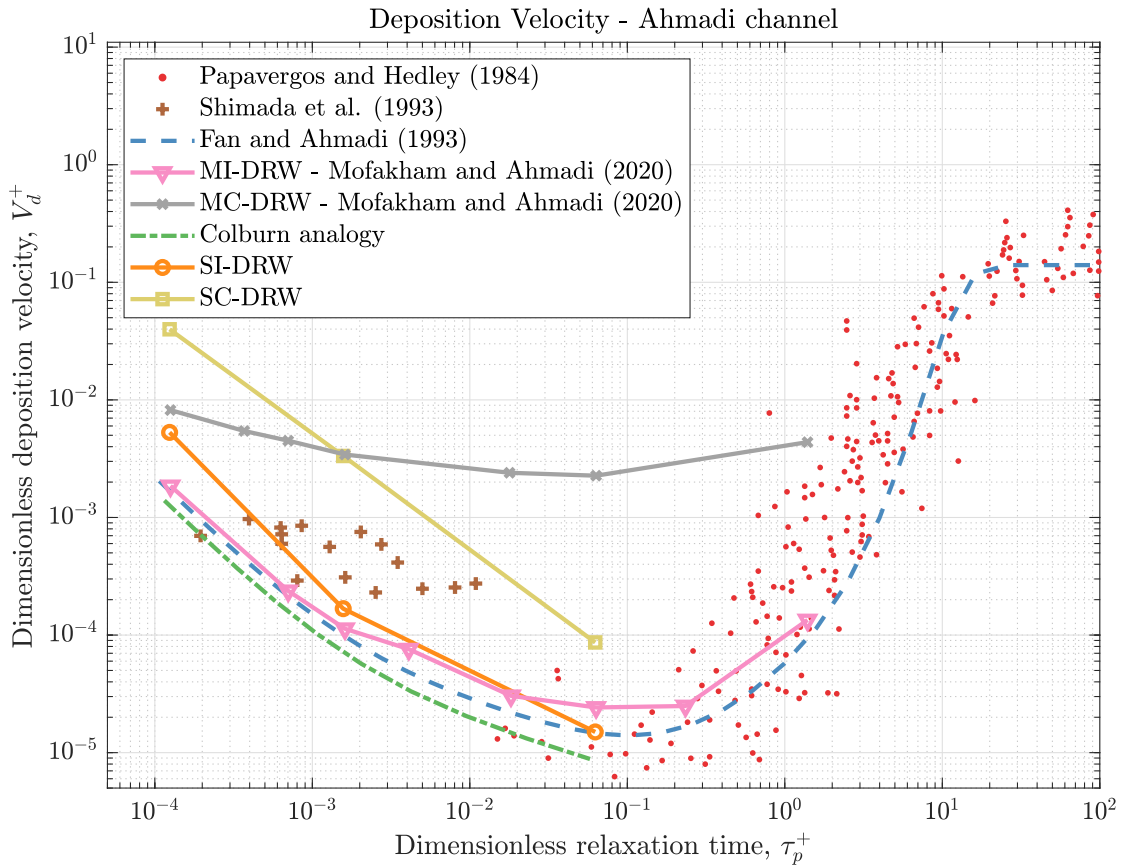


Figure 7.9: Comparison of the dimensionless deposition velocity predictions by different DRW-models with experimental, earlier numerical results and a heat transfer analogy.

Boundary Layer Model in the Ahmadi-channel

In Figure 7.10 the effects on the deposition velocity for the two boundary layer models are presented versus the particle relaxation time. Empirical, numerical and experimental results are included to assess the accuracy, similar to Figure 7.9. Simulations with the PARTICLE model were performed for no boundary layer model (grey), boundary layer model with Equation 4.19 (yellow) and boundary layer model with Equation 4.20 (orange).

The effect of including Equation 4.19 for $y^+ < 4$ is significant compared to employing no boundary layer model for the wall-normal fluctuating velocity. When the wall-normal fluctuating component is not

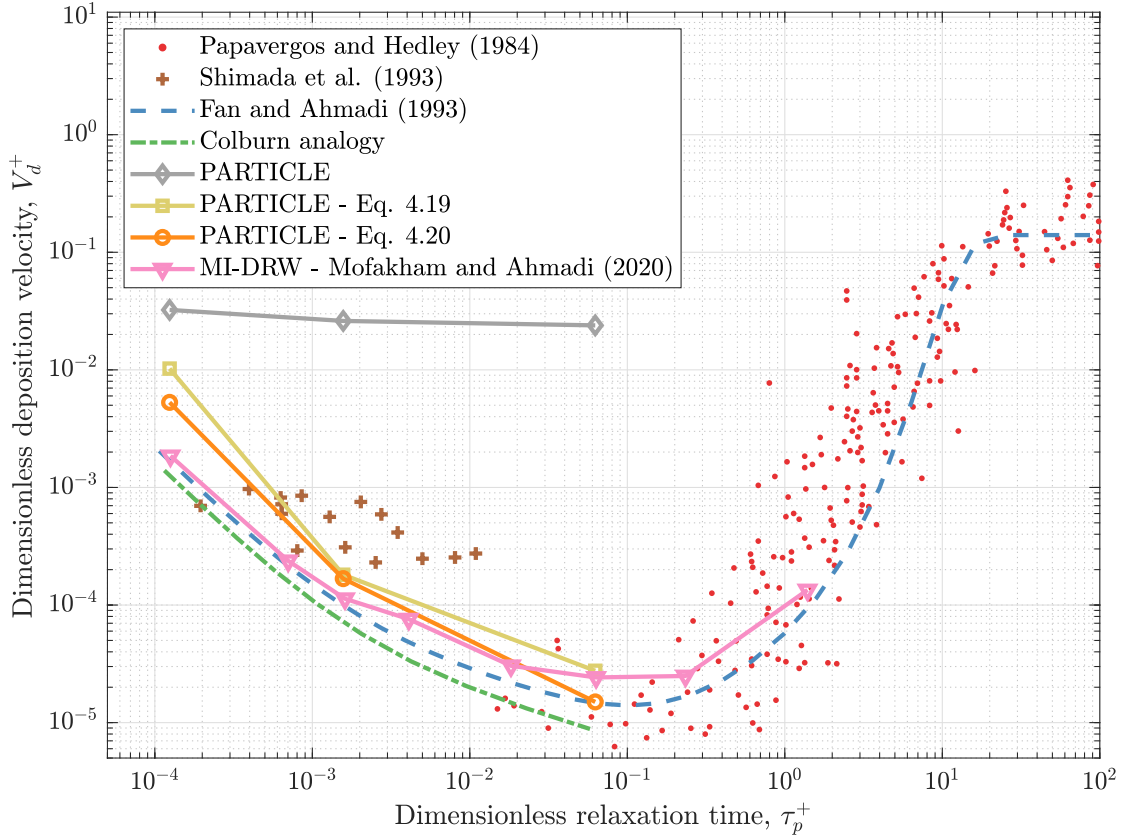


Figure 7.10: The dimensionless deposition velocity versus the dimensionless particle relaxation time for $p = 50$ bar compared to the numerical correlation of Fan and Ahmadi (1993), the experimental correlation of Papavergos and Hedley (1984) and the Colburn analogy to heat transfer. The simulation results are based on different boundary layer models for the wall-normal fluctuating velocity; No model, Equation 4.20 and Equation 4.19

corrected near the wall, high discrepancies from the empirical correlations are observed. The dimensionless deposition velocity is correctly reduced by several orders of a magnitude when the boundary layer model by Ounis, Ahmadi and J. B. McLaughlin (1993) is employed. Further mitigation on the deposition velocity is introduced when Equation 4.20 is employed in the boundary layer model.

The results presented in Figure 7.10 illustrate the significant influence of the near wall v' prediction on the simulation results. However, it also elucidate the sensitivity in the PARTICLE model. Compared to the SC-DRW presented in Figure 7.9, the deposition results are poor when excluding the boundary layer model. Hence, it seems like the near-wall overestimation of v' might lead to enhanced deposition with the SI-DRW. Term (b) in the drift term introduced in the improved-DRW (see Equation 5.27) enforces particles towards the wall, to reduce the effects of time-scale inhomogeneities. As this term is proportional to the square of v' , deposition enhancement might occur if the wall-normal fluctuating velocity is overestimated. Furthermore, high resolution tracking and interpolation of v' were not employed near the wall, which might have led to further enhancement.

The deposition velocity predictions are further improved when Equation 4.20 is employed in the boundary layer model. However, these reductions are of less significance. This indicates that correction to v' in the viscous sublayer ($y^+ < 5$) is pivotal for deposition modelling of submicron particles. However, in the PARTICLE model, the boundary layer correction of Equation 4.20 is implemented.

8 | Experimental Investigation

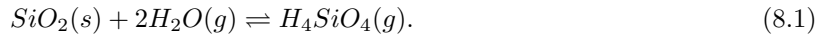
The numerical simulations in ANSYS Fluent of submicron silica particle deposition in superheated and supercritical water vapour need to be validated with experimental data. Currently, no experiments of this kind have been found in the literature. Chauhan (2019) performed experiments of silica particle deposition and concentration in superheated steam with injected particles ranging from 1 μm to 20 μm in size. These straight pipe experiments were performed at 1.4 bar and 160 $^{\circ}\text{C}$.

The purpose of the experiments is to accurately measure the mass of deposition in three different places in the experimental rig. The measured deposition represents the deposition caused by silica particles formed when depressurising steam from 350 bar and 500 $^{\circ}\text{C}$ through an isenthalpic valve to pressure and temperature ranging from 50 bar to 275 bar and 325 $^{\circ}\text{C}$ to 500 $^{\circ}\text{C}$. The experiments were conducted at the Institute of Energy Technology (IFE).

Below, some theoretical background, the aims and objectives of the experiment, the experimental setup, the construction of the rig and the performed experiments are described. Lastly, the calculation procedure and uncertainty analysis are presented. The results are presented in Section 9.3.

8.1 Theoretical Background

At reservoir conditions, the temperature in the superheated water vapour is above 185 $^{\circ}\text{C}$. The silica content can then be determined from the equilibrium value of quartz in the superheated water vapour. Hence, the dissolution of silica in the geothermal reservoir and precipitation (generation) of silica over pressure drops follow the simplified reaction rate



Here, H_4SiO_4 is silicic acid. The crystalline forms of $\text{SiO}_2(s)$, like quartz and cristoballite, have relatively slow reaction rates and are not common in geothermal systems. On the other hand, amorphous silica is a non-crystalline form of silica and has a fast enough reaction time to cause precipitation (Bordvik and Næss 2020).

The driving force for silica precipitation is rapid changes in the supersaturation of silicic acid. The rate of supersaturation is measured by the supersaturation index (SSI):

$$SSI = \frac{\text{actual concentration}}{\text{equilibrium concentration}}.$$

High values of the SSI are expected in superheated geothermal steam when the density is drastically reduced (Fournier and Potter II 1982a), for instance, over pressure drops in the process plants. When this happens, the dominant mechanism involved in the formation of silica precipitate is bulk polymerisation and the formation of nanocolloids, i.e. nano-sized particles. Bulk polymerisation happens as monomers mutually condensate and bond, giving rise to so-called nuclei, or nanocolloids. This mechanism is called homogeneous nucleation and is often associated with high deposition rates (Bordvik and Næss 2020; Brown 2011).

In Figure 8.1, precipitation as homogeneous nucleation, agglomeration and deposition are illustrated. Here, high pressure is illustrated in red and lower pressure in blue. Over the orifice in (ii), large amounts of nuclei and monomers are precipitated into the flow. The number of particles and the initial particle sizes is dependent on the SSI. After this initial reaction, the system will move towards equilibrium ((iii)

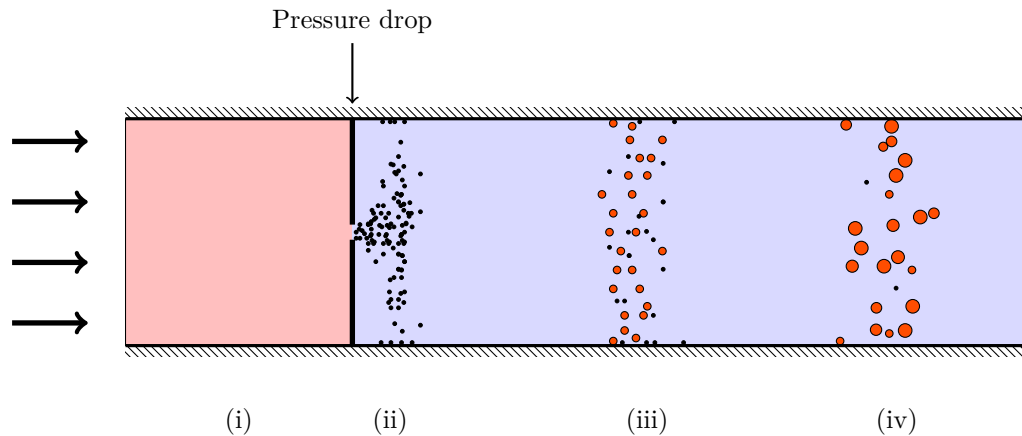


Figure 8.1: Illustration of particle precipitation, agglomeration and deposition: (i) high pressure zone; (ii) pressure drop and $SSI \gg 1$ leading to precipitation of particles; (iii) Agglomeration and system moves towards equilibrium; (iv) Particles grow bigger and system is in quasi-equilibrium. The particle size and the geometry is not to scale.

in Figure 8.1). Then, three mechanisms arise: The monomers will either (1) attach to the nanocolloids (larger particles) or (2) redissolve in the superheated water vapour. New nuclei are less likely to emerge, as the energy required to form a nucleus is higher than latch on an already formed particle. The last mechanism (3) is agglomeration, where nanocolloids merge to form larger particles. As the system strives towards equilibrium, the larger particles will grow larger, as seen in (iv) in Figure 8.1.

The agglomeration is determined by the particle transport mechanism and particle-particle interaction forces. Particles of nucleus size (1 nm) ((ii), (iii) in Figure 8.1) is dominated by Brownian motion, and the growth is relatively slow. As the particles grow in size and the influence of turbulence becomes significant ((iv) in Figure 8.1), the particle growth due to agglomeration is accelerated exponentially (Lewis et al. 2015). However, agglomeration is also highly dependent on the particle-particle interaction forces, which affect the collision efficiency. Many factors are influencing the interaction forces, e.g. particle surface charge, ionic strength of water, pH, silica-water surface tension, concentration, and flow characteristics (Bordvik and Næss 2020).

From the initial precipitation of particles with homogeneous nucleation, particle deposition is present. The transport and deposition mechanisms of submicron particles are presented in Chapter 5. From the literature, deposition velocity decreases for increasing particle sizes in the diffusion-dominated regime. Therefore, high deposition rates are expected in the vicinity of pressure drops, as the finest particles are present here. The deposition layer can also consist of nuclei precipitated on the wall, forming hard scale layers by condensation on the wall. This type of precipitation is called heterogeneous nucleation.

8.2 Aims and Objectives

The experimental investigation aims to validate calculated rates of precipitation, agglomeration and deposition by quantifying deposition in different test sections downstream a pressure drop, as these three processes are related. The generation of particles at different supersaturation (SSI) rates is measured with deposition in the two test sections. However, the agglomeration is more challenging to measure. Presumably, the measured deposition is higher in the first test section. Such results would indicate that the particle size distribution has shifted towards bigger particles (as the deposition rate reduces for bigger particles) or that the total concentration is reduced (due to deposition) during the transport to test section two. Indeed, in addition to agglomeration, generation of new particles and deposition of particles are present processes between the two test sections. Therefore, model validation is essential to estimate the agglomeration rate.

8.3 Experimental Setup

A schematic diagram of the experimental setup is shown in Figure 8.2. The rig, as set up at IFE, is depicted in Figure 8.4. More pictures and a 3D model of the experimental setup can be found in Appendix A. The setup consists of an autoclave, which generates water vapour at 350 bar and 500 °C with dissolved silica, a heated box, where pressure is regulated, and submicron silica particles are generated, agglomerated and deposited in the test sections. At the rig outlet, the water vapour is cooled to liquid phase. The setup is described in more detail below.

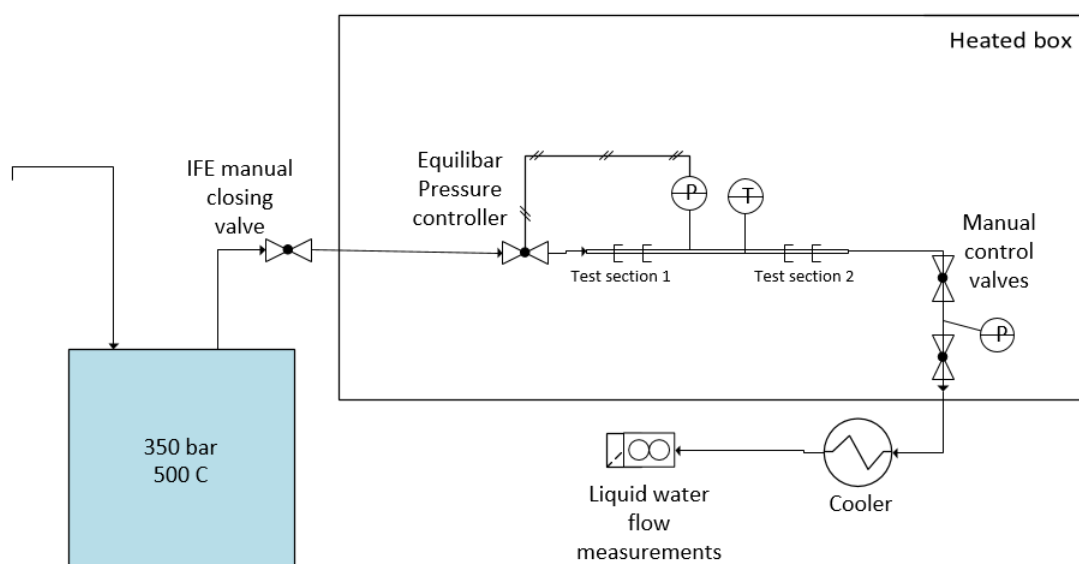


Figure 8.2: Schematic diagram of the experimental setup. The blue box represents the autoclave.

The autoclave is constantly fed by 10 g/min of water during the experiments. Silica particles of 21 μm size are inserted in the autoclave before the initial heating, assuring equilibrium conditions of silicic acid in the water vapour (see Equation 8.1). Then, the water vapour is passed through a metallic filter of 0.5 μm size to ensure that the inserted silica particles in the autoclave are not transported through the test rig. The manual closing valve separates the autoclave from the heated, insulated box and is only opened during the experiments. The primary purpose of the heated box is to avoid temperature gradient biased results. Two heaters with 2 kW capacity each deliver the desired temperature in the heated box.

The pressure controller sets the solicited pressure, the set pressure, in the test sections. The controller consists of a pressure regulator, the Equilibar, and a pressure controller, delivering a reference pressure to the Equilibar. In this setup, the Equilibar is used as a pressure reducing regulator. The Equilibar Ultra High Temperature pressure regulator is rated for 413 bar and 500 °C. Figure 8.3 shows a simple illustration of the functionality of the Equilibar. The technology is dome-loaded, meaning if the upstream process pressure is much less than the reference pressure in the dome, the regulator is closed, and the diaphragm is pushed down. On the other hand, if the reference pressure is lower than the process pressure, excess pressure is relieved through the valve.

The reference pressure is controlled by a so-called High-Pressure Dual Valve Vary-P Controller. The controller is supplied with a high-pressure inert gas (typically nitrogen), which needs to be of higher pressure than the maximum process pressure. The controller consists of an inlet valve, an outlet valve, a pressure sensor and a proportional–integral–derivative (PID) controller. Based on the pressure sensor data from the test section, the PID controls the outlet and inlet valve to deliver the correct reference pressure to the Equilibar (Equilibar 2021; PCS 2021).

The pressure drop through the Equilibar is expected to make the silica precipitate in the water

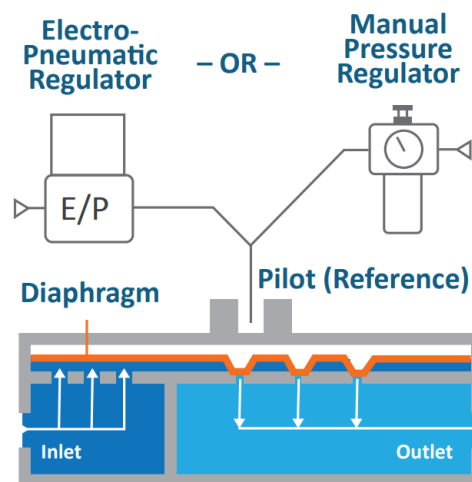


Figure 8.3: Illustration of the functionality of the Equilibar, where the regulator reduces the pressure from the inlet to the outlet based on the reference pressure. The figure is taken from Equilibar (2021).

vapour. Therefore, test section 1 is located just downstream of the Equilibar. A second test section is located 400 mm further downstream to test the agglomeration time of the silica particles along the pipe.

Two manual control valves and a pressure sensor are located at the end of the heated box to control the flow rate through the system manually. After exiting the heated box, the water vapour is cooled in a condenser, where the steam is directed through helix tubing with liquid water circulating on the outside. The condensate is stored for control of the average flow rate.

8.4 Flow Rig Design

An experimental rig was designed and constructed to study the deposition of generated and agglomerated submicron silica particles from depressurised superheated and supercritical steam. The aim was to design a system at controlled hydrodynamic and chemical conditions, which is dynamically similar to the flow conditions in geothermal power plants for deep hot wells, i.e. turbulent flow conditions of high-pressure water vapour. Furthermore, the system was designed with the ability to regulate the pressure in the test sections and the Reynolds number by changing the flow rate.

The autoclave, provided by IFE, has a volume of 21. The autoclave is fed from a constant pressure pump of 250 ml with water at ambient conditions. Due to the restrictive volumes, the maximum flow rate through a stable system is 10 g/min. A small pipe diameter of $D = 1.38$ mm is employed to ensure turbulent flow conditions. For the different fluid flow conditions evaluated, the Reynolds number is in the range 5,000 – 7,300, with respective friction velocities of 0.07 and 0.35 m/s.

Critical equipment, including the Equilibar and the test sections, is located in an insulated box and is heated to test temperature by two electric heaters (see Figure 8.2). By assuming a low Biot number in Equilibar, the temperature is relatively uniform inside it. Therefore, the rig is heated until the temperature sensor located on the surface of the Equilibar reaches the test temperature. In this way, stable thermal conditions are assured inside the rig, and the effect of thermophoresis is minimised. In addition, the equipment located inside the box is covered with a thick layer of thermal insulation.

Lastly, a water-cooled condenser was designed to handle the outlet steam safely. A descriptive picture of the rig is presented in Figure 8.4.

8.5 Experiments - Measurement Procedure

The measurement procedure are described in Appendix A. In the subsections below, the alternative measurements techniques for quantifying the enhanced deposited mass on the test sections are described,

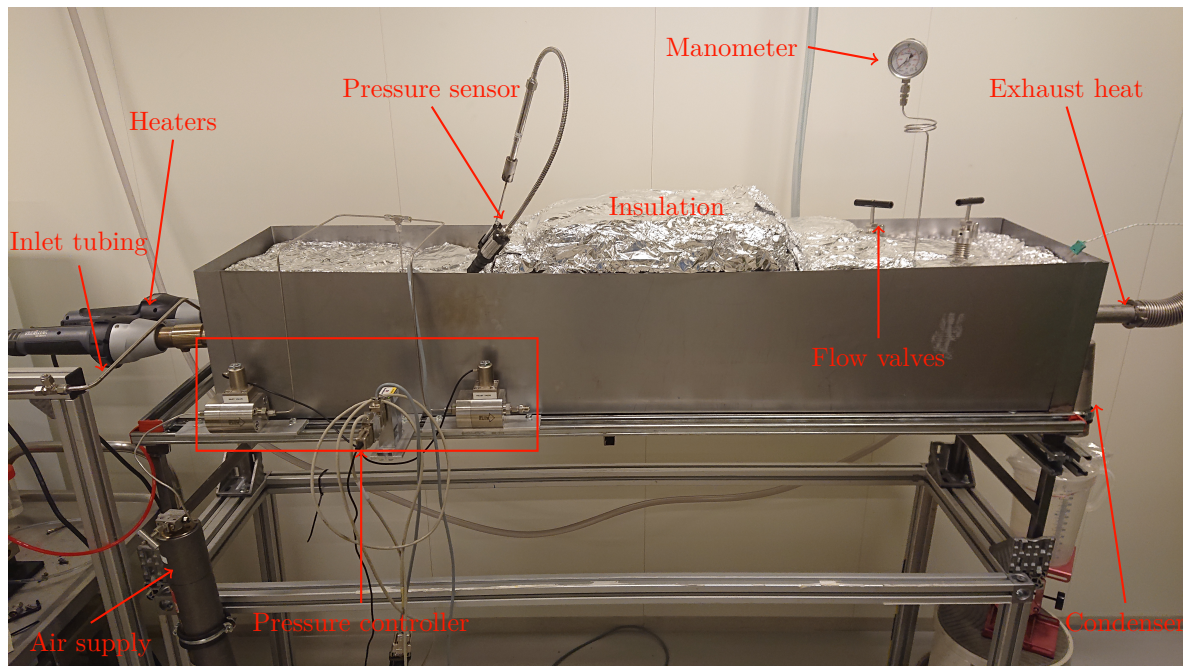


Figure 8.4: Picture of the rig at IFE.

and the experiment matrix is presented.

8.5.1 Measurements Techniques

The deposits accumulated on the pipe surface area during the experiments were initially set to be analysed with mass spectrometry, or ICP-MS measurements, on IFE. Such measurements have higher accuracy than the weighing scale, reducing the uncertainty related to the deposited mass. Unfortunately, the ICP-MS measurements were not carried out due to some technical issues. However, when the experimental investigation starts up again, these measurements are likely to be feasible.

ICP is short for inductively coupled plasma, which is a method for ionising a sample. The samples are introduced as droplets in a gaseous flow, typically of ionised argon gas. They are further inductively heated, atomised and ionised through a high-temperature plasma (typically >3000 K). The ions are then separated based on their mass-to-charge ratio in the mass spectrometer (MS). When the mass spectrometer detects the ions, the concentration of the different species is determined based on the signal intensities of the ions. The accuracy of these concentration measurements can be as low as parts-per-trillion (ppt). In the present experimental investigation, a sample would consist of dissolved silica in distilled water, taken from the Equilibar and the test sections.

8.5.2 Experiment Matrix

The experiments were set to have a mass rate of $\dot{m} = 10$ g/min and to last for five hours (5h). The autoclave water vapour conditions are set to $T = 500$ °C, $p = 350$ bar and with an enthalpy of 3000 kJ/kg. The concentration of silica is then estimated to be 244 mg/kg (Fournier and Potter II 1982b). However, concentration measurements of dissolved silica are performed simultaneously with the present measurements by IFE. In Table 8.1, the test sections conditions are presented for the different experiments. As described later, only preliminary studies are presented in the present study. The performed experiment is presented in bold mode in the table. The numerical results from the model of Bordvik, Næss et al. (2021) on precipitated concentration of amorphous silica and the SSI for the different pressures at test section 1 are also included in Table 8.1 and illustrated in Figure 8.5.

Table 8.1: Experiment matrix with the test section conditions. The performed experiment is presented in bold mode.

T [°C]	p [bar]	Re [-]	SSI	$\bar{c}_{SiO_2,1}$ [mg/kg]
471	275	5,050	1.6	$9 \cdot 10^{-36}$
460	250	5,230	2.2	$1 \cdot 10^{-4}$
448	225	5,410	2.8	19
435	200	5,620	3.8	72
421	175	5,840	5.3	119
406	150	6,080	9.0	168
389	125	6,350	11.3	181
370	100	6,650	15.4	196
349	75	6,970	24.0	213
325	50	7,330	66.2	231

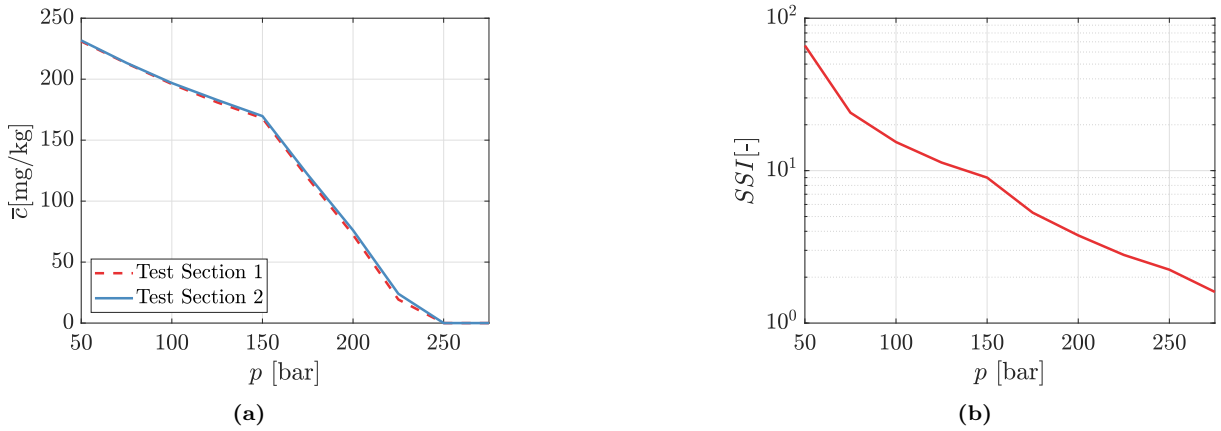


Figure 8.5: (a) The precipitated concentration of amorphous silica in [mg/h] for the two test sections, and (b) the SSI evaluated at different geothermal conditions, according to modelling results from Bordvik, Næss et al. (2021).

8.6 Calculations of the Results

The main results of the experimental investigation are the enhanced masses of the test sections due to particle deposition. Based on measurements at different conditions, the effects of precipitation, agglomeration and deposition can be quantified.

The wall particle flux, J , is calculated based on the enhanced mass of the test section due silica deposits, Δm , the test section area, A , and the duration of the experiment, Δt ; that is,

$$J = \frac{\Delta m}{A \Delta t}. \quad (8.2)$$

The wall particle flux is normalised by accounting for the inlet concentration of silica particles, \bar{c}_{SiO_2} , and the friction velocity, u_τ , and commonly presented as a dimensionless deposition velocity. We arrive at,

$$V_d^+ = \frac{J}{\bar{c}_{SiO_2} u_\tau}. \quad (8.3)$$

Here, the friction velocity is estimated based on volume flow rate measurements and common correlations for the friction factor, C_f . \bar{c}_{SiO_2} is estimated by the precipitation and agglomeration code of Bordvik, Næss et al. (2021). Likewise, numerical estimations of the particle size distributions are necessary, as in-situ size measurements of the deposited particles in the test sections were not applicable. From these estimations, the particle relaxation times, τ_p , (see Equation 5.29) are calculated. The mean particle concentration

and the average particle size are presented in Table 8.2. The particle distribution profiles, experimental results and comparisons with the present numerical model results are presented in Section 9.3.

Table 8.2: Predictions of generation and agglomeration of particles by Bordvik, Næss et al. (2021). The mean concentration, \bar{c}_{SiO_2} , is a measure of the dispersed solid particles in the flow at the inlet of the section.

T	p	Test Section 1		Test Section 2	
		\bar{c}_{SiO_2} [mg/kg]	r_{avg} [nm]	\bar{c}_{SiO_2}	r_{avg}
406 °C	150 bar	168.4	12.8	138.0	16.7

8.6.1 Uncertainty Analysis

If the measured variables x_1, x_2, \dots, x_n are independent of each other and the result R is only dependent of the product of these; that is

$$R = Cx_1^a x_2^b \dots x_n^N, \quad (8.4)$$

The estimated uncertainty, w_R , can then be given as (Wheeler and Ganji 2010)

$$\frac{w_R}{R} = \left[\left(a \frac{w_1}{x_1} \right)^2 + \left(b \frac{w_2}{x_2} \right)^2 + \dots + \left(N \frac{w_n}{x_n} \right)^2 \right]^{1/2}. \quad (8.5)$$

Each of the exponents in Equation 8.4 and coefficient in Equation 8.5 (a, b, \dots, N) can be positive or negative. The result can now be presented as $R = B \pm w_R$, where B is the calculated value of the result. The uncertainties related to the measured variables in the experiments are described in Table 8.3. The estimated uncertainties associated with the experiments are presented in Section 9.3.

Table 8.3: Descriptions of the uncertainties related to the measured variables.

Measured Variable	Description
Duration	Deposition may continue while the rig is cooled, after the experiment is finished
$L_{test\ section}$	Related to measurements of test section length
D_{pipe}	Related to tolerances of manufacturing
Δm	Related to the random uncertainty of the scale
Re	Re is based on volume flow rate measurements, and relates to the friction velocity, u_τ .

In this study, the numerical uncertainties or the uncertainties associated with the theoretical models implemented in the code from Bordvik, Næss et al. (2021) are not considered. The results presented in Table 8.2 for the inlet concentration of precipitated silica particles, \bar{c}_{SiO_2} , and the inlet particle distributions in the test sections are therefore assumed true.

9 | Results and Discussions

This chapter is divided into three sections, namely the flow simulations, the particle model simulations and the experimental investigation. Here, the results are presented and later discussed. In the last section, numerical predictions and experimental results are compared and a calculation procedure is presented.

9.1 Flow Simulation

Three different fluid flow conditions of water vapour are evaluated in this study, and the employed properties are given in Table 6.1. The Reynolds number based on the channel height is set to 10,000 in the three cases, enabling the utilisation of only one mesh. This mesh is verified in the grid independence study in Section 6.7. The shear Reynolds number ($Re_\tau = u_\tau(h/2)/\nu$) is about 305.

9.1.1 Near-Wall Profiles

In Figure 9.1, cross-sectional profiles of mean and turbulent flow variables are presented versus the dimensionless wall distance, y^+ . The profiles are taken from the location of the particle injection ($x_{inj} = 0.05\text{m}$), where the flow is assumed fully developed. The fluid flow results presented in Figure 9.1 are from the $p = 50\text{ bar}$ -conditions, but results for the $p = 150\text{ bar}$ and $p = 275\text{ bar}$ -conditions are similar when made dimensionless.

The streamwise mean velocity profile predicted by the RSM is plotted in Figure 9.1a and is compared with the law-of-the-wall (White 2019) and DNS data of Moser et al. (1999) with $Re_\tau = 395$. The RSM prediction shows good agreement with the DNS data and the empirical correlations of Spalding (1961). The no-slip condition of $u = 0$ is imposed on the first cell, explaining the discrepancy at $y^+ = 1$.

In Figure 9.1e, the normalised turbulent fluctuating velocities are presented and compared to the DNS data by Moser et al. (1999). The results deviate at greater distances from the wall due to the different shear Reynolds number (Re_τ) considered. Thus, the results are illustrated for $y^+ < 100$. In Figure 9.1e, RSM underpredicts the streamwise and spanwise components of the mean turbulent fluctuating velocity for $y^+ < 40$. The more crucial wall-normal component is overpredicted for $y^+ < 15$. This component is presented in more detail in Figure 9.1b. Here, the curve fitted DNS-data from Matida et al. (2000) and DNS-data from Moser et al. (1999) are included, as well as the empirical model suggested by Ounis, Ahmadi and J. B. McLaughlin (1993) (see Equation 4.19). The quadratic variation of v'^+ in the vicinity of the wall, as elaborated in Section 4.2.2, is not captured by the RSM model. In the viscous sublayer ($y^+ < 5$), the overprediction is of a factor of between two and five compared to the curvefitted DNS-data of Matida et al. (2000).

When thermophoresis is taken into account, a temperature gradient is imposed on the fluid flow with a constant heat rate on the walls. The RSM-prediction of a 10 K temperature difference compared to the temperature law of the wall is illustrated in Figure 9.1c. Based on the RSM prediction, the turbulent Prandtl number, Pr_t , is 0.85 in the log-law region. Compared to the temperature law of the wall, the temperature profile is solved satisfactorily. T^+ ($\propto (T - T_w)$) is defined as zero in the first cell, as $T = T_w$, explaining the discrepancy at $y^+ = 1$.

The dimensionless turbulent dissipation rate as predicted by the RSM model is depicted in Figure 9.1d and compared to the DNS data of Mansour et al. (1988) with $Re_\tau = 180$. Compared to the DNS data, the RSM model overestimates the dissipation near the wall with a maximum at $y^+ = 10$. However, these results are deemed satisfactory.

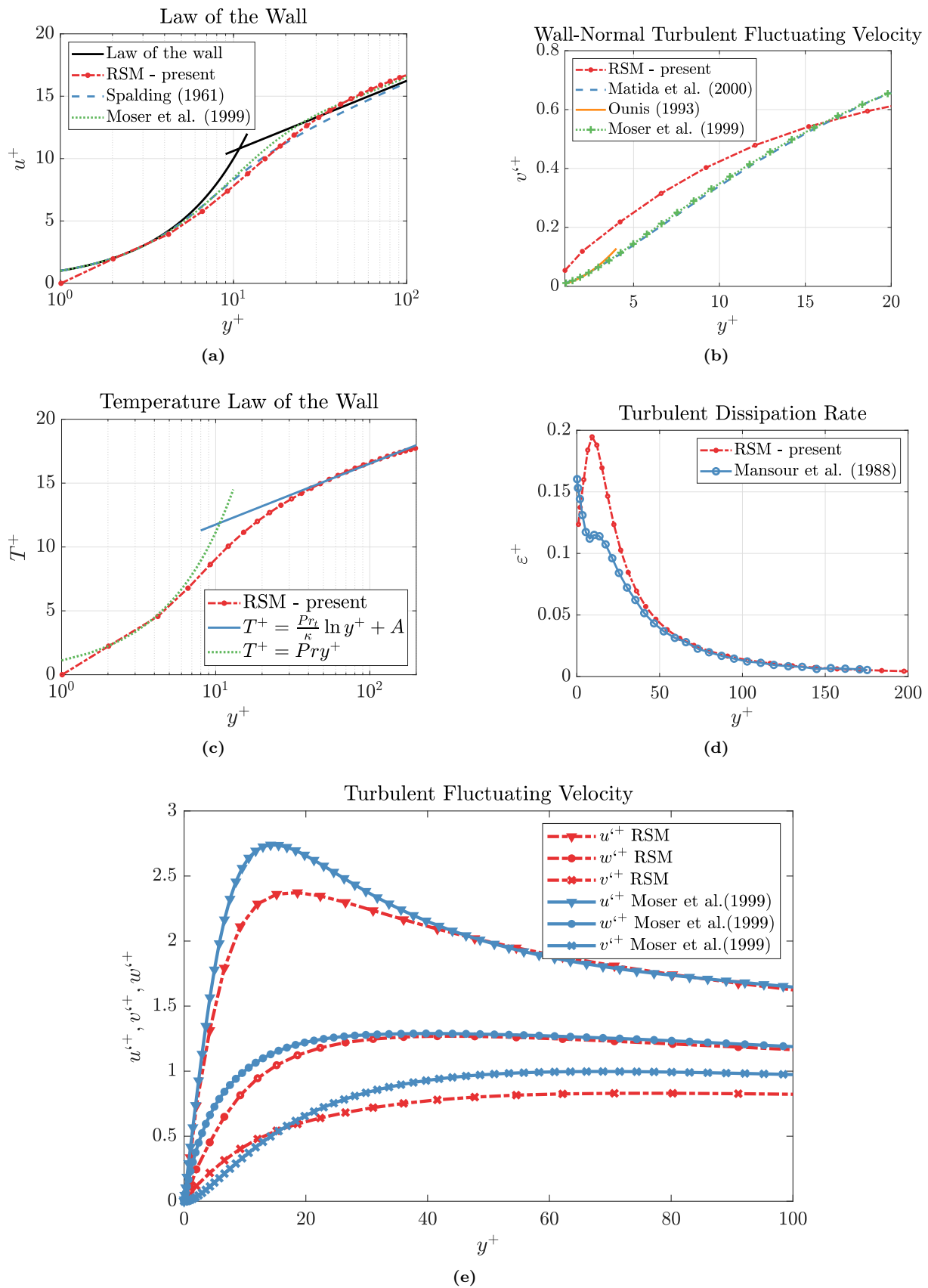


Figure 9.1: Dimensionless cross-sectional profiles of mean and turbulent flow variables at the location of the particle injection ($x_{inj} = 50\text{mm}$) versus the dimensionless wall distance, y^+ . The results are compared with DNS data.

9.1.2 Discussion

The prediction of the wall-normal fluctuation velocity component, illustrated in Figure 9.1b, is not satisfactory for the present application of the fluid flow field, especially in the near-wall region. The quadratic variation is not captured, even though low-Reynolds correction to the enhanced wall treatment was employed on the most elaborate RANS turbulence model, the RSM. Tian and Ahmadi (2007) made similar conclusions and address a default algorithm in ANSYS Fluent that uses linear interpolation of flow field variables between nodal points as a possible reason for this result.

The enhanced wall treatment includes a simple algebraic model for the turbulent dissipation rate, ε , near the wall. In addition, the dissipation term ε_{ij} in the transport equations for the Reynolds stresses is modelled in the RSM, as described in Equation 4.7. As a result of these model simplifications, the inhomogeneous contributions of the turbulent dissipation rate, as elaborated by Jovanović et al. (1995), is not appropriately captured by the RSM model (see Figure 9.1d). However, possible implications of these deviations in the wall region are not further investigated in this study.

When a constant temperature gradient is imposed on the walls by employing a constant heat rate, the fluid flow temperature reduces along the channel. However, this does not affect the flow field, because the fluid properties are set constant. The temperature profile depicted in Figure 9.1b is well-predicted at x_{inj} , and it is deemed fully developed. The temperature gradient is checked for consistency along the channel, and Equation 4.22 is shown to be accurate for the fluid flow considered.

In general, the flow simulation results of the main components in the domain are considered sufficient for the particle simulations. However, the simulation results for the crucial wall-normal fluctuating velocity were inaccurate and considered unsatisfactory for the present application. As a result, a boundary layer model for this fluctuating velocity component has been implemented, as described in Chapter 7. Simulation results with and without the boundary layer model are presented in Figure 7.10.

9.2 Particle Tracking

In this section, the concentration profiles and deposition velocities of 1 nm to 500 nm particles predicted by the Discrete Phase Model (DPM) in ANSYS Fluent are presented, and the results are compared with theoretical and empirical correlations. The DPM employs the particle model as elaborated in Chapter 7 and the above-mentioned steady-state flow simulation results for the three different conditions evaluated herein to predict particle trajectories. At last, the model predictions are discussed.

9.2.1 Concentration Profiles

The predictions of the normalised particle concentration profiles using the implemented improved-DRW model versus the normalised half channel width, $\xi = y/h$, are presented in Figure 9.2. For $d_p = 1$ nm the normalised concentration profile is predicted around unity and reducing drastically in the near wall region. The normalised concentration profiles for the remaining particle sizes are similar to each other. Here, the near-wall concentration is small, a peak of $\tilde{c} = 1.8$ is predicted at approximately $\xi = -0.9$, and in the core-flow of the pipe the normalised concentration is below unity.

In Figure 9.2f, the five normalised concentration profiles are presented versus the dimensionless wall distance, y^+ . Here, it is evident that the concentration in the first cell is smallest for the smallest particle. In general, the normalised concentration are increasing with particle size for $y^+ < 10$.

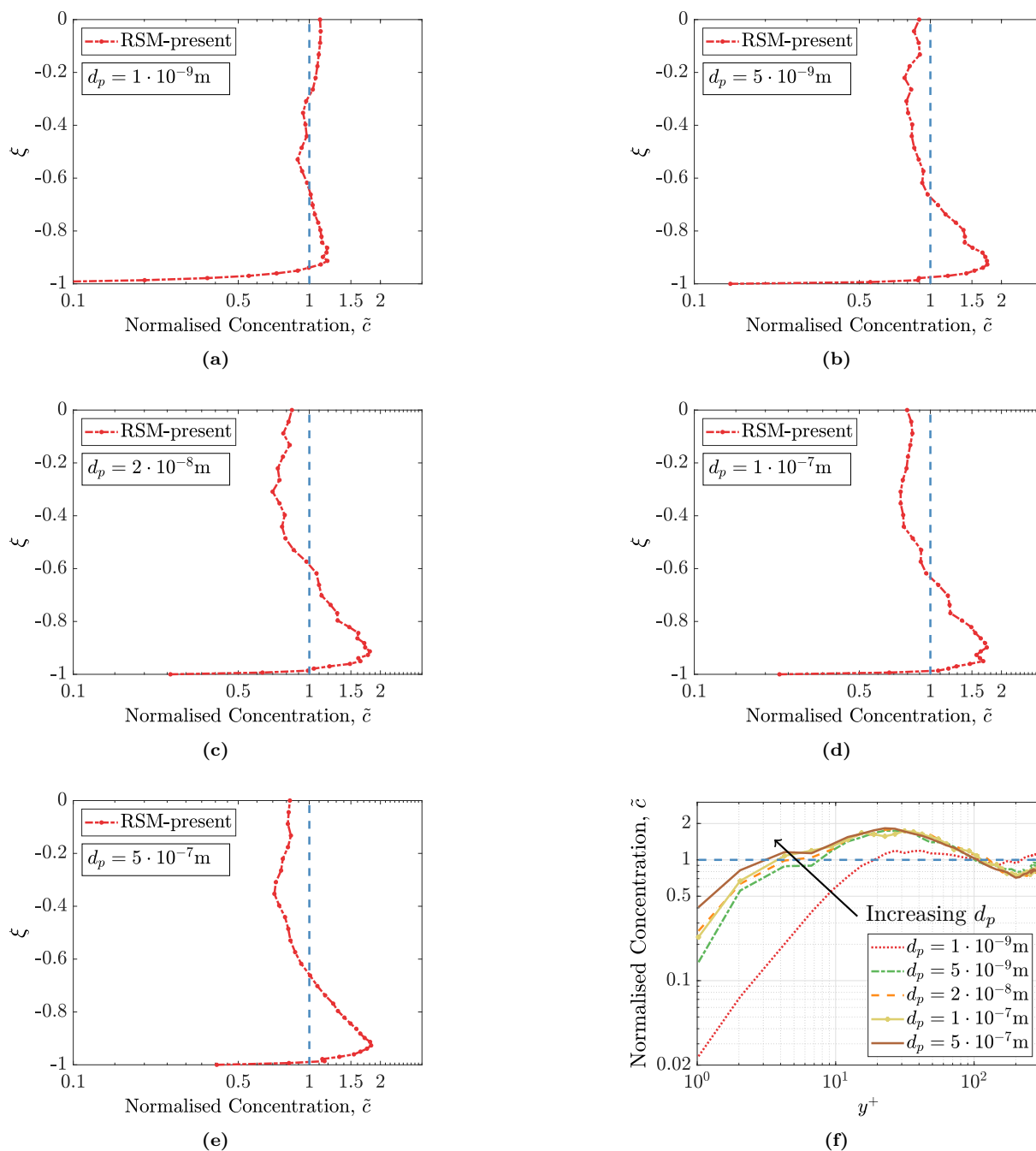


Figure 9.2: Concentration profiles for particles diameters of 1 nm to 500 nm, simulated at $p = 50$ bar conditions. In (a) to (e), the normalised concentration are presented versus the normalised half channel width, $\xi = y/h$. In (f), the normalised concentration is presented versus the dimensionless wall distance, y^+ , for the five particle sizes.

9.2.2 Deposition Velocity

The results for particle deposition are presented as the dimensionless deposition velocity, V_d^+ versus the dimensionless particle relaxation time, τ_p^+ (see definitions in Section 5.2.1). In Figure 9.3, 9.4 and 9.5, the results are presented for $p = 50$ bar, $p = 150$ bar and $p = 275$ bar, respectively, and compared to the numerical correlation of Fan and Ahmadi (1993) and the Colburn analogy to heat transfer.

The deposition velocities are generally overpredicted in the diffusion-dominated regime ($\tau_p^+ < 0.1$). Compared to the empirical correlation of Fan and Ahmadi (1993), the results deviate at most with a factor of five. In Figure 9.3, results for 1 nm to 10 μm are presented to validate the model for the eddy-diffusion-impaction regime. For $\tau_p^+ > 1$, the results correlate satisfactory compared to the empirical correlation.

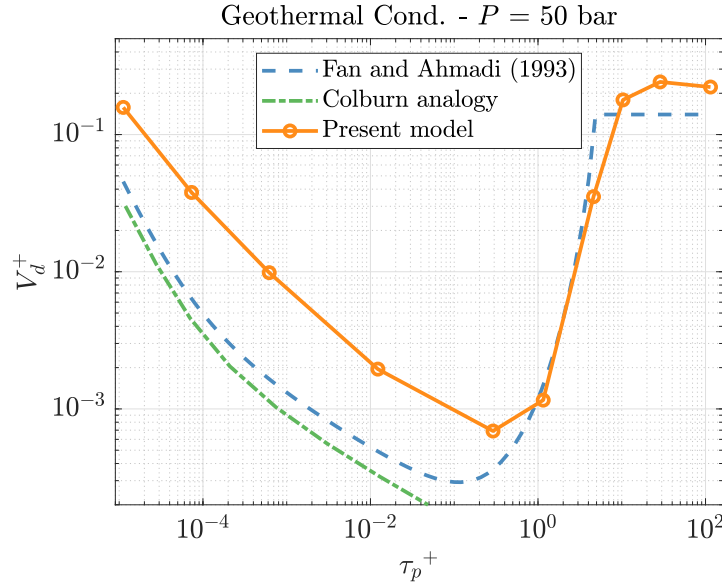


Figure 9.3: The dimensionless deposition velocity versus the dimensionless particle relaxation time for $p = 50$ bar compared to the numerical correlation of Fan and Ahmadi (1993), the experimental correlation of Papavergos and Hedley (1984) and the Colburn analogy to heat transfer.

Below, parameter studies are performed to evaluate effects of a thermal gradient and wall roughness on the particle deposition. As the dimensionless prediction trends are similar for the three different conditions, possible sensitivities are assumed to be similar as well. The parameter studies below are performed in the $p = 50$ bar-conditions as simulations with these conditions are most computer efficient.

Roughness

To make a good comparison with the deposition velocity from the experimental measurements, the effect of roughness needs to be included in the numerical simulations. Therefore, the the maximal surface roughness of the employed tubes were accounted for by including the roughness model (see Section 5.2.4). The dimensionless roughness parameter is $k^+ = 0.7$. The results are depicted in Figure 9.6 and compared to the numerical correlation of Fan and Ahmadi (1993) and the Colburn analogy to heat transfer. The enhancement of the employed surface roughness is compared to the correlation of Fan and Ahmadi (1993) with $k^+ = 0.7$. The deposition velocity is enhanced for $\tau_p > 10^{-3}$. The enhancement trend is similar to the empirical model for roughness by Fan and Ahmadi (1993), where the enhancement is most significant for $0.01 < \tau_p^+ < 1$.

Thermophoresis

As introduced in Section 5.1.3, deposition is enhanced when particles are prone to a thermal gradient in the flow. In Figure 9.7, the predicted thermophoretic effect of a 10 K temperature gradient on particle

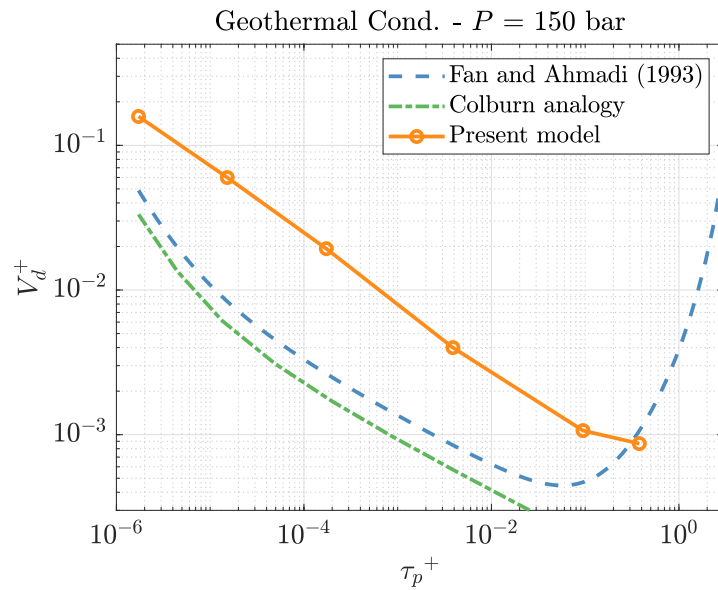


Figure 9.4: The dimensionless deposition velocity versus the dimensionless particle relaxation time for $p = 150$ bar compared to the numerical correlation of Fan and Ahmadi (1993), the experimental correlation of Papavergos and Hedley (1984) and the Colburn analogy to heat transfer.

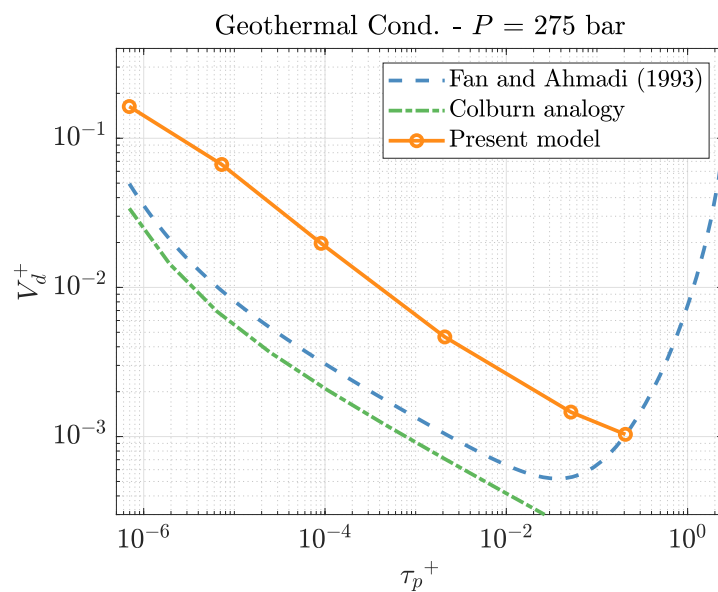


Figure 9.5: The dimensionless deposition velocity versus the dimensionless particle relaxation time for $p = 275$ bar compared to the numerical correlation of Fan and Ahmadi (1993), the experimental correlation of Papavergos and Hedley (1984) and the Colburn analogy to heat transfer.

deposition velocity is illustrated. The enhancement of thermophoresis becomes of significance for $\tau_p > 0.01$ and the predictions follow the same trend as the correlation of He and Ahmadi (1998). However, the enhancement is smaller with the present model for $0.01 < \tau_p < 2$ compared to the empirical correlation.

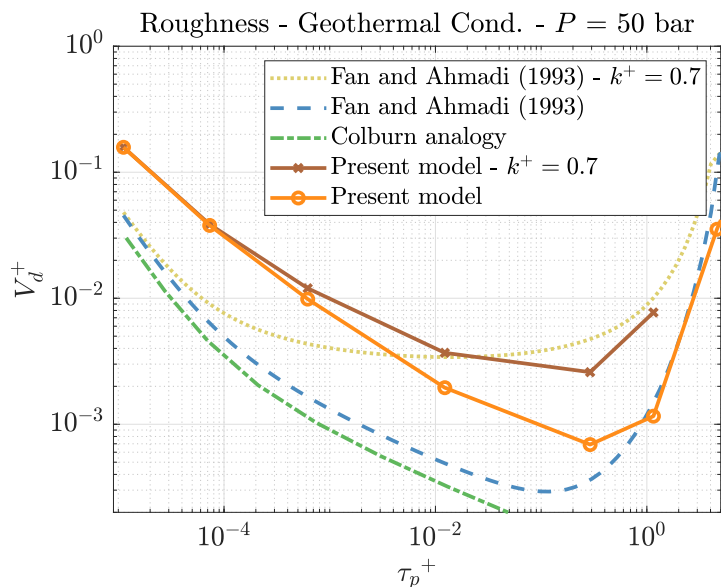


Figure 9.6: The dimensionless deposition velocity versus the dimensionless particle relaxation time for $p = 50$ bar compared to the numerical correlation of Fan and Ahmadi (1993), the experimental correlation of Papavergos and Hedley (1984) and the Colburn analogy to heat transfer.

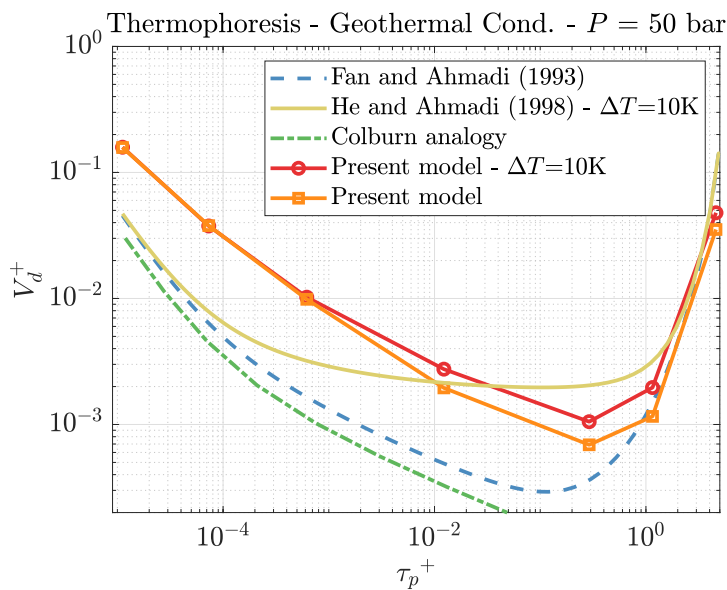


Figure 9.7: The dimensionless deposition velocity versus the dimensionless particle relaxation time for $p = 50$ bar when the effect of thermophoresis is included. The results are compared with the numerical correlation of Fan and Ahmadi (1993), He and Ahmadi (1998) and the Colburn analogy to heat transfer.

9.2.3 An Alternative Presentation of the Results

As introduced in Section 5.2.5, the present numerical results can be compared with experimental measurements from the literature by evaluating the data with Equation 5.43. The results are presented in Figure 9.8a. In this presentation of the results, the predictions are overestimated by a factor of about five and the numerical results are scattered out along the y-axis. A detailed plot of the numerical predictions are presented in Figure 9.8b, where the results are coloured by the pressure-condition and marked by the particle size. Here, the particle sizes are grouped in intervals. For the three pressure conditions, the results

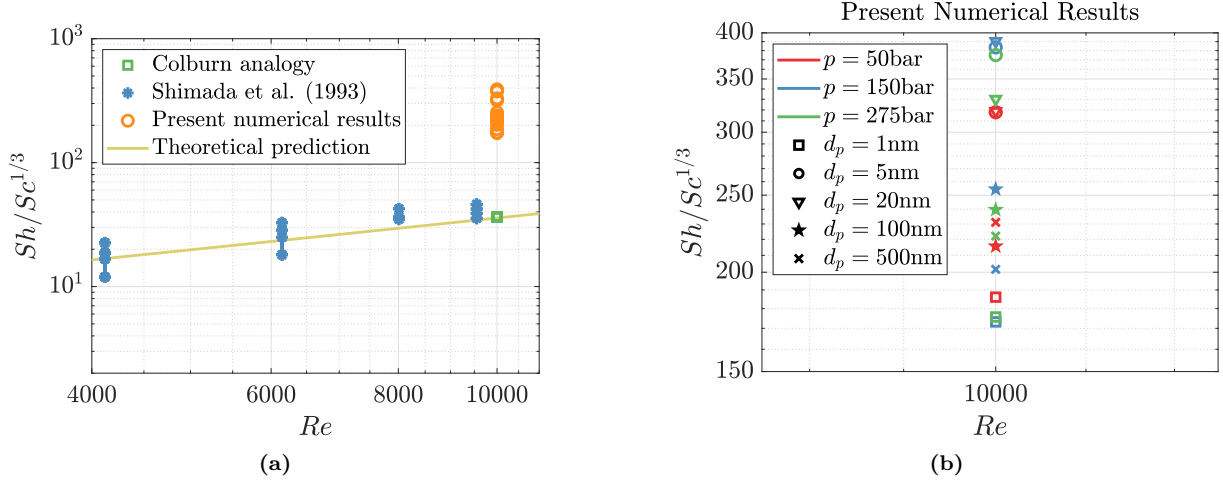


Figure 9.8: (a) The present numerical results, theoretical predictions with Equation 5.43, the Colburn analogy to heat transfer and experimental results of Shimada et al. (1993) are presented for $Sh/Sc^{1/3}$ versus the Reynolds number. (b) A detailed view on the present numerical results at different geothermal conditions (coloured) and particle diameters (marked).

predicted for $d_p = 1$ nm are below 200, for $d_p = 5$ nm and 20 nm above 300 and for $d_p = 100$ nm and 500 nm between 200 and 260. No general trend is observed in the predictions based on the case considered (coloured data). However, the predictions of $d_p = 5$ nm, 20 nm and 100 nm for the $p = 50$ bar-condition are closer to the theoretical predictions for the respective groups of particle sizes.

9.2.4 Sensitivity Analysis - Improved-DRW

In this subsection, a sensitivity analysis is presented to elucidate the effect of modifications to the correction terms in the SI-DRW implemented in the PARTICLE model. The aim of this SI-DRW model is to diminish the spurious drift caused by the conventional-DRW, by correcting the modelled instantaneous fluctuating velocity. For sake of clarity, the model for the instantaneous fluctuating velocity is repeated here

$$u_i'^{m+1} = \zeta_i \gamma_i + \overline{u_i'^{m+1}}, \quad (9.1)$$

where

$$\overline{u_i'^{m+1}} = \overline{u_i'^m} + \frac{1}{1 + Stk} \left(\underbrace{\gamma_i \frac{\partial \gamma_i}{\partial x_j}}_{(A)} - \underbrace{\frac{\gamma_i^2}{T_L} \frac{\partial T_L}{\partial x_j}}_{(B)} \right) \Delta t. \quad (9.2)$$

Here, u_i' is the modelled instantaneous fluctuating velocity, γ_i is the mean fluctuating velocity, $\overline{u_i'}$ is the mean drift velocity correction, and the two correction terms are named A and B . It is worth mentioning, that correction term A leads to a particle transport away from the wall, whereas correction term B leads to a particle transport towards the wall. For more details on the improved-DRW, the reader is referred to Section 5.1.5. In the sensitivity analysis, different factors were included on the two correction terms (A and B) to estimate the sensitivity of the implemented model. By defining a sensitivity parameter Θ , Equation 9.2 can be rewritten to

$$\overline{u_i'^{m+1}} = \overline{u_i'^m} + \frac{\Delta t}{1 + Stk} \cdot \Theta. \quad (9.3)$$

For the improved-DRW $\Theta = (A - B)$, where A and B are the correction terms in Equation 9.2. The sensitivity was evaluated based on the following five cases:

- I) $\Theta = (2A - B)$

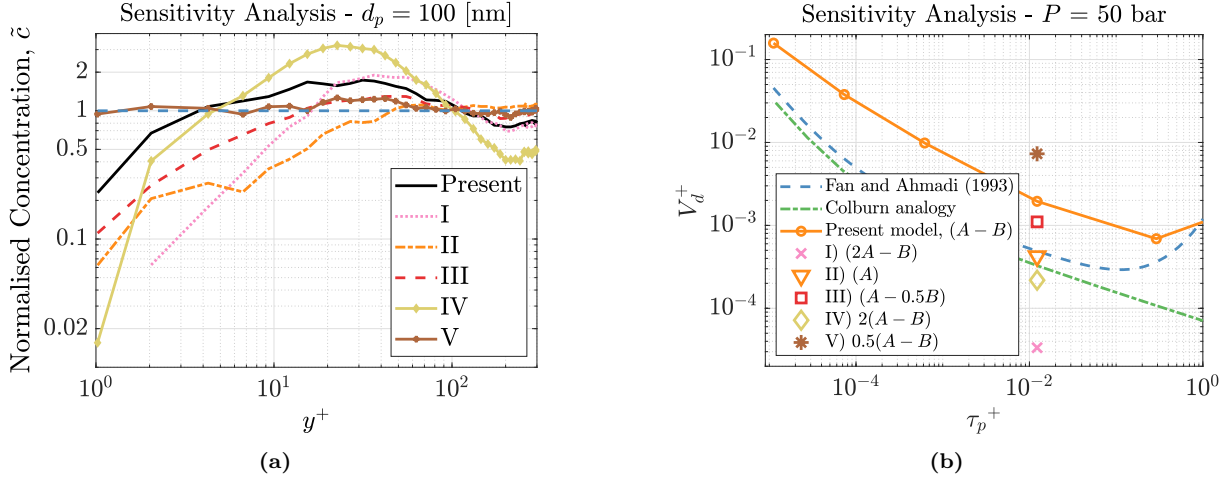


Figure 9.9: The results of the sensitivity analysis of $d_p = 100$ nm for $p = 50$ bar for the cases I-V. (a) The normalised concentration profile versus the dimensionless wall distance. (b) The dimensionless deposition velocity versus the dimensionless particle relaxation time.

- II) $\Theta = (A)$
- III) $\Theta = (A - 0.5B)$
- IV) $\Theta = 2(A - B)$
- V) $\Theta = 0.5(A - B)$

Based on the effects of the correction terms, the particle transport away from the wall should be enhanced in case (I), and in case (II) and (III) the particle transport towards the wall should be reduced. Case (IV) and (V) evaluate the sensitivity if both correction terms are enhanced or reduced. In general, case (I-IV) should lead to a particle transport away from the wall, relative to the present simulations. In case (V), the relative particle transport should be directed towards the wall, since the correction to the spurious drift is reduced.

Results of the Sensitivity Analysis

The results of the sensitivity analysis are presented in Figure 9.9, where Figure 9.9a illustrates the normalised concentration profiles versus the dimensionless wall distance. Here, the black line represents the PARTICLE simulation results with the SI-DRW model of $d_p = 100$ nm. As expected, when the netto particle transport towards the wall is reduced (case (I),(II) and (III)), the near-wall concentration of particles is decreased, as depicted in Figure 9.9a. Similarly, the near-wall concentration is reduced when the total correction is increased (case (IV)). When the effect of the correction term is reduced (case (V)), the normalised concentration is much higher in the wall-region.

In Figure 9.9b, the dimensionless deposition velocity versus the particle relaxation time is presented for the five cases. As references to this sensitivity analysis, the present results, the numerical correlation of Fan and Ahmadi (1993) and the Colburn analogy to heat transfer are included in the figure. From Figure 9.9 it is evident that the predicted deposition velocity is correlated to the near-wall particle concentration. Highest deposition velocity is predicted for case (V), where also the highest near-wall concentration is predicted. In cases (I-IV), where the netto transport of particles towards the wall is reduced, a lower deposition velocity is predicted compared to the present model. In general, the effect of this sensitivity analysis on the deposition velocity is considerable.

9.2.5 Discussion

In this subsection, the results from the PARTICLE model are discussed. The discussion is structured as follows:

- Shapes of concentration profiles

- Predictions of velocity for various conditions
- Applicability of the PARTICLE model

Concentration Profiles

The shape of the concentration profiles should be governed by the turbulent mixing, the near-wall diffusion rate (the Schmidt number) and the inertia effect on the particles. The latter can be determined based on the Stokes number or the particle relaxation time and is related to the size and density of the particle and fluid properties. The submicron particles evaluated in the present study have small Stokes numbers, which means that the particles follow and interact with the turbulent eddies throughout the eddy-lifetime. The random nature of the turbulent mixing suggests a uniform concentration profile. However, due to the inclusion of deposition in the PARTICLE model and the diffusion effects in the wall region, the concentration of particles at the wall is zero and a concentration gradient near the wall is induced. The submicron particles are strongly influenced by Brownian motion in the wall region. This effect increases with smaller particle sizes. So, due to the small Stokes numbers, analogies can be made to mass transfer relations. The lowest concentration gradients should be observed for the smallest particles, as Brownian motion is strongest for these particles and the diffusive sublayer thickness reaches farther into the flow. When the particles become bigger, the Brownian motion and the diffusive sublayer thickness reduces, and the influence of the turbulent mixing is introduced closer to the wall. The shape of the concentration profile is also dependent on the turbulence kinetic energy, as higher Reynolds numbers would reduce the height of the viscous sublayer. The turbulence would then have stronger effects on the particles closer to the wall.

The normalised concentration profiles presented in Figure 9.2 illustrate essential improvements on the physical representation of submicron particle dispersion with the PARTICLE model, as elaborated in Section 7.3. The spurious drift of particles produced by the SC-DRW model is diminished with the implementation of the SI-DRW model.

By evaluating the concentration profiles of the different particle sizes in Figure 9.2f, it is evident that the near-wall concentration increases with particle size. This trend is similar to the theoretical predictions described in the paragraph above. It is also clear from Figure 9.2f that the Brownian motion is strongest and diffusive sublayer thickness is largest for the smallest particles. It is worth mentioning that stronger diffusion (Brownian motion) also mean higher deposition rates of particles on the wall.

The predicted concentration profiles at the three geothermal conditions evaluated are almost identical for the respective particle sizes. Only the results from the $p = 50$ bar-conditions are presented here. It is noted that the small discrepancy in the shape of the concentration profiles near the wall for the respective particle sizes, can be related to the change in the Schmidt numbers and above-mentioned theoretical predictions.

The theoretical predictions on the dimensionless concentration profiles also holds when comparing the shape to ambient conditions. For the smallest particle considered at geothermal conditions in Figure 9.2f, $Sc = 2.6$, and for the smallest particle considered for ambient conditions in Figure 7.8b, $Sc = 264$. Therefore, a higher diffusion rate is expected at geothermal conditions. By inspection of these figures, it is evident that the normalised concentration is lowest at $y^+ = 1$ for the geothermal case. Thus, higher diffusion in the geothermal case.

The trends of the normalised concentration profiles predicted by the PARTICLE model for different particle sizes and Schmidt numbers are confirmed by the theoretical predictions, as discussed above. In addition, similar trends in the normalised concentration profiles are described in the numerical simulations of Mofakham and Ahmadi (2019) and Mofakham and Ahmadi (2020). Guha (2008) argued that deposition of small particles can simply be described by Fick's law of diffusion, with turbulent diffusion and Brownian motion as the two contributions. These two contributions are discussed above.

The sensitivity analysis elucidated the effects of the two correction terms in the implemented SI-DRW when amplified or reduced. The concentration profiles in the five cases considered in the sensitivity analysis are not necessarily more correct. However, tuning of the model might become relevant to develop the numerical model further. Emphasis is put on validating the concentration profiles with model predictions and theoretical predictions from the literature, similar to the law-of-the wall for velocity profiles. This might lead to better predictions of the deposition velocity.

Deposition Velocity

The model predictions for the deposition velocities are generally good. The PARTICLE model with the boundary layer model of Ounis, Ahmadi and J. B. McLaughlin (1993) and the improved discrete random walk (DRW) model of Mofakham and Ahmadi (2020) have addressed the challenges with the default deposition model for submicron particles in ANSYS Fluent. The validation of the implemented model at ambient conditions (see Chapter 7) was promising. At ambient conditions, the smallest particle evaluated ($\tau_p^+ = 1.2 \times 10^{-4}$) were overpredicted by a factor of two. For greater particle sizes in the diffusion-dominated regime, the predictions were very good compared to experimental and numerical results and empirical correlations (Fan and Ahmadi 1993; Mofakham and Ahmadi 2020; Papavergos and Hedley 1984; Shimada et al. 1993; Wood 1981). In addition, a more physical boundary condition for particle deposition is implemented in the PARTICLE model, resulting in a more physical interpretation. A particle is taken as deposited when its surface touches the wall.

Before discussing the PARTICLE model predictions for geothermal conditions, it should be mentioned that the Schmidt numbers of submicron particles at the geothermal conditions considered, are smaller than for particles in ambient air. The theoretical predictions of Fan and Ahmadi (1993) and Wood (1981) state that $V_d^+ \propto Sc^{-2/3}$ for particles for diffusion-dominated submicron particles. From this it follows that the dimensionless deposition velocity is higher in the geothermal conditions, as the diffusion is stronger at geothermal conditions. This is correct down to $d_p = \mathcal{O}(1 \text{ nm})$, where the Schmidt numbers are similar. This is related to the high Knudsen numbers of nano-particles dispersed in air. So, when the model is applied to the geothermal conditions evaluated in the present study, the dimensionless deposition velocity for submicron particles is predicted up to two orders of magnitude higher than in ambient air. This is especially significant for $d_p = 100 \text{ nm}$ and $d_p = 500 \text{ nm}$.

When the PARTICLE model is applied to geothermal conditions, the dimensionless deposition velocity is over-estimated up to a factor of five compared to the Colburn's analogy to heat transfer and the empirical correlation of Fan and Ahmadi (1993). This overprediction is consistent for the geothermal conditions and might be related to the change of fluid properties or the necessary change of models due to applicability. For instance, the implemented model for mean free path is general for gases and have a significant effect on the physical behaviour of the particles. The smallest particles evaluated have Knudsen numbers above unity, leading to corrections with the Cunningham correction factor on the drag force, the relaxation time of the particle and the Brownian motion. No alternative model is found for mean free path for water vapour. The model for Brownian motion (see Section 5.1.4) applied in the PARTICLE model is widely employed in numerical models of dispersed particles in air (Gao et al. 2012; Mofakham and Ahmadi 2020; Tian and Ahmadi 2007). The applicability range of the model is however never stated. Further investigations on the applicability of the model for Brownian motion is emphasised for further work.

The presentation of the results with $Sh/Sc^{1/3}$ versus the Reynolds number in Figure 9.8 reveals some interesting insights. Here, the particle deposition rates can be compared with experimental data at ambient condition, e.g. (Shimada et al. 1993), by assuming that the particles are dominated by diffusion. The overestimation with present numerical results is also clear in Figure 9.8, and the consistency of the overprediction for the three conditions is confirmed. By evaluating the results with regards to the particle size and the fluid properties in Figure 9.8b, the results appear to be scattered in particle groups. Particle sizes of 5 nm and 20 nm have high values of $Sh/Sc^{1/3}$ and are overpredicted the most compared to the theoretical predictions. In contrast, the smallest particles are estimated closest to the theoretical predictions. This observation coincides with the relative discrepancy to the Colburn analogy in Figure 9.3, Figure 9.4 and Figure 9.5, but are more evident in Figure 9.8b.

Another interesting observation in Figure 9.8b is the differences of deposition rates based on geothermal conditions. For $d_p = 5, 20$ and 100 nm , the deposition rates are lower for the $p = 50 \text{ bar}$ -condition. This is possibly related to the numerical schemes employed at the different conditions. In the $p = 50 \text{ bar}$ -conditions, either a higher-order scheme or a refined time-step was employed compared to $p = 150 \text{ bar}$ and $p = 275 \text{ bar}$ -conditions. This prioritisation of accuracy was related to computational time of the particle tracking. Computational time is further discussed in Section 9.2.5. In general, the higher-order scheme, trapezoidal, introduce a higher accuracy compared to the lower-order analytical scheme, and hence, a smaller deposition velocity was in general also observed. If the same numerical scheme had been applied to the $p = 150 \text{ bar}$ and $p = 275 \text{ bar}$ -conditions for $d_p = 5, 20$ and 100 nm , the results would possibly coincide

to a larger extent.

The sensitivity analysis revealed the importance of implementing a model with proper correction for the turbulent fluctuations. When amplifying and reducing the correction term in the SI-DRW in the PARTICLE model by a factor of two, the dimensionless deposition velocity differed by almost two orders of magnitude. Tuning of the model is emphasised as a further work. In addition, when validation with the experimental data is possible, the physical behaviour of the particle flow can be ensured with the concentration profile, and an improved version of the present model can be developed.

To test the enhancement related to thermophoresis, a temperature difference of 10 K is imposed on the fluid flow. This is equivalent to a total thermal gradient of 145 K/cm. By evaluating Figure 9.7 and the interpolation formula of Talbot et al. (1980) in Figure 5.1, a correspondence between the thermophoretic coefficient, η_T , and the enhanced deposition velocity is observed. η_T is in general expected to be higher at the geothermal conditions, as the thermal conductivity is higher than for ambient conditions of air. For a lower particle-fluid thermal conductivity ratio, $\Lambda = k_p/k_f$, the thermophoretic coefficient is enhanced.

However, the estimated enhancement of thermophoresis is lower than the empirical correlation of He and Ahmadi (1998). In Figure 9.7, the deposition velocity enhancement is negligible for $\tau_p^+ < 1 \times 10^{-3}$, even though the thermophoretic coefficient is largest for $d_p = 20$ nm. The enhancement is more significant for $0.01 < \tau_p^+ < 1$. This overall underestimation of thermophoresis might be related to the predicted concentration profile. As very high diffusive rates are predicted by the PARTICLE model, the near-wall concentration is lower. Hence, less particles are affected by the higher temperature gradients near the wall. This is another indication that the diffusion is overpredicted by the PARTICLE model. It is worth mentioning that the employed interpolation formula of Talbot et al. (1980) estimates much higher η_T than the more recent interpolation formula of Young (2011) (see Figure 5.1). If this model was employed here, the enhancement of for $0.01 < \tau_p^+ < 1$ would probably be of less significance.

A roughness model (see Section 5.2.4) was implemented to account for roughness effects in the present experimental investigation, where the dimensionless surface roughness of $k^+ = 0.7$ is expected. The model predictions show an enhanced deposition velocity for particles $5 \times 10^{-4} < \tau_p^+ < 1$. The trend of enhancement is very similar to the empirical correlation of Fan and Ahmadi (1993), when a similar roughness is taken into account. This was expected, because the present roughness model is taken from Fan and Ahmadi (1993). This can be seen as a validation of the roughness model, as the empirical correlation of Fan and Ahmadi (1993) was described based on experimental measurements of deposition in rough pipe sections.

Applicability of the Present Model

In Section 9.3, the methodology for comparing and validating the numerical predictions with the present experimental measurements is presented. Validation of the present numerical model is essential to facilitate further investigations on submicron particle deposition from superheated and supercritical water vapour in other geometries. For further investigations with the present model, a proper discussion on its applicability is necessary.

Throughout this thesis, Colburn's analogy to heat transfer and the empirical correlation of Fan and Ahmadi (1993) have been included as references to the numerical results of the particle deposition results to assess accuracy. As described in Section 5.2.4, the correlation of Fan and Ahmadi (1993) accounts for roughness and gravity, and if employed with the findings in He and Ahmadi (1998), thermophoresis can also be accounted for. For conventional purposes in simple geometries, such as straight pipes, channels, ducts or flat plates, the correlation of Fan and Ahmadi (1993) has shown good coherence with experimental results (Fan and Ahmadi 1993; He and Ahmadi 1998). However, one of the objectives in the project of NTNU and Equinor on IDDP is to establish numerical tools to simulate particle deposition in more complex geometries and to facilitate model developments.

As the PARTICLE model is implemented in ANSYS Fluent, it is applicable to more complex geometries such as pipe bends and turbine blades. With the PARTICLE model, development by adding other contributions to the particle behaviour, for instance wall bounding effects, agglomeration and particle size distributions, is facilitated. The PARTICLE model is also applicable to simulating particle trajectories in the eddy-diffusion-impaction and the inertia-dominated regime, as shown in Figure 9.3. As a more general remark, the PARTICLE model is validated with numerical and experimental results for simulating submicron particles in ambient air, and is therefore applicable to a wide range of conditions

and geometries for particle-laden flows.

In this numerical model, the Euler-Lagrangian mathematical approach has been employed. The physical interpretation and implementation of transport and deposition mechanisms for submicron particles are reported to be simpler using this approach (Elghobashi 1994; Gao et al. 2012; Guha 2008) compared to the Euler-Euler approach. For instance, implementing a model for the wall bounding forces would be simple if the theory was well-known. However, difficulties in numerical accuracy and computational time had arisen when the model was applied to the geothermal conditions. For the evaluated particle sizes, the particle relaxation time is very small ($\tau_p < 1 \times 10^{-10}$ for $d_p = 1$ nm). If good accuracy should be maintained, a higher-order scheme is employed. The time step (dt) should be of the same order as the particle relaxation time, and in the ideal case, $dt < \tau_p/2$ to ensure that the physical behaviour of the particle transport is captured. The particle relaxation time is related to the acceleration time from a still situation to reaching the fluid velocity, and if $dt > \tau_p$, some changes to the particle trajectory are omitted. The effect of the higher time step is possibly of highest significance in the vicinity of the wall. Higher particle deposition is observed when the lower order scheme employed, using a time step several orders of magnitude larger than the particle relaxation time. Elsewhere, the particles are anyway randomly distributed, and the detailed particle behaviour is deemed insignificant. This reasoning is confirmed by the identical concentration profile results using different time steps and numerical schemes.

In order to obtain a higher-order accuracy for all the particle sizes, a time step of at minimum $dt = \mathcal{O}(10^{10})$ should be employed. For the given length of the domain (0.2 m) and the mean fluid velocity (1 – 6 m/s), the number of time steps per particle trajectory is as high as $\mathcal{O}(10^9)$. In practice, with a time step of $dt = 5 \cdot 10^{-10}$, simulations of only 5000 particles lasted for 50 hours with one CPU. Such high computational costs for improved accuracy is undesirable and impractical. The difficulty related to the computational cost of the particle simulations reduces the applicability of the PARTICLE model. This issue is also described in Section 7.2.1.

9.3 Experimental Measurements and Numerical Predictions

In this section, the measurement results from the experimental investigation are presented and discussed. These results are compared with the numerical results based on particle size distributions given by the Department.

9.3.1 Measurement Results and Uncertainties

Preliminary Measurements

The experimental investigation related to the objectives in this thesis was delayed by IFE until late in May. Complications and leakage in the equipment provided by IFE made further delays inevitable. Therefore, only preliminary results from this experimental investigation can be presented here. The purpose of presenting the results from the preliminary experimental study of particle deposition, is to demonstrate the post-processing methodology and how numerical predictions can be compared with the experimental measurements of polydisperse particle distribution.

Results and Uncertainty Estimates

The preliminary results consist of only one more or less stable test with water vapour conditions of 150 bar and 406 °C in the test section. This experiment was susceptible to unstable flow in the test sections and unstable pressure and temperature in the autoclave. Additionally, the unstable conditions increased the air and steam consumption in the pressure controller and the autoclave, respectively, leading to a shorter duration time of the experiment. Nevertheless, it was decided that the uncertainty estimates should be based on experimental measurements conducted in more stable and reliable conditions.

In Table 9.1, the measurements related to this single experiment in the two test sections are presented. The uncertainty estimates are presented in the rightmost column. Special care should be taken on the weight measurements in test section 2. The shortened duration of the experiment and relatively high random uncertainty of the weight measurements on industrial scale, lead to a high absolute uncertainty for this measurement. It is worth mentioning that the ICP-MS analysis was not prepared by IFE, and only weight measurements were applied here.

Table 9.1: Uncertainty estimates for the dimensionless deposition velocity, V_d^+ .

Measured Variable	Units	Measurements		Uncertainty
		Test Section 1	Test Section 2	
Duration	[min]	36	36	3
$L_{test\ section}$	[mm]	51.55	49.20	0.05
D_{pipe}	[mm]	1.38	1.38	0.14
Δm	[mg]	1.3	0.1	0.1
Re	[-]	6,000	6,000	1,000

9.3.2 Particle Distribution and Calculation Procedure

Based on the precipitation and agglomeration model by Bordvik, Næss et al. (2021), the particle distribution in the two test sections are predicted. The particle range is between 1.7 nm to 120 nm, where the smallest particle size correspond to the critical size of generation. The particle concentration in mg of silica particles per k of water is presented in Figure 9.10a versus particle diameter in nm. To illuminate the distribution of number of particles in the flow, the particle mass is taken into account in Figure 9.10b. In the figures, the squares (\square) and circles (\circ) represent the first and second test section, respectively.

The model predicts a shift in the particle distribution towards bigger particles from the first to the second test section. This is mainly due to the accounted agglomeration of particles in the model. As bigger particles is related to lower deposition velocities in the diffusion-dominated regime, such a shift in the particle distribution would imply lower particle deposition on the wall. It is also evident from Figure 9.10

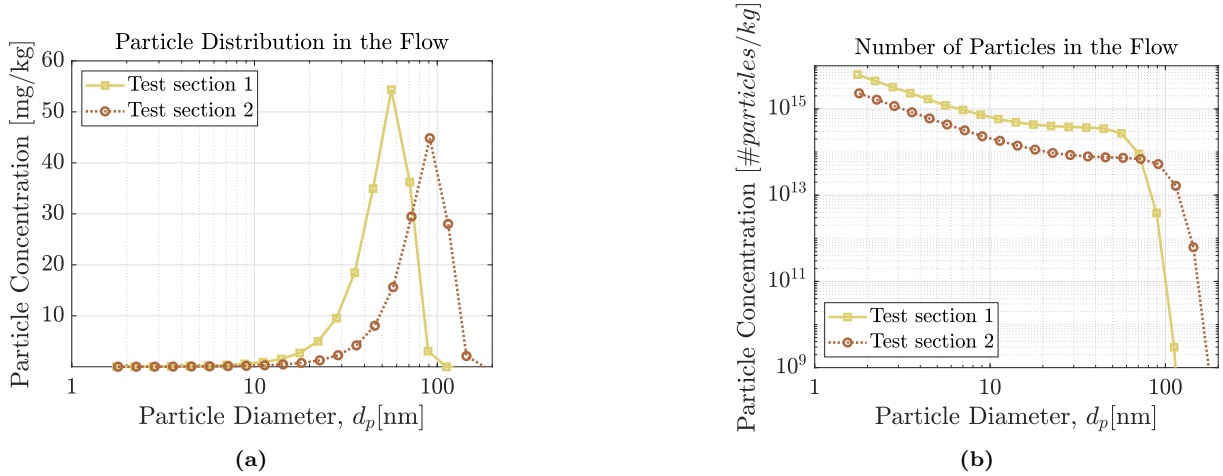


Figure 9.10: Predicted particle size distributions in the two test sections in the experimental rig. The particle size distribution is presented versus the mass concentration (a) and versus the number of particles concentration (b).

that the total concentration predicted by the model by Bordvik, Næss et al. (2021) is less in the second test section. This inconsistency is related to a simple deposition model implemented in the model, taken into account the mass of particles deposited between the two test sections.

The particle distribution profile is discretised into separate particle sizes, illustrated by the data points (\circ , \square). In order to assign deposition velocities for these discretised particle sizes, MATLAB was used to do linear interpolation based on the present predictions of V_d^+ for different τ_p^+ . Further on, an effective deposition velocity was obtained for a particle size i with concentration fraction of α_i with the following

$$V_{d^+_{eff,i}} = V_{d^+_i} \alpha_i. \quad (9.4)$$

The particle relaxation time, τ_p , was calculated based on the total number of particles and the total mass of the particles in the model.

9.3.3 Results

The effective deposition velocity based on the present predictions for superheated steam at 150 bar and 406 °C and the particle distributions in the two test sections are presented in Figure 9.11a versus τ_p^+ . The same calculation procedure has been performed with the empirical correlation for deposition velocity by Fan and Ahmadi (1993). These results are depicted in blue, with the \square representing the first test section and \circ the second test section. In Figure 9.11b, the deposition predicted by the present model in terms of milligram deposited per hour is illustrated for the particle size distribution in the two test sections. In total, the deposition is evaluated to be 15.2 [mg/h] and 9.5 [mg/h] in test section one and two, respectively.

Finally, we arrive at Figure 9.12. Here, the present experimental results, the present numerical results, and the numerical results based on the particle distributions are presented. The Colburn analogy and the empirical correlation of Fan and Ahmadi (1993) as a function of τ_p^+ and with considerations on the particle distributions are presented to assess references. The horizontal bars are included to illustrate the range of τ_p^+ for the particles considered. This is the same range of τ_p^+ as depicted in Figure 9.11a. The experimental results for the preliminary results show some coherence with the predictions based on the particle distributions. The deposition velocity based on the measurements in test section 1 is very similar to the estimations based on the correlation of Fan and Ahmadi (1993). The numerical prediction based on the particle size distribution is about one order of magnitude higher. The error bars related to the experimental measurements in test section two are significant, and based on the uncertainty analysis, the dimensionless deposition velocity can be in the range of 0 to 0.004.

In the predictions by Bordvik, Næss et al. (2021), the mean particle is estimated in the two test sections. In the numerical predictions of the deposition velocity using the methodology presented above,

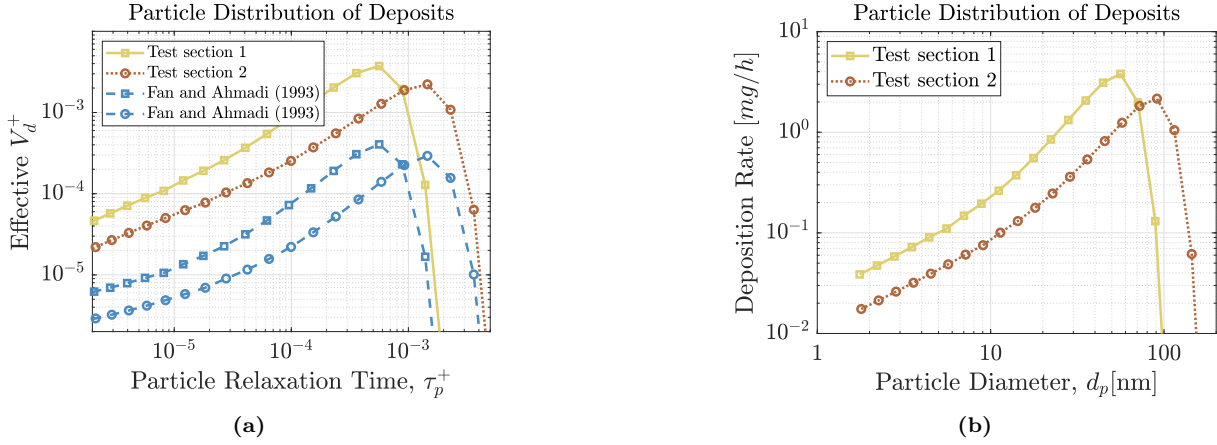


Figure 9.11: Deposition rates based on the present numerical results and the predicted particle size distribution, in test section 1 (a) The effective dimensionless deposition velocity versus the particle relaxation time for the present numerical results and the empirical correlation of Fan and Ahmadi (1993). (b) The deposition rate [mg/h] versus the particle diameter.

a significant lower deposition velocity is predicted based on this mean particle diameter. This is due to the shift in the particle size distribution and the effective deposition velocity (see Figure 9.11a) towards greater particles.

In Figure 9.13, the present experimental results are included in the alternative presentation with $Sh/Sc^{1/3}$ versus the Reynolds number. Here, the experimental measurement from the first test section correlates well with the theoretical predictions (the upper data point). The lower data point is from the experimental measurement in test section two.

9.3.4 Discussion

The lack of experimental data reduces this discussion to a matter of post-processing methodology rather than a discussion of dominant deposition mechanisms of silica particles in the present conditions. Likewise, the validation of the numerical models is not relevant in this discussion.

The uncertainty analysis elucidated a crucial aspect in experimental investigation. The measurements of the enhanced mass due to deposition should be of special attention, as this uncertainty was of particular significance in the preliminary results. In order to reduce this uncertainty, the duration of the experiments should be prolonged, the accuracy of the industrial scale increased, or the alternative and more accurate ICP-MS should be employed. When experiments are performed at even higher pressures and in the supercritical conditions of water, fewer particles are generated according to the classical nucleation theory (Bordvik, Næss et al. 2021). In addition, the equilibrium concentration of amorphous silica is increasing with pressure and temperature, reducing the number of particles in the flow. Therefore, lower deposition is expected in the water of supercritical conditions. Ensuring a significant particle deposition for these conditions is essential.

The model predictions of the particle size distribution in Figure 9.10 include the Colburn analogy to heat transfer to account for the deposition of particles between the test sections. However, the deposition is not estimated based on the different particle sizes; only the mean diameter and the total concentration is considered. This modelling of deposition is evident from Figure 9.10b, as there is no distinct change in the particle size distribution but the mean concentration. For submicron particles in the diffusion-dominated regime, deposition is decreasing for bigger particles. Over the span of particles accounted for in the particle size distribution, the dimensionless deposition velocity varies over an order of magnitude. Presumably, a sharper decrease in the concentration of the smallest particles should be observed in test section 2 compared to test section 1, if a more elaborate deposition model should be included. In addition, a more distinct shift of the particle size distribution profile towards bigger particles are expected.

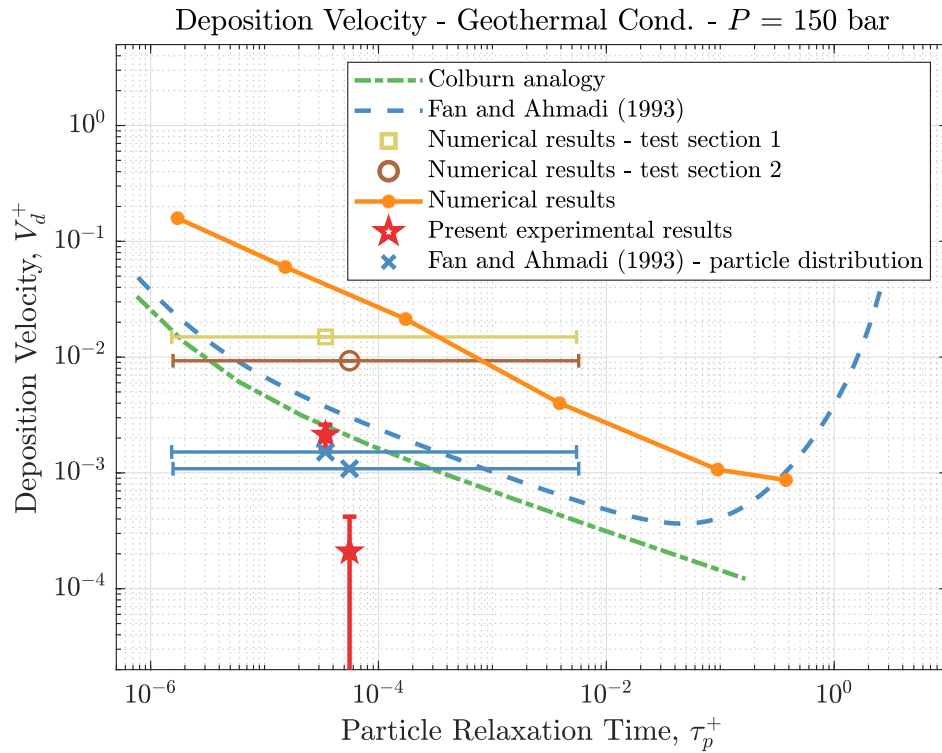


Figure 9.12: Presentation of the dimensionless deposition velocities from present experimental measurements (including uncertainties), predicted by the PARTICLE model and calculated based on the predicted particle size distribution of Bordvik, Næss et al. (2021). The horizontal bars represent the span of particles in the distribution in Figure 9.11a. Empirical results and a heat transfer analogy are included for comparison.

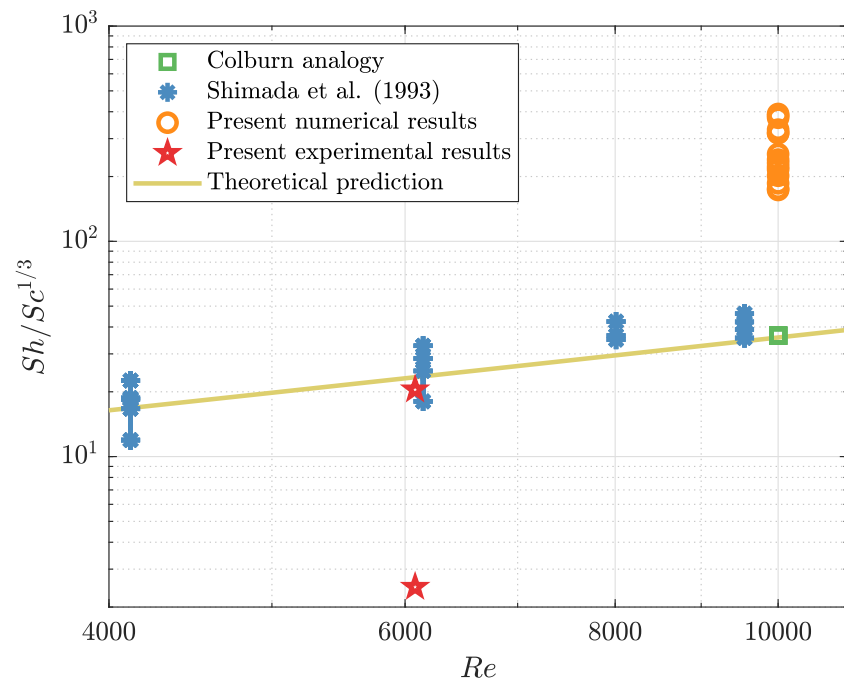


Figure 9.13: The results from the preliminary experimental investigation is presented with the alternative presentation of deposition rate ($Sh/Sc^{1/3}$). Here, the upper experimental data point is from test section 1 and the lower from test section 2.

10 | Conclusions and Further Work

10.1 Concluding Remarks

Submicron particle deposition from superheated and supercritical water vapour in turbulent channel flows was studied in this thesis using theoretical, numerical and experimental methods. A numerical model (PARTICLE) for submicron particle transport and deposition was established in ANSYS® Fluent Release 20.2 with the Euler-Lagrangian approach. The main focus of this thesis has been to explore the modelling possibilities and limitations and to better the predictions of submicron particle deposition. In this way, reasonable estimates of the deposition velocity of submicron particles generated from superheated steam supersaturated with silicic acid can be produced.

Initially, two main challenges with the default model in ANSYS Fluent were discovered. (1) The wall-normal mean fluctuating velocity ($\overline{v'^2}$) in the vicinity of the wall was overpredicted by the Reynolds stress Transport Model (RSM), leading to non-physical enhanced deposition. (2) The default particle model for generating the instantaneous velocity fluctuation in ANSYS Fluent, the so-called conventional-discrete random walk model (DRW), produced a spurious drift of particles towards the wall, leading to particle accumulation in the near-wall region and enhanced deposition. This drift is spurious as submicron particles of low inertia should be randomly distributed in a fully turbulent flow.

A boundary layer model for the wall-normal mean fluctuating velocity was introduced to address (1), and a correction term to the DRW similar to the model by Mofakham and Ahmadi (2020) was introduced to address (2). These two modifications were implemented in the PARTICLE model and applied in ANSYS Fluent using user-defined functions (UDFs). These UDFs were based on the model of Longmire (2007).

The resulting prediction of the normalised concentration profile around unity confirmed a more physical interpretation of the particle-fluid interaction when these challenges were addressed. The predicted deposition velocity agrees with earlier experimental results (Papavergos and Hedley 1984; Shimada et al. 1993), numerical results (Gao et al. 2012; Guha 2008; Mofakham and Ahmadi 2020; Tian and Ahmadi 2007), empirical correlations (Fan and Ahmadi 1993; Wood 1981) and Colburn's heat transfer analogy to mass transfer. It is concluded that the established PARTICLE model facilitates improved submicron particle deposition simulations using ANSYS Fluent.

The PARTICLE model was subsequently applied to geothermal conditions of superheated and supercritical water vapour, and deposition velocities of submicron particles were predicted for smooth walls, slightly rough walls and in the presence of a temperature gradient. From these results, the following conclusions can be drawn:

- The submicron particles evaluated are strongly influenced by Brownian motion and the wall-normal turbulent velocity fluctuations in the near-wall region. The influence of these deposition mechanisms and thus the deposition velocity increase with smaller particle sizes.
- Deposition velocities of diffusion-dominated submicron particles are predicted up to one order of magnitude higher than theoretical predictions (Wood 1981) and empirical correlations (Fan and Ahmadi 1993). The discrepancies are possibly related to an overestimation of the particle diffusion.
- The concentration profiles are predicted satisfactorily at geothermal conditions. Improvements and corrections can, however, be made by validating with theoretical predictions from mass transfer.
- Roughness is shown to enhance deposition significantly, even for slightly rough walls, where the dimensionless surface roughness, k^+ , is less than unity. This roughness enhancement is negligible for dimensionless particle relaxation times shorter than 1×10^{-4} .

- Thermophoresis leads to enhanced deposition of submicron particles, but the predicted influence in the PARTICLE model is less than in the correlation of He and Ahmadi (1998). This discrepancy might be related to the overestimated diffusion by the PARTICLE model and subsequent lower near-wall concentration of particles.
- A sensitivity analysis of the discrete random walk model (SI-DRW) revealed high sensitivity to the correction terms to the modelled instantaneous velocity fluctuations.

The experimental investigation aimed to validate the calculated rates of precipitation, agglomeration and deposition of submicron particles by quantifying deposition rates. A calculation procedure was proposed to compare the experimental and numerical results by including a particle size distribution from the numerical model of Bordvik, Næss et al. (2021). As the experimental investigation was preliminary, no conclusions can be drawn from the results. However, the uncertainty analysis on the preliminary results revealed high uncertainties related to the weight measurements. The emphasis was put on increasing the measurement accuracy and perform prolonged experiments to ensure significant deposition.

The PARTICLE model has improved the deposition velocity predictions for diffusion-dominated submicron particles. In addition, the model predictions for bigger particles is excellent, as shown in Figure 9.3, and the model is therefore applicable for a wide range of particle sizes. It is worth noting that other dominant transport and deposition mechanisms, like gravity and lift forces, apply for micron-sized particles. The model is also applicable to more complex geometries like pipe bends and turbine blades. However, validation of the numerical model with results from an experimental investigation is emphasised as a first step. This experimental investigation will possibly reveal the influence of the wall bounding forces for silica deposition from superheated water vapour. Finally, the high computational time related to the short particle relaxation times in the geothermal conditions makes the PARTICLE model most applicable to research. For conventional modelling of submicron particles in simple geometries, the correlation of Fan and Ahmadi (1993) is recommended for estimations of particle deposition.

10.2 Further Work

In the numerical model established in this thesis, the essential transport and deposition mechanisms of diffusion-dominated submicron particles are included. However, the model needs to be validated and possibly tuned in order to achieve desired numerical predictions. The following is recommended for further work:

Numerical Model

- The numerical model should be validated with the measurements from the experimental investigation introduced in this thesis. Possible deviations from the numerical predictions or the empirical correlations might be related to repulsive wall bounding forces. These forces can be corrected by introducing a sticking probability less than unity.
- Validation of the concentration profiles predicted by the numerical model with mass transfer theory is emphasised, e.g. (Kader 1981), as this will consolidate the physical interpretation in the model. Possible discrepancies might lead to a necessary tuning of the correction terms in the implemented discrete random walk (DRW) model, similar to the sensitivity analysis performed in Section 9.2.4.
- The model mean free path employed here is general for gaseous media. The applicability of this model should be further investigated.
- The implemented user-defined functions (UDFs) is not prepared for parallel computing. As the CPU time related to particle tracking is quite significant, preparing the code for parallelisation is recommended for further work.

Wall Bounding Forces

Research on the effect of wall bounding forces on submicron silica particle deposition from superheated steam is emphasised. Estimations on the wall bounding effects would lead to better deposition models. Furthermore, it would facilitate time-dependent and multi-layer deposition models of submicron particles. Such models should also consider the surface roughness of the deposited silica layer and the sticking

probability of a particle.

Complex Geometries

Finally, a broader understanding of deposition mechanisms in more complex geometries is of interest. Therefore, the following is recommended for further work:

- Carry out a two-dimensional channel flow in a 90° bend and simulate deposition of particles in curvilinear motion.

Bibliography

- Andersson, H. I. (1988). *Introduction to turbulence modelling* [Lecture Notes]. NTNU. Trondheim.
- Bergman, T. L., Incropera, F. P., Lavine, A. S. & DeWitt, D. P. (2011). *Introduction to heat transfer*. John Wiley & Sons.
- Bocksell, T. L. & Loth, E. (2001). Random walk models for particle diffusion in free-shear flows. *AIAA journal*, 39(6), 1086–1096.
- Bordvik, S. & Næss, E. (2020). Comparative analysis of energy extraction systems for high temperature, high pressure geothermal steam considering silica precipitation.
- Bordvik, S., Næss, E., Ucar, S. & S. van Erp, T. (2021). Predicting silica deposition from superheated pressurized steam using numerical modelling of nucleation, agglomeration and deposition [In preparation].
- Brown, K. (2011). Thermodynamics and kinetics of silica scaling. *International Workshop on Mineral Scaling*, 25–27.
- Celik, I. B., Ghia, U., Roache, P., Freitas, C., Coleman, H. & Raad, P. (2008). Procedure for Estimation and Reporting of Uncertainty Due to Discretization in CFD Applications [078001]. *Journal of Fluids Engineering*, 130(7).
- Chauhan, V. (2019). *Superheated steam scrubbing and utilization for power generation* (Doctoral dissertation). Reykjavik University, School of Science and Engineering.
- Chen, H. & Patel, V. (1988). Near-wall turbulence models for complex flows including separation. *AIAA journal*, 26(6), 641–648.
- Chen, Q. [Qian] & Ahmadi, G. (1997). Deposition of particles in a turbulent pipe flow. *Journal of Aerosol Science*, 28(5), 789–796.
- Colburn, A. P. (1993). A method of correlating forced convection heat transfer data and a comparison with fluid friction. *Trans Am Inst Chem Engrs*, 29, 174–210.
- Coles, D. & Hirst, E. (1968). Computation of turbulent boundary layers - 1968 afosr-ifp standford conference. *Proc. 1968 conference*. Stanford University.
- Crowe, C. T. (2006). *Multiphase flow handbook*. Taylor & Francis/ CRC Press.
- Crowe, C. T., Drossinos, Y. & Housiadas, C. (2006). Ch. 6. aerosol flows. *Multiphase flow handbook* (pp. 6.1–6.58). CRC Press.
- Crowe, C. T., Sommerfeld, M. & Tsuji, Y. (1998). *Multiphase flows with droplets and particles*. CRC Press.
- D’Auria, F. (2017). *Thermal-hydraulics of water cooled nuclear reactors*. woodhead publishing.
- Davies, C. (1945). Definitive equations for the fluid resistance of spheres. *Proceedings of the Physical Society*, 57(4), 259.
- Dehbi, A. (2008). A cfd model for particle dispersion in turbulent boundary layer flows. *Nuclear engineering and design*, 238(3), 707–715.
- Dreeben, T. D. & Pope, S. B. (1997). Probability density function and reynolds-stress modeling of near-wall turbulent flows. *Physics of Fluids*, 9(1), 154–163.
- Dutkowski, K. (2008). Single phase pressure drop in minichannels. *Transactions IFFM*, 121, 17–32.
- Elghobashi, S. (1994). On predicting particle-laden turbulent flows. *Applied scientific research*, 52(4), 309–329.
- Elghobashi, S. & Abou-Arab, T. (1983). A two-equation turbulence model for two-phase flows. *The Physics of Fluids*, 26(4), 931–938.
- Ellis, P. & Anliker, D. (1981). Geothermal power plant corrosion experience-a global survey. *nace*.

- Equilibar. (2021). *Research series - back pressure regulators* (tech. rep. No. 7) [Online; Accessed: 20-04-2021]. 320 Ruthledge Rd., Fletcher, NC, USA. https://cdn.equilibar.com/PDF/Equilibar-Research_Series-Back_Pressure_Regulators.pdf
- Fan, F.-G. & Ahmadi, G. (1993). A sublayer model for turbulent deposition of particles in vertical ducts with smooth and rough surfaces. *Journal of Aerosol Science*, 24(1), 45–64.
- Fluent, A. (2021a). Ansys fluent customization manual.
- Fluent, A. (2021b). Ansys fluent theory guide.
- Fournier, R. O. & Potter II, R. W. (1982a). An equation correlating the solubility of quartz in water from 25 to 900 c at pressures up to 10,000 bars. *Geochimica et Cosmochimica Acta*, 46(10), 1969–1973.
- Fournier, R. O. & Potter II, R. W. (1982b). Revised and expanded silica (quartz) geothermometer. *Bull., Geotherm. Resour. Counc.(Davis, Calif.):(United States)*, 11(10).
- Fridleifsson, G., Albertsson, A., Bjarnason, J., Gunnarsson, T., Ballzus, C. & Ingason, K. (2003). Part iii: Fluid handling and evaluation. *Iceland deep drilling project, feasibility report* (p. 33). Orkusstofnun.
- Fridriksson, T., Stefánsson, A., Óskarsson, F., Eyjólfsdóttir, E. & Sigurdsson, Ó. (2015). Fluid chemistry scenarios anticipated for iddp-2 to be drilled in reykjanes, iceland. *Proceedings World Geothermal Congress*, 19–25.
- Gao, N., Niu, J., He, Q., Zhu, T. & Wu, J. (2012). Using rans turbulence models and lagrangian approach to predict particle deposition in turbulent channel flows. *Building and Environment*, 48, 206–214.
- Geankoplis, C. J. (2003). *Transport processes and separation process principles* (4th ed.) [p. 475]. Prentice Hall Professional Technical Reference.
- Guha, A. (1997). A unified eulerian theory of turbulent deposition to smooth and rough surfaces. *Journal of Aerosol Science*, 28(8), 1517–1537.
- Guha, A. (2008). Transport and deposition of particles in turbulent and laminar flow. *Annu. Rev. Fluid Mech.*, 40, 311–341.
- He, C. & Ahmadi, G. (1998). Particle deposition with thermophoresis in laminar and turbulent duct flows. *Aerosol science and technology*, 29(6), 525–546.
- Hinze, J. O. (1975). *Turbulence* (2nd ed.). McGraw-Hill.
- Jovanović, J., Ye, Q.-Y. & Durst, F. (1995). Statistical interpretation of the turbulent dissipation rate in wall-bounded flows. *Journal of Fluid Mechanics*, 293, 321–347.
- Kader, B. (1981). Temperature and concentration profiles in fully turbulent boundary layers. *International journal of heat and mass transfer*, 24(9), 1541–1544.
- Kallio, G. & Reeks, M. (1989). A numerical simulation of particle deposition in turbulent boundary layers. *International Journal of Multiphase Flow*, 15(3), 433–446.
- Karlsdóttir, S., Ragnarsdóttir, K., Moller, A., Thorbjornsson, I. & Einarsson, A. (2014). On-site erosion–corrosion testing in superheated geothermal steam. *Geothermics*, 51, 170–181.
- Kays, W. M. & Crawford, M. E. (2011). *Convective heat and mass transfer*. Tata McGraw-Hill Education.
- Kim, J., Moin, P. & Moser, R. (1987). Turbulence statistics in fully developed channel flow at low reynolds number. *Journal of fluid mechanics*, 177, 133–166.
- Kleinhans, U., Wieland, C., Frandsen, F. J. & Spliethoff, H. (2018). Ash formation and deposition in coal and biomass fired combustion systems: Progress and challenges in the field of ash particle sticking and rebound behavior. *Progress in energy and combustion science*, 68, 65–168.
- Kokhanenko, P. (2014). *Hydrodynamics and chemistry of silica scale formation in hydrogeothermal systems* (Doctoral dissertation). University of Canterbury. Mechanical Engineering.
- Lauffer, J. (1953). The structure of turbulence in fully developed pipe flow.
- Launder, B. E. & Shima, N. (1989). Second-moment closure for the near-wall sublayer-development and application. *AIAA journal*, 27(10), 1319–1325.
- Lewis, A., Seckler, M., Kramer, H. & van Rosmalen, G. (2015). *Industrial crystallization: Fundamentals and applications*. Cambridge University Press.
- Li, A. & Ahmadi, G. (1992). Dispersion and deposition of spherical particles from point sources in a turbulent channel flow. *Aerosol science and technology*, 16(4), 209–226.
- Longmire, P. (2007). *Computational fluid dynamics (cfd) simulations of aerosol in a u-shaped steam generator tube* (Doctoral dissertation). Texas A&M University.
- Lu, H. & Lu, L. (2015). Numerical investigation on particle deposition enhancement in duct air flow by ribbed wall. *Building and Environment*, 85, 61–72.

- MacInnes, J. & Bracco, F. (1992). Stochastic particle dispersion modeling and the tracer-particle limit. *Physics of Fluids A: Fluid Dynamics*, 4(12), 2809–2824.
- Mansour, N. N., Kim, J. & Moin, P. (1988). Reynolds-stress and dissipation-rate budgets in a turbulent channel flow. *Journal of fluid mechanics*, 194, 15–44.
- Matida, E. A., Nishino, K. & Torii, K. (2000). Statistical simulation of particle deposition on the wall from turbulent dispersed pipe flow. *International Journal of Heat and Fluid Flow*, 21(4), 389–402.
- Milojević, D. (1990). Lagrangian stochastic-deterministic (lsd) predictions of particle dispersion in turbulence. *Particle & particle systems characterization*, 7(1-4), 181–190.
- Mofakham, A. A. & Ahmadi, G. (2019). Particles dispersion and deposition in inhomogeneous turbulent flows using continuous random walk models. *Physics of Fluids*, 31(8), 083301.
- Mofakham, A. A. & Ahmadi, G. (2020). Improved discrete random walk stochastic model for simulating particle dispersion and deposition in inhomogeneous turbulent flows. *Journal of Fluids Engineering*, 142(10).
- Mofakham, A. A., Ahmadi, G. & McLaughlin, J. (2018). Interactions of flow structure with nano-and micro-particles in turbulent channel flows, 1–4.
- Monin, A. & Yaglom, A. (1971). Statistical fluid mechanics; mechanics of turbulence, 1.
- Moser, R. D., Kim, J. & Mansour, N. N. (1999). Direct numerical simulation of turbulent channel flow up to $Re = 590$. *Physics of fluids*, 11(4), 943–945.
- Mozafari, A. T. J. (2014). *Numerical investigation of marine hydrokinetic turbines: Methodology development for single turbine and small arrays simulation, and application to flume and full-scale referencemodels* (Doctoral dissertation). University of Washington.
- National Energy Authority of Iceland, p. (2020). The iceland deep drilling project [Online]. <https://nea.is/geothermal/the-iceland-deep-drilling-project/>
- Ounis, H. & Ahmadi, G. (1990). Analysis of dispersion of small spherical particles in a random velocity field.
- Ounis, H., Ahmadi, G. & McLaughlin, J. B. (1991). Brownian diffusion of submicrometer particles in the viscous sublayer. *Journal of Colloid and Interface Science*, 143(1), 266–277.
- Ounis, H., Ahmadi, G. & McLaughlin, J. B. (1993). Brownian particle deposition in a directly simulated turbulent channel flow. *Physics of Fluids A: Fluid Dynamics*, 5(6), 1427–1432.
- Papavergos, P. & Hedley, A. (1984). Particle deposition behaviour from turbulent flows. *Chemical engineering research & design*, 62(5), 275–295.
- Paulsen, V. E. S. (2020). *Deposition of silica particles in turbulent superheated steam* (Master's thesis). NTNU.
- PCS, P. C. S. (2021). High pressure dual valve vary-p controller [Online; Accessed: 20-04-2021]. <https://www.pressurecontrolsolutions.nl/products/electronic-pressure-controller/dual-valve-electronic-pressure-controllers/high-pressure-dual-valve-varyp/>
- Perot, B. & Natu, S. (2004). A model for the dissipation rate tensor in inhomogeneous and anisotropic turbulence. *Physics of fluids*, 16(11), 4053–4065.
- Saffman, P. (1965). The lift on a small sphere in a slow shear flow. *Journal of fluid mechanics*, 22(2), 385–400.
- Saffman, P. (1968). Corrigendum to 'the lift on a small sphere in a slow shear flow'. *J. Fluid Mech.*, 31, 624.
- Sato, Y. & Yamamoto, K. (1987). Lagrangian measurement of fluid-particle motion in an isotropic turbulent field. *Journal of fluid mechanics*, 175, 183–199.
- Schiller, L. & Nauman, A. (1933). Über die grundlegenden berechnungen bei der schwerkraftaufbereitung. *Z. Vereines Deutscher Inge.*, 77, 318–321.
- Shimada, M., Okuyama, K. & Asai, M. (1993). Deposition of submicron aerosol particles in turbulent and transitional flow. *AIChE journal*, 39(1), 17–26.
- Snyder, W. H. & Lumley, J. (1971). Some measurements of particle velocity autocorrelation functions in a turbulent flow. *Journal of Fluid Mechanics*, 48(1), 41–71.
- Spalding, D. B. (1961). A single formula for the law of the wall. *Journal of Applied Mechanics*, 28, 455–457.
- Stordal, T. V. (2020). *Particle deposition from geothermal supercritical steam* (Project work). NTNU.

- Strutt, H. C. & Lightstone, M. (2006). Analysis of tracer particle migration in inhomogeneous turbulence. *International journal of heat and mass transfer*, 49(15-16), 2557–2566.
- Sveningsson, A. (2003). *Analysis of the performance of different- v_2 - f turbulence models in a stator vane passage flow* (Doctoral dissertation). Chalmers University of Technology.
- Talbot, L., Cheng, R., Schefer, R. & Willis, D. (1980). Thermophoresis of particles in a heated boundary layer. *Journal of fluid mechanics*, 101(4), 737–758.
- Tandberg, A. R. (2017). *Gas-side fouling of heat exchanger surfaces* (Master's thesis). NTNU.
- Tian, L. & Ahmadi, G. (2007). Particle deposition in turbulent duct flows—comparisons of different model predictions. *Journal of Aerosol Science*, 38(4), 377–397.
- van den Heuvel, D. B., Gunnlaugsson, E., Gunnarsson, I., Stawski, T. M., Peacock, C. L. & Benning, L. G. (2018). Understanding amorphous silica scaling under well-constrained conditions inside geothermal pipelines. *Geothermics*, 76, 231–241.
- von Hirtz, P. (2016). 16 - silica scale control in geothermal plants—historical perspective and current technology1. In R. DiPippo (Ed.), *Geothermal power generation* (pp. 443–476). Woodhead Publishing. <https://www.sciencedirect.com/science/article/pii/B9780081003374000164>
- Wagner, W. & Kretzschmar, H.-J. (2008). Iapws industrial formulation 1997 for the thermodynamic properties of water and steam. *International steam tables: properties of water and steam based on the industrial formulation IAPWS-IF97*, 7–150.
- Wheeler, A. J. & Ganji, A. R. (2010). *Introduction to engineering experimentation* (Vol. 199). Prentice Hall New Jersey.
- White, F. M. (2019). *Viscous fluid flow* (3rd). McGraw-Hill Education.
- Wilson, J., Thurtell, G. & Kidd, G. (1981). Numerical simulation of particle trajectories in inhomogeneous turbulence, ii: Systems with variable turbulent velocity scale. *Boundary-layer meteorology*, 21(4), 423–441.
- Wood, N. (1981). A simple method for the calculation of turbulent deposition to smooth and rough surfaces. *Journal of aerosol Science*, 12(3), 275–290.
- Young, J. B. (2011). Thermophoresis of a spherical particle: Reassessment, clarification, and new analysis. *Aerosol Science and Technology*, 45(8), 927–948.
- Zhang, Z. & Chen, Q. (2009). Prediction of particle deposition onto indoor surfaces by cfd with a modified lagrangian method. *Atmospheric Environment*, 43(2), 319–328.

A | Experiments

A.1 Experimental Procedure

The experimental procedure when performing the measurements consists of preparations, startup, running the test, shut down, and lastly, disassembly and measurement. The different procedures are listed below:

Preparations

1. The autoclave was prepared with distilled water with a sufficient amount of silica particles ($d_p = 21 \mu\text{m}$) to be dissolved and heated up. At supercritical conditions, the pH in the water is about neutral.
2. The rig was cleaned for silica deposits with hot water and a basic solution ($pH > 9$) if necessary.
3. The water pump to the autoclave, the pressure control system and liquid water for the condenser were made ready.
4. Low-pressure leakage test with helium was performed to ensure sealed connections.
5. The electrical heaters were started, and the system was allowed to heat until the Equilibar was fully heated. The system was typically heated for half an hour before initiation.

Startup

1. The manual closing valve was carefully opened, and the desired pressure was set by the pressure control system.
2. The manual control valves at the outlet were slowly opened until the desired flow rate was achieved. The flow rate was measured at the pump controller upstream of the autoclave.

Running Test

The tests were run at steady state for as long as possible. During the tests, the following were monitored

- Pressures in the rig, autoclave and the pressure controller to ensure steady behaviour.
- Temperature in the heated box and in the autoclave.

The tests were run until the water pump needed refilling. Then the following procedure was performed:

1. The manual control valves at the outlet was closed.
2. The manual closing valve downstream the autoclave was closed.
3. The pump was detached, refilled and attached.
4. The manual closing valve downstream the autoclave was opened.
5. The manual control valves at the outlet were slowly opened until the desired flow rate was achieved.

Shut Down

1. The manual closing valve downstream the autoclave was close, and the test sections were depressurised to ambient conditions.
2. The system was carefully purged with nitrogen for two minutes to remove the remaining steam.
3. The heaters were turned off, and the system was allowed to cool for one hour.

Disassembly and Measurement

1. The Equilibar and the two test sections were carefully removed and weighed.
2. The condensate container was weighted to estimate the average flow rate.

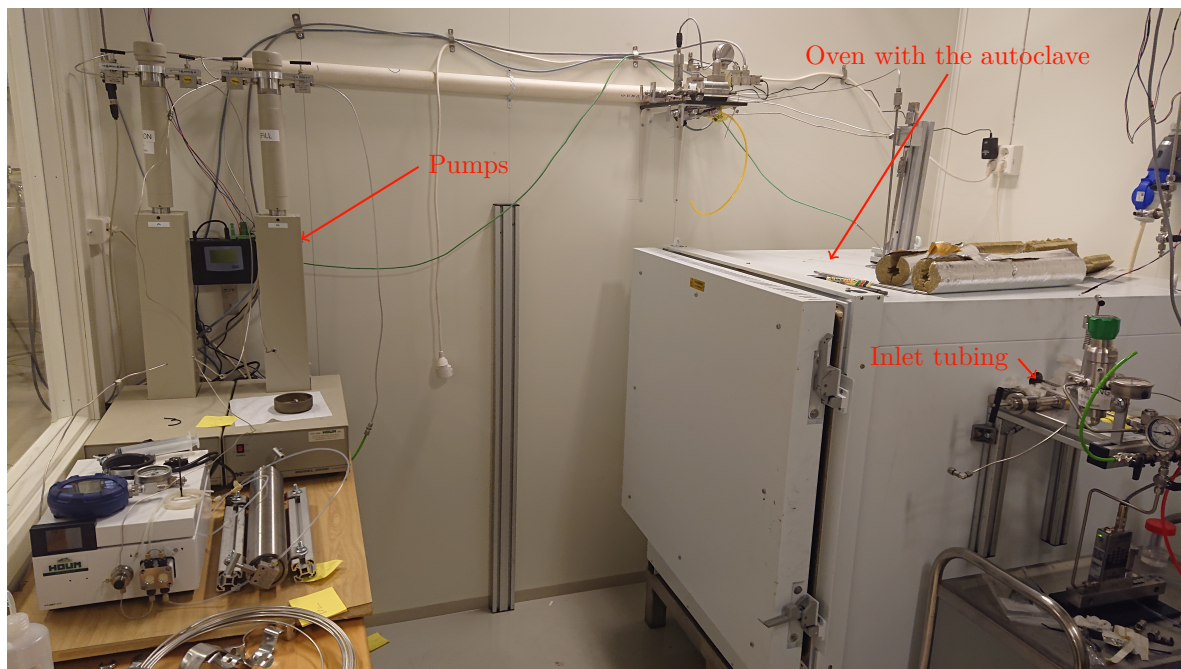


Figure A.1: Picture of the rig at IFE.

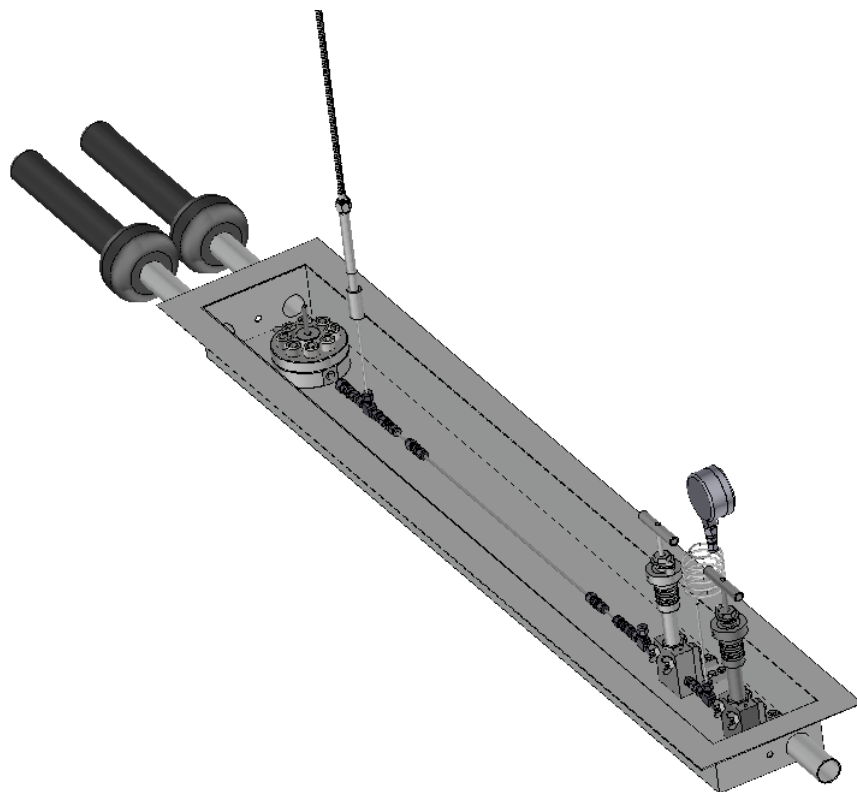


Figure A.2: Three-dimensional model of the rig.

B | Fluent Macros

The PARTICLE model consists of user-defined functions (UDFs) that are implemented in ANSYS Fluent with the use of Fluent macros. In the present study, the macros for the Discrete Phase Model (DPM) are included in one code. The Fluent macros employed in Code listing B.1 are

- DEFINE_DPM_INJECTION_INIT for particle initiation
- DEFINE_DPM_BODY_FORCE for the Brownian force
- DEFINE_DPM_BC for boundary conditions
- DEFINE_DPM_DRAG for drag and turbulent fluctuations
- DEFINE_DPM_SCALAR_UPDATE for updating and initiating particle scalars e.g. location
- DEFINE_DPM_TIMESTEP for the particle time step
- DEFINE_ON_DEMAND for managing user-defined memory (UDM)

For further details on the code, the reader is referred to the comments in the code and descriptions in the master's thesis. Again, it is emphasised that the groundwork and basis for the implemented code is taken from Longmire (2007).

Code listing B.1: PARTICLE model: UDFs

```
1
2 /*
3 *** The implemented C-code below includes several UDF-macros:
4 * - DEFINE_DPM_DRAG(dpm_stochastic_drag,Re,p) - model for particle drag and the user defined
5 * turbulent dispersion (improved-DRW)
6 * - DEFINE_DPM_BODY_FORCE(brownian_forceF,p,i) - model for the Brownian motion
7 * - DEFINE_DPM_BC(bc_escape,p,t,f,f_normal,dim) - user-defined boundary condition for
8 * generating concentration profiles
9 * - DEFINE_DPM_BC(bc_capture, p, t, f, f_normal, dim) - user-defined boundary condition at
10 * the walls for particle deposition
11 * - DEFINE_DPM_INJECTION_INIT(init_particles, I) - user-defined function for initiating
12 * the particles with the velocity and temperature similar to the fluid flow at the
13 * particle location.
14 *
15 * For these functions to work appropriately, UDM locations and particle scalars need to be
16 * defined. In addition, UDF-macros for e.g. updating these scalars and clear the UDMs after
17 * data extraction are necessities. These are:
18 * - DEFINE_ON_DEMAND(set_udm_fluid) - or similar. Clears the UDM data and generates the fluid
19 * udms.
20 * - DEFINE_DPM_SCALAR_UPDATE(dpm_sc_interact,cell,thread,initialize,p) - updates and initialises
21 * the particle scalars.
22 * The particle time step in the DPM can also be controlled by applying the following:
23 * - DEFINE_DPM_TIMESTEP(dpm_ts_by_eddy_time,p, dt
24 *
25 * Global functions are included to simplify the code. These are
26 * - get_rms_vel_fluc - returns the rms velocities
27 * - get_yplus_particle - returns the yplus-location of the particle
28 * - get_Cc - returns the Cunningham correction for the particle
29 * - get_correction - returns the value of the correction terms in the improved-DRW
30 * - get_tl_plus - returns the dimensionless Lagrangian time scale, T_L+
31 * - get_aborted - returns number of aborted particles if roughness or the new model for the wall
32 * boundary condition are implemented
33 * As most of these global functions have been implemented in the different Fluent macros,
34 * the c-code should not be splitted.
35 *
36 *** The code has certain limitations:
37 * - does not work with accuracy control of particle tracks
38 * - stochastic tracking is activated for ALL defined injections
39 * - does not work for parallel processing (but can be implemented)
40 *
```

```

41 *
42 *** DEFINE_DPM_DRAG(dpm_stochastic_drag,Re,p) and the implemented improved-DRW model:
43 * Based on the defined y_tresh (here, 200), the particle is located...
44 * - inside the boundary layer and do_wall_stoch is employed
45 * - outside the boundary layer and do_stochastics is employed
46 *
47 * The function do_stochastics is implemented similar to the default conventional-DRW in Fluent
48 *
49 * In the function do_wall_stoch, the improved-DRW is implemented. Here, empirical formulations
50 * for the Lagrangian time scale and the wall-normal fluctuating velocity is included, updated
51 * and modified.
52 *
53 * For further explanations, see comments in the code or explanations/theory in the Master's thesis
54 * by Tarjei Vefring Stordal (2020). The groundwork and basis for the implemented code is taken from
55 *
56 * Longmire, P. (2007). Computational fluid dynamics (CFD) simulations of aerosol in a U-shaped steam
57 * generator tube (Doctoral dissertation, Texas A & M University).
58 *
59 *** Usage Manual:
60 * - download Visual Studio
61 * - open Fluent via the cross-tool command window, with one processor
62 * - compile and load the udfs
63 * - activate drag force udf (deactivate the default DRW)
64 * - activate Brownian motion udf
65 * - activate time step routines
66 * - for walls and the outlet activate DPM boundary condition
67 * - activate 13 particle scalars and hook SCALAR_UPDATE function
68 * - hook DEFINE_INIT function
69 * - activate 7 UDM locations
70 * - after calc. of flow field execute the set_udm function for setting
71 * Y_plus values for particles in wall nearest cell (coarse grid), or
72 * if the sublayer is resolved, choose set_udm_finegrid (may take a long time to execute)
73 * - finally perform particle tracking with the DPM. The DPM_DRAG function evaluates the particle Y_plus
74 * and chooses the appropriate time scale for eddy interaction and instantaneous turbulence
75 */
76
77 #include "udf.h"
78 #include "dpm.h"
79 #include "cxsurf.h" /* for screen output with CX_Message(...) */
80 #include "surf.h"
81 #include "sg.h"
82 #include "mem.h"
83 #include "metric.h"
84 #include "random.h"
85
86 #define C_MU_FACTOR(I) (I->time_scale_constant)
87 #define C_MU 0.09
88 #define MY_WALL_SHEAR_X(f,t) F_STORAGE_R_N3V(f,t,SV_WALL_SHEAR)[0] /*FORCES!! divide by face area */
89 #define MY_WALL_SHEAR_Y(f,t) F_STORAGE_R_N3V(f,t,SV_WALL_SHEAR)[1]
90 #define MY_WALL_SHEAR_Z(f,t) F_STORAGE_R_N3V(f,t,SV_WALL_SHEAR)[2]
91 #define THERMO 0
92 #define INTERPOLATION 1
93 #define DEBUGGER 0
94 #define KB 1.38e-23 /*Stephan-Boltzmann constant*/
95 #define PI 3.1415926
96
97 cxboolean dns = TRUE; /* Boundary layer model: TRUE: Eq. 3.20. FALSE Eq. 3.19 */
98 cxboolean dns_correction = TRUE; /* Correction term in improved-DRW: TRUE: Eq. 3.20. FALSE Eq. 3.19 */
99 cxboolean random_eddy_lifetime = FALSE;
100 cxboolean air = FALSE; /* TRUE if the fluid medium is air */
101 cxboolean roughness = FALSE; /* TRUE if a slightly rough wall is considered (k+ < 1.5) */
102 static real op_pressure = 50e5; /* Operational pressure in the system, here 50 bar */
103
104 cxboolean do_stochastics = TRUE;
105 cxboolean do_wall_stoch = FALSE;
106
107 /* For message printing */
108 int update_interval = 100001;
109 int update_interval_up = 1000000;
110 int update_interval_old = 5000000
111 static int msg_count = 0; /*count of messages printed*/
112 static int aborted = 0; /*# aborted particles with the roughness model, used for output msg*/
113

```



```

114 static real yplus_thresh = 200.0;          /* max yplus for wall functions in this UDF*/
115 static real dt_min = 1.8e-7;             /* smallest time step = 1/5 of smallest eddy lifetime*/
116 static real te_min = 8.9e-07;           /* smallest eddy lifetime, tau_e*/
117
118 /* global function declarations */
119 static real get_yplus_particle(cell_t c, Thread *t, real *pp); /*yplus at particle position*/
120 static real get_tl_plus(real);
121 static real get_Cc(real,real,real,real);
122 static real get_aborted();
123 static real get_correction(real, real, real, real, real, real, real, cell_t c0, Thread *t0);
124 #if dns
125 static void get_rms_vel_fluc(real,real,real*,real*,real*,real*,cphase_state_t*,
126 cell_t c0,Thread *t0,cxboolean,real);
127 #else
128 static void get_rms_vel_fluc(real, real, real*, cell_t c0, Thread* t0);
129 #endif
130 /*UDMs*/
131 enum udm_names{
132 Y_PLUS,
133 TAU_WALL,
134 N_VEC_X,
135 N_VEC_Y,
136 #if RP_3D
137 N_VEC_Z,
138 #endif
139 FACE_X,
140 FACE_Y,
141 #if RP_3D
142 FACE_Z,
143 #endif
144 WALL_HIT,
145 DEP
146 };
147 /*particle scalars*/
148 enum p_names{
149 E_PLUS,
150 T_EDDY,
151 Y_PLUS_P,
152 LAMBDA1,
153 LAMBDA2,
154 LAMBDA3,
155 N_EDDY,
156 EDDY_DIR,
157 MOD
158 };
159 /*****
160 real get_tl_plus(real yplus)
161 {
162 real TL_plus = 1.0;
163
164 if (yplus>5.0 && yplus<yplus_thresh)
165 {
166 TL_plus = 7.122 + 0.5731*yplus - 0.00129*yplus*yplus;
167 }
168 else if (yplus <= 5.0)
169 {
170 TL_plus = 10; /* yplus*2 */
171 }
172 else
173 {
174 CX_Message("TL_plus_error:\n",TL_plus);
175 }
176 return TL_plus;
177 }
178
179 /*****
180
181
182 #if dns
183 /* Boundary layer model with Eq. 3.20*/
184 void get_rms_vel_fluc(real yplus, real vel_fric, real *Vprime_vec, real *I, real *J, real *K,
185 cphase_state_t* c,cell_t c0, Thread *t0, cxboolean new_eddy, real dir)
186 {

```

```

187 real I_mag;
188 /*NV_V(pp, =, p->state.pos); position of particle, x,y,z-coord. now stored in pp*/
189 Vprime_vec[0] = 0.4*vel_fric*yplus/(1.+0.0239*pow(yplus,1.496));
190 Vprime_vec[1] = 0.0116*vel_fric*yplus*yplus/(1.+0.203*yplus+0.0014*pow(yplus,2.421));
191 Vprime_vec[2] = 0.19*vel_fric*yplus/(1.+0.0361*pow(yplus,1.322));
192 /* calc. anisotropic local fluctuation velocities ...*/
193 /* and assign the local coordinate system vectors ... */
194 I[0] = c->V[0];
195 I[1] = c->V[1];
196 #if RP_3D
197 I[2] = c->V[2];
198 #endif
199 /* Normalize I_mag*/
200 I_mag = NV_MAG(I);
201 NV_S(I,/=,I_mag);
202
203 if (new_eddy)
204 {
205 J[0] = C_UDMI(c0,t0,N_VEC_X); /* This is 0 everywhere */
206 J[1] = C_UDMI(c0,t0,N_VEC_Y); /* This is 1 for y > 0 and -1 for y < 0. */
207 #if RP_3D
208 J[2] = C_UDMI(c0,t0,N_VEC_Z);
209 #endif
210 }
211 else
212 {
213 J[0] = 0.;
214 J[1] = dir;
215 #if RP_3D
216 J[2] = 0.;
217 #endif
218 }
219
220
221
222 NV_CROSS(K,I,J); /* K = I x J */
223 #if DEBUGGER
224 CX_Message("I0=%f,I1=%f,I2=%f\n",I[0],I[1],I[2]);
225 CX_Message("J0=%f,J1=%f,J2=%f\n",J[0],J[1],J[2]);
226 CX_Message("K0=%f,K1=%f,K2=%f\n",K[0],K[1],K[2]);
227 #endif
228 /* ... finally transform everything back into cartesian coordinates */
229 NV_S(I,*,Vprime_vec[0]); /* x-component stored in I*/
230 NV_S(J,*,Vprime_vec[1]); /* y-component stored in J*/
231 NV_S(K,*,Vprime_vec[2]); /* z-component stored in K*/
232 /*re-assign fluctuation velocities*/
233 Vprime_vec[0] = I[0] + J[0] + K[0];
234 Vprime_vec[1] = I[1] + J[1] + K[1];
235 Vprime_vec[2] = I[2] + J[2] + K[2];
236 #if 0
237 Vprime_vec[0] = 0.*vel_fric;
238 Vprime_vec[1] = 0.*vel_fric;
239 Vprime_vec[2] = 0.*vel_fric;
240 #endif
241 }
242
243
244
245 #else
246 /* Boundary layer model with Eq. 3.19 */
247 void get_rms_vel_fluc(real yplus, real vel_fric, real *Vprime_vec, cell_t c0, Thread *t0)
248 {
249
250 real chc11=0.;
251 real chc22=0.;
252 real chc33=0.;
253 chc11 = sqrt(C_RUU(c0,t0));
254 chc22 = sqrt(C_RVV(c0,t0)); /*sqrt(MAX(SMALL, C_RVV(c0,t0)chc12*chc12) -*/
255 chc33 = sqrt(C_RWW(c0,t0));
256
257 Vprime_vec[0] = chc11;
258 Vprime_vec[1] = chc22;
259 Vprime_vec[2] = chc33;

```

```

260
261 if (yplus <= 4)
262 {
263     real A = 0.008;
264     Vprime_vec[1] = A*pow(yplus,2.)*vel_fric;
265 }
266 }
267 #endif
268
269 /* function to determine a particle's dimensionless wall distance */
270 /* This function fits well with my estimates for y_plus: Check OK */
271 real get_yplus_particle(cell_t c,Thread *t,real *pp)
272 {
273     real Y_plus_p,Y_p;
274     real p_dist[ND_ND];
275     real A[ND_ND];
276     real Xf[ND_ND];
277     if(C_UDMI(c,t,Y_PLUS) < 0.0)
278     return -1.0;
279     A[0] = C_UDMI(c,t,N_VEC_X);
280     A[1] = C_UDMI(c,t,N_VEC_Y);
281     #if RP_3D
282     A[2] = C_UDMI(c,t,N_VEC_Z);
283     #endif
284     Xf[0] = C_UDMI(c,t,FACE_X);
285     Xf[1] = C_UDMI(c,t,FACE_Y);
286     #if RP_3D
287     Xf[2] = C_UDMI(c,t,FACE_Z);
288     #endif
289     NV_VV(p_dist,=,Xf,-,pp);
290     Y_p = fabs(NV_DOT(A,p_dist));
291     Y_plus_p = Y_p*sqrt(C_UDMI(c,t,TAU_WALL)*C_R(c,t))/C_MU_L(c,t);
292     return Y_plus_p;
293 }
294
295
296 real get_Cc(real P, real T, real Dp, real mu)
297 {
298     /* Defining variables to be used*/
299     real lam,Cc,a,b,R,p_abs;
300     R = 461.526; /*From AIPWS*/
301     p_abs = P + op_pressure;
302     a = pow(PI*R*T/2,0.5);
303     b = mu/(p_abs);
304     lam = a*b;
305
306     #if air
307     /* Extract needed variables from Fluent*/
308     lam_ref=0.0664*pow(10.0,-6.0);
309
310     /* lam = mean free path*/
311     a=(101.0e3)/(P+101.0e3);
312     b=T/293.0;
313     d=(1.0+110.0/293.0)/(1.0+110.0/T);
314     lam=lam_ref*a*b*d;
315     #else
316
317     #endif
318
319     /* Cc = Cunningham correction factor*/
320     Cc=1.0+lam/Dp*(2.514+0.8*exp(-0.55*Dp/lam));
321
322     return Cc;
323 }
324
325 real get_aborted()
326 {
327     return aborted+= 1;
328 }
329
330
331 real get_correction(real yplus, real vel_fric, real Stk, real nu, real TL, real dt, real dir,
332 cell_t c0, Thread *t0)

```

```

333 {
334     real v = sqrt(C_RVV(c0,t0));
335
336
337 if (yplus <= 4)
338 {
339     real A = 0.008;
340     v = A*pow(yplus,2.)*vel_fric;
341 }
342     #if dns_correction
343     real v = 0.0116*vel_fric*yplus*yplus/(1.+0.203*yplus+0.0014*pow(yplus,2.421));
344     #endif
345
346 real dvdy = ((11836.7*yplus + 1201.43*pow(yplus,2.) - 3.48829*pow(yplus,3.421))/
347 (pow(714.286 + 145*yplus + pow(yplus,2.421),2.))*pow(vel_fric,2.)/nu;
348 real dTLdy = 0.;
349 if (yplus > 5) dTLdy = (0.5731-0.00258*yplus)/vel_fric;
350
351 real corr_term = (1/(1+Stk))*(v*dvdy-(pow(v,2.)/TL)*dTLdy)*dt; /* v*dvdy-(pow(v,2.)/TL)*dTLdy */
352 /* The direction away from the wall has to be taken into account */
353
354 corr_term *= dir; /* Direction of the correction-term */
355 return corr_term;
356 }
357
358 /* distribute user RP variables */
359 DEFINE_ADJUST(get_rp_variables, domain)
360 {
361     #if !RP_NODE
362     update_interval = (int)RP_Get_Real("update_thermo");
363     update_interval_old = (int)RP_Get_Real("update_old");
364     update_interval_up = (int)RP_Get_Real("update_new");
365     yplus_thresh = RP_Get_Real("yplus_threshold");
366     dt_min = RP_Get_Real("delta_t_min");
367     te_min = RP_Get_Real("t_eddy_min");
368     #endif
369     host_to_node_int_1(update_interval);
370     host_to_node_int_1(update_interval_old);
371     host_to_node_int_1(update_interval_up);
372     host_to_node_real_1(yplus_thresh);
373     host_to_node_real_1(dt_min);
374     host_to_node_real_1(te_min);
375 }
376 /* distribute user RP variables */
377 DEFINE_ON_DEMAND(eod_rp_variables)
378 {
379     #if !RP_NODE
380     update_interval = (int)RP_Get_Real("update_thermo");
381     update_interval_old = (int)RP_Get_Real("update_old");
382     update_interval_up = (int)RP_Get_Real("update_new");
383     yplus_thresh = RP_Get_Real("yplus_threshold");
384     dt_min = RP_Get_Real("delta_t_min");
385     te_min = RP_Get_Real("t_eddy_min");
386     #endif
387
388     host_to_node_int_1(update_interval);
389     host_to_node_int_1(update_interval_old);
390     host_to_node_int_1(update_interval_up);
391     host_to_node_real_1(yplus_thresh);
392     host_to_node_real_1(dt_min);
393     host_to_node_real_1(te_min);
394 }
395
396
397 /* set user defined memories with global search method (very slow) */
398 DEFINE_ON_DEMAND(set_udm_domain)
399 {
400     Domain *d;
401     face_t f, f0;
402     cell_t c, c0;
403     Thread *ft, *ft0, *ct, *ct0;
404     real ds;
405     real A_by_es ;

```

```

406 real es[ND_ND] ;
407 real dr0[ND_ND] ;
408 real A[ND_ND] ;
409 real Xf[ND_ND] ;
410 real Xc[ND_ND] ;
411 real tau_wall[ND_ND] ;
412 real wall_dist = 1.0e+20;
413 real face_dist[ND_ND];
414 real As;
415 /* *****/
416 d=Get_Domain(1);
417 thread_loop_c(ct,d)
418 {
419   begin_c_loop(c,ct)
420   {
421     wall_dist = 1.0e+20;
422     C_CENTROID(Xc,c,ct);
423     thread_loop_f(ft, d)/* loops over all face threads in a domain*/
424     {
425       if(THREAD_TYPE(ft) == THREAD_F_WALL) /* check if it is a wall */
426       {
427         begin_f_loop(f, ft) /* loops over faces in a face thread */
428         {
429           F_CENTROID(Xf,f,ft);
430           NV_VV(face_dist,=,Xc,-,Xf);
431           if (NV_MAG(face_dist)<wall_dist)
432           {
433             f0 = f;
434             ft0 = ft;
435             wall_dist = NV_MAG(face_dist);
436           }}
437         end_f_loop(f, ft)
438         if (msg_count%1000==0){
439           CX_Message("%d_Cell_Thread_ID=%d\n",msg_count,THREAD_ID(ct));
440           CX_Message("wall_dist.=%f\n",wall_dist);}
441         msg_count++;
442       }
443     }
444     if(NNULLP(THREAD_STORAGE(ft0,SV_WALL_SHEAR)))
445     {
446       c0 = F_C0(f0,ft0);
447       ct0 = THREAD_T0(ft0);
448       F_CENTROID(Xf,f0,ft0);
449       NV_VV(face_dist,=,Xc,-,Xf);
450       BOUNDARY_FACE_GEOMETRY(f0,ft0,A,ds,es,A_by_es,dr0);
451       As= NV_MAG(A);
452       NV_VS(tau_wall,=,F_STORAGE_R_N3V(f0,ft0,SV_WALL_SHEAR) , / , As);
453       NV_VS(A,=,A , / , As) ;
454       C_UDMI(c,ct,TAU_WALL) = NV_MAG(tau_wall);
455       wall_dist = fabs(NV_DOT(A,face_dist));
456       C_UDMI(c,ct,Y_PLUS) = wall_dist*sqrt(NV_MAG(tau_wall)*C_R(c,ct))/C_MU_L(c,ct);
457       C_UDMI(c,ct,N_VEC_X) = -A[0];
458       C_UDMI(c,ct,N_VEC_Y) = -A[1];
459       #if RP_3D
460       C_UDMI(c,ct,N_VEC_Z) = -A[2];
461       #endif
462       C_UDMI(c,ct,FACE_X) = Xf[0];
463       C_UDMI(c,ct,FACE_Y) = Xf[1];
464       #if RP_3D
465       C_UDMI(c,ct,FACE_Z) = Xf[2];
466       #endif
467
468       C_UDMI(c,ct,WALL_HIT) = 0.0;
469       C_UDMI(c,ct,DEP) = 0.0;
470     }
471     else
472     {
473       C_UDMI(c,ct,TAU_WALL) = -1.0;
474       C_UDMI(c,ct,Y_PLUS) = -1.0;
475     }
476   }
477   end_c_loop(c,ct)
478 }

```

```

479 }
480 /* set user defined memories only in near wall cell (fastest method) */
481 DEFINE_ON_DEMAND(set_udm_wall)
482 {
483 Domain *d;
484 face_t f;
485 cell_t c;
486 Thread *ft,*ct;
487 real ds;
488 real A_by_es ;
489 real es[ND_ND] ;
490 real dr0[ND_ND] ;
491 real A[ND_ND] ;
492 real Xf[ND_ND] ;
493 real Xc[ND_ND] ;
494 real tau_wall[ND_ND] ;
495 real wall_dist;
496 real As;
497 /* *****/
498 d=Get_Domain(1);
499 thread_loop_f(ft, d)/* loops over all face threads in a domain*/
500 {
501 begin_f_loop(f, ft) /* loops over faces in a face thread */
502 {
503 c = F_C0(f, ft);
504 ct = THREAD_T0(ft);
505 C_CENTROID(Xc,c,ct);
506 F_CENTROID(Xf,f,ft);
507 BOUNDARY_FACE_GEOMETRY(f,ft,A,ds,es,A_by_es,dr0);
508 As= NV_MAG(A);
509 if(THREAD_TYPE(ft) == THREAD_F_WALL) /* check if it is a wall */
510 {
511 if(NNULLP(THREAD_STORAGE(ft,SV_WALL_SHEAR)))
512 {
513 NV_VS(tau_wall,=,F_STORAGE_R_N3V(f,ft,SV_WALL_SHEAR) , / , As);
514 C_UDMI(c,ct,TAU_WALL) = NV_MAG(tau_wall);
515 NV_VS(A,=,A , / , As);
516 wall_dist = fabs(NV_DOT(A,dr0));
517 C_UDMI(c,ct,Y_PLUS) = wall_dist*sqrt(NV_MAG(tau_wall)*C_R(c,ct))/C_MU_L(c,ct);
518 }
519 else
520 {
521 C_UDMI(c,ct,TAU_WALL) = -1.0;
522 C_UDMI(c,ct,Y_PLUS) = -1.0;
523 }
524
525 C_UDMI(c,ct,N_VEC_X) = -A[0];
526 C_UDMI(c,ct,N_VEC_Y) = -A[1];
527 #if RP_3D
528 C_UDMI(c,ct,N_VEC_Z) = -A[2];
529 #endif
530 C_UDMI(c,ct,FACE_X) = Xf[0];
531 C_UDMI(c,ct,FACE_Y) = Xf[1];
532 #if RP_3D
533 C_UDMI(c,ct,FACE_Z) = Xf[2];
534 #endif
535
536 C_UDMI(c,ct,WALL_HIT) = 0.;
537 C_UDMI(c,ct,DEP) = 0.0;
538 }}
539 end_f_loop(f, ft)
540 }
541 }
542 /* set user defined memories zone by zone (recommended over global) */
543 DEFINE_ON_DEMAND(set_udm_fluid)
544 {
545 Domain *d;
546 face_t f,face;
547 cell_t c;
548 Thread *ft,*ct;
549 real ds;
550 real A_by_es ;
551 real es[ND_ND] ;

```

```

552 real dr0[ND_ND] ;
553 real A[ND_ND] ;
554 real Xf[ND_ND] ;
555 real Xpos[ND_ND] ;
556 real Xc[ND_ND] ;
557 real face_dist[ND_ND];
558 real tau_wall[ND_ND] ;
559 real wall_dist = 1.0e+20;
560 real As;
561 /* *****/
562 d=Get_Domain(1);
563 thread_loop_f(ft, d)/* loops over all face threads in a domain*/
564 {
565   if(THREAD_TYPE(ft) == THREAD_F_WALL) /* check if it is a wall */
566   {
567     CX_Message("Wall_Thread_ID=%d\n",THREAD_ID(ft));
568     ct = THREAD_T0(ft);
569     if(FLUID_THREAD_P(ct))
570     {
571       begin_c_loop(c,ct)
572       {
573         C_CENTROID(Xc,c,ct);
574         wall_dist = 1.0e+20;
575         begin_f_loop(f, ft) /* loops over faces in a face thread */
576         {
577           F_CENTROID(Xf,f,ft);
578           NV_VV(face_dist,=,Xc,-,Xf);
579           if (NV_MAG(face_dist)<wall_dist)
580           {
581             face = f;
582             wall_dist = NV_MAG(face_dist);
583             F_CENTROID(Xpos,f,ft);
584           }
585         }
586         end_f_loop(f, ft)
587         if (msg_count%1000==0){
588           CX_Message("%d_Cell_Thread_ID=%d\n",msg_count,THREAD_ID(ct));
589           CX_Message("wall_dist.=%f\n",wall_dist);}
590         msg_count++;
591         BOUNDARY_FACE_GEOMETRY(face, ft,A,ds,es,A_by_es,dr0);
592         As= NV_MAG(A);
593         if(NNULLP(THREAD_STORAGE(ft,SV_WALL_SHEAR)))
594         {
595           NV_VS(tau_wall,=,F_STORAGE_R_N3V(face,ft,SV_WALL_SHEAR) , / , As);
596           C_UDMI(c,ct,TAU_WALL) = NV_MAG(tau_wall);
597           NV_VS(A,=,A , / , As);
598           C_UDMI(c,ct,Y_PLUS) = wall_dist*sqrt(NV_MAG(tau_wall)*C_R(c,ct))/C_MU_L(c,ct);
599           C_UDMI(c,ct,N_VEC_X) = -A[0];
600           C_UDMI(c,ct,N_VEC_Y) = -A[1];
601           #if RP_3D
602           C_UDMI(c,ct,N_VEC_Z) = -A[2];
603           #endif
604           C_UDMI(c,ct,FACE_X) = Xpos[0];
605           C_UDMI(c,ct,FACE_Y) = Xpos[1];
606           #if RP_3D
607           C_UDMI(c,ct,FACE_Z) = Xpos[2];
608           #endif
609         }
610         else
611         {
612           C_UDMI(c,ct,TAU_WALL) = -1.0;
613           C_UDMI(c,ct,Y_PLUS) = -1.0;
614         }}
615         end_c_loop(c,ct)
616       }
617     }
618   }
619 }
620
621 /* Set the deposition and concentration UDMs to zero */
622 DEFINE_ON_DEMAND(eod_udm_zero)
623 {
624   cell_t c;

```

```

625 Thread *ct;
626 Domain *d;
627 d = Get_Domain(1);
628 /* loop over all cell threads in the domain */
629 thread_loop_c(ct,d)
630 {
631 /* loop over all cells */
632 begin_c_loop_all(c,ct)
633 {
634 C_UDMI(c,ct,WALL_HIT) = 0.;
635 C_UDMI(c,ct,DEP) = 0.;
636 }
637 end_c_loop_all(c,ct)
638 }
639 }
640
641 /* initialize UDMs on solver init */
642 DEFINE_INIT(udm_init_func,d)
643 {
644 cell_t c;
645 Thread *ct;
646 if
647 (NULLP(user_particle_vars)) Init_User_Particle_Vars();
648 /* loop over all cell threads in the domain */
649 thread_loop_c(ct,d)
650 {
651 /* loop over all cells */
652 begin_c_loop_all(c,ct)
653 {
654 C_UDMI(c,ct,TAU_WALL) = -1.0;
655 C_UDMI(c,ct,Y_PLUS) = -1.0;
656 C_UDMI(c,ct,N_VEC_X) = 0.;
657 C_UDMI(c,ct,N_VEC_Y) = 0.;
658 #if RP_3D
659 C_UDMI(c,ct,N_VEC_Z) = 0.;
660 #endif
661 C_UDMI(c,ct,FACE_X) = 0.;
662 C_UDMI(c,ct,FACE_Y) = 0.;
663 #if RP_3D
664 C_UDMI(c,ct,FACE_Z) = 0.;
665 #endif
666 C_UDMI(c,ct,WALL_HIT) = 0.;
667 C_UDMI(c,ct,DEP) = 0.;
668 }
669 end_c_loop_all(c,ct)
670 }
671 }
672
673
674 /* model for the Brownian motion */
675 DEFINE_DPM_BODY_FORCE(brownian_forceF,p,i)
676 {
677 real rho_p,p_dt,F;
678 real k,j,S,z1,z2,z3;
679 real lam,Cc,a,b,R,pi,p_abs,P,mu_f,T,Dp;
680
681 cell_t c=P_CELL(p);
682 Thread *t=P_CELL_THREAD(p);
683
684 rho_p=P_RHO(p); //tracked particle density
685 p_dt=P_DT(p); //tracked particle time step
686
687 P=C_P(c,t); //static pressure in the cell where the particle is located
688 T=C_T(c,t); //temperature in the cell where the particle is located
689 mu_f=C_MU_L(c,t); //density of the fluid in the cell where the particle is located
690 Dp=P_DIAM(p); //tracked particle diameter
691
692
693 /* Compute the Cunningham Correction factor*/
694 Cc=get_Cc(P,T,Dp, mu_f);
695
696
697 /* Implementation of Brownian diffusion model */

```



```

698 z1 = dpm_gauss_random(p); /* independent zero-mean Gaussian random number*/
699 z2 = dpm_gauss_random(p); /* independent zero-mean Gaussian random number*/
700 z3 = dpm_gauss_random(p); /* independent zero-mean Gaussian random number*/
701
702
703 if(P_TIME(p)==0.0) F = 0.0;
704 else
705 {
706 k = 216*mu_f*KB*T;
707 j = PI*pow(Dp,5)*pow(rho_p,2)*Cc*p_dt;
708
709 S = pow(k/j,0.5); /* [m/s^2] */
710     if (i==0) F =z1*S;
711     else if (i==1) F =z2*S;
712     else if (i==2) F =z3*S;
713 }
714
715 return(F); /* Return variable into DPM model as an acceleration in [m/s^2] */
716 }
717
718
719 /* modify the DPM model to do a user defined turbulent dispersion */
720 DEFINE_DPM_DRAG(dpm_stochastic_drag,Re,p)
721 {
722 cphase_state_t *c = &(p->cphase[0]); /* pointer to continuous phase properties, velocity etc.(dpm.h) */
723 real Vrel;
724 real dir = p->user[EDDY_DIR]; /* y-direction of the new eddy */
725 real drag_factor;
726 real CL = 0.2; /* For the core flow eddy_time */
727 /*-----*/
728 real fluent = 0; /* 0: TL_plus. 1: TL = CL k/eps */
729 /*-----*/
730 real k,eps,eplus,TL_plus = 1.0; /* dimensionless time scales */
731 real Y_plus_p = 200.0; /* dimensionless particle dist. */
732 cell_t c0 = RP_CELL(&(p->cCell)); /* index of cell in which currently tracked particle is in */
733 Thread *t0 = RP_THREAD(&(p->cCell)); /* cell thread to which above cell belongs */
734 real coeff;
735 cxboolean check_time = FALSE;
736 int dim = ND_ND; /* 2D - ND_ND = 2 */
737 real pv[3] = {0.,0.,0.}; /* particle velocity vector */
738 real pp[3] = {0.,0.,0.}; /* particle position vector */
739 real I[3] = {0.,0.,0.}; /* streamwise direction vector at particle location */
740 real J[3] = {0.,0.,0.}; /* wall normal vector */
741 real K[3] = {0.,0.,0.}; /* spanwise direction vector */
742 int i;
743 real Vprime_rms;
744 real Vprime_vec[3]; /* fluct. vel. vector */
745 real vel_fric; /* u_tauwall , frictional velocity */
746 real y_dist;
747 NV_V(pv, =, p->state.V); /* velocity of particle, x,y,z-coord. now stored in pv */
748 NV_V(pp, =, p->state.pos); /* position of particle, x,y,z-coord. now stored in pp*/
749 #if !INTERPOLATION
750 c->V[0] = C_U(c0,t0); /*x_vel*/
751 c->V[1] = C_V(c0,t0); /*y_vel*/
752 #if RP_3D
753 c->V[2] = C_W(c0,t0);
754 #endif
755 #endif /* INTERPOLATION */
756 #if !PARALLEL
757 update_interval_old = (int)RP_Get_Real("update_old");
758 update_interval_up = (int)RP_Get_Real("update_new");
759 yplus_thresh = RP_Get_Real("yplus_threshold");
760 dt_min = RP_Get_Real("delta_t_min");
761 te_min = RP_Get_Real("t_eddy_min");
762 #endif /* PARALLEL */
763 Y_plus_p = get_yplus_particle(c0,t0,pp);
764 /* CX_Message("Y_plus_p = %f, px = %f, py = %f, pz = %f\n",Y_plus_p,pp[0],pp[1],pp[2]); */
765 if(Y_plus_p < yplus_thresh && Y_plus_p > -0.1 )
766 {
767 do_stochastics = FALSE;
768 do_wall_stoch = TRUE;
769 }
770 else

```

```

771 {
772 do_stochastics = TRUE;
773 do_wall_stoch = FALSE;
774 if(p->user[1]<0.)
775 {
776 p->eddy_time=DPM_SMALL;
777 p->user[T_EDDY] = DPM_SMALL;
778 }}
779
780
781 /* Trap particle if closer than particle radius to the wall */
782 y_dist = Y_plus_p/sqrt(C_UDMI(c0,t0,TAU_WALL)*C_R(c0,t0))*C_MU_L(c0,t0);
783
784 #if roughness
785 real rough = 0.96e-6; /* k + sigma_k - e*/
786 #else
787 real rough = 0;
788 #endif
789
790 if(y_dist < (0.5*P_DIAM(p)+rough) && Y_plus_p > -0.1)
791 {
792     if (p->type==DPM_TYPE_INERT)
793     {
794         do_stochastics = FALSE;
795         do_wall_stoch = FALSE;
796         aborted = get_aborted();
797         C_UDMI(c0,t0,DEP) += 1.0;
798         CX_Message("particle_aborted_roughness_model:%i\n", aborted);
799         p->stream_index = -1;
800         return PATH_ABORT;
801     }
802     return PATH_ACTIVE;
803 }
804
805 #if RP_2D
806 if (rp_axi_swirl)
807 {
808     dim = 3;
809     pv[2] = p->state.V[2];
810 }
811 else
812 {
813     pv[2]=0;
814     pp[2]=0.;
815 }
816 #endif
817
818 real ruu = sqrt(C_RUU(c0,t0));
819 real rvv = sqrt(C_RVV(c0,t0));
820 real cu = C_U(c0,t0);
821 real cv = C_V(c0,t0);
822
823
824 if (0) /*msg_count%(update_interval_up)==0*/
825 {
826     CX_Message("Particle_Y+=%f,t_eddy=%g,dt=%g,pp_x=%g\n",Y_plus_p,
827 p->user[T_EDDY],P_DT(p), pp[0]);
828     CX_Message("NEW:u=%f,v=%f,u_rms=%f,v_rms=%f\n",cu,cv, ruu, rvv);
829     msg_count++;
830 }
831
832
833 /* Near-wall particle dispersion, y+ < 200 */
834 if (do_wall_stoch)
835 {
836     if (p->eddy_time <= DPM_SMALL) /*If the old eddy time is up: New discrete eddy. DPM_SMALL = 1e-9*/
837     {
838         check_time = TRUE;
839         p->user[N_EDDY] ++;
840         p->user[E_PLUS]=0.; /* reset interaction time */
841         p->user[MOD] = 0.; /* reset spurious drift correction term */
842         vel_fric = sqrt(C_UDMI(c0,t0,TAU_WALL)/C_R(c0,t0));
843

```

```

844 /*Generating the rms velocity fluctuations in the location of the particle*/
845 #if dns
846 get_rms_vel_fluc(Y_plus_p,vel_fric,Vprime_vec,I,J,K,c,c0,t0,check_time,dir);
847 #else
848 get_rms_vel_fluc(Y_plus_p,vel_fric,Vprime_vec,c0,t0);
849 #endif
850
851 p->user[EDDY_DIR] = C_UDMI(c0,t0,N_VEC_Y);
852
853 TL_plus = get_tl_plus(Y_plus_p); /* calc. dimensionless time scale based on particle y_plus*/
854 eplus = get_tl_plus(Y_plus_p);
855 real eps = C_D(c0,t0); /*dissipation*/
856
857 k = C_K(c0,t0); /*turbulence kinetic energy*/
858
859
860 /* calc. modified time scale */
861 if (fluent == 1.) p->eddy_time = CL*k/eps; /* FLUENT DEFINITION */
862 else p->eddy_time = TL_plus*C_MU_L(c0,t0)/C_UDMI(c0,t0,TAU_WALL); /* Lagrangian time scale made dimensional*/
863
864
865 if (random_eddy_lifetime)
866     p->eddy_time *= -log(uniform_random()); /* Eq. 23.2-32 User's Guide, characteristic eddy lifetime*/
867 else
868     p->eddy_time *=2.; /* Eq. 23.2-31 User's Guide, characteristic eddy lifetime */
869
870 if (p->state.time == 0.0000000) p->eddy_time *= dpm_uniform_random(p);
871 if (p->eddy_time < te_min) p->eddy_time = te_min; /* te_min = 4e-6 = komogorov scale*/
872 /*store eddy time*/
873 p->user[E_PLUS] = eplus; /* time scale constant */
874 p->user[T_EDDY] = p->eddy_time; /* store eddy lifetime */
875 p->user[Y_PLUS_P] = Y_plus_p;
876
877 /* New random fluctuations constant for t_eddy (LAMBDA1,2&3)*/
878 for (i=0; i<3; i++) p->user[LAMBDA1+i] = dpm_gauss_random(p);
879 /* New velocity fluctuation: Fluent definition of DRW */
880 for (i=0; i<3; i++) p->V_prime[i] = p->user[LAMBDA1+i] * Vprime_vec[i];
881
882 } /*END New discrete eddy*/
883 else
884 {
885 /*If the eddy is still alive, the eddy time, u', v' and w' are corrected according to the new location*/
886
887 check_time = FALSE;
888 /* Calc. the friction velocity in the particle position */
889 vel_fric = sqrt(C_UDMI(c0,t0,TAU_WALL)/C_R(c0,t0));
890
891 /*Generating the rms velocity fluctuations in the location of the particle*/
892 #if dns
893 get_rms_vel_fluc(Y_plus_p,vel_fric,Vprime_vec,I,J,K,c,c0,t0,check_time,dir);
894 #else
895 get_rms_vel_fluc(Y_plus_p,vel_fric,Vprime_vec,c0,t0);
896 #endif
897
898 /* Calc. the fluctuating velocity based on the generated rms velocity in this new location*/
899 for (i=0; i<3; i++) p->V_prime[i] = p->user[LAMBDA1+i] * Vprime_vec[i];
900
901 /* Generate the correction term for the modified DRW */
902 real Cc = get_Cc(C_P(c0,t0),C_T(c0,t0),P_DIAM(p), C_MU_L(c0,t0));
903 real tau_p = Cc*P_RHO(p)*pow(P_DIAM(p),2)/(18*C_MU_L(c0,t0));
904 real TL = get_tl_plus(Y_plus_p); /* TL_plus*/
905 TL = TL*C_MU_L(c0,t0)/C_UDMI(c0,t0,TAU_WALL); /* Dimensionalize */
906 real Stk = tau_p/TL;
907 real nu = C_MU_L(c0,t0)/C_R(c0,t0);
908
909 real correction_direction = C_UDMI(c0,t0,N_VEC_Y);
910
911 real new_correction = get_correction(Y_plus_p,vel_fric, Stk, nu, TL, P_DT(p), correction_direction, c0, t0);
912
913 p->user[MOD] += new_correction;
914 p->V_prime[1] += p->user[MOD];
915
916

```

```

917 if (fluent == 1.)
918 {
919     p->eddy_time *= (p->old_ted/p->old_tke) * (C_K(c0,t0)/C_D(c0,t0));
920 }
921 else
922 {
923     /* tau_e is updated based on the particle location at each time step (Mofakham and Ahmadi, 2020) */
924     TL_plus = get_tl_plus(Y_plus_p);
925     p->eddy_time *= TL_plus/p->user[E_PLUS];
926     p->user[E_PLUS] = TL_plus;
927 }
928 }
929 }
930 msg_count++;
931
932 /* add the fluctuating vel. to mean cont. phase vel*/
933 for (i=0; i<dim; i++) c->V[i] += p->V_prime[i];
934 } /* End do_wall_stoch */
935
936
937
938
939
940 /* standard stochastic tracking outside of y+ = 200*/
941
942 if (do_stochastics)
943 {
944     p->user[MOD] = 0.;
945
946     if (p->eddy_time <= DPM_SMALL) /*New discrete eddy*/
947     {
948         check_time = TRUE;
949         p->user[9]++; /*Number of eddies*/
950
951         /* Eq. 23.2-23 User's Guide, fluid Lagrangian integral time */
952         p->eddy_time = CL * C_K(c0,t0)/ C_D(c0,t0);
953
954         /* This needs to be defined, else p->eddy_time --> inf */
955         p->user[E_PLUS] = p->eddy_time*C_UDMI(c0,t0,TAU_WALL)/C_MU_L(c0,t0);
956
957         /*p->eddy_time = 70* C_MU_L(c0,t0)/C_UDMI(c0,t0,TAU_WALL);*/
958         if (random_eddy_lifetime)
959         p->eddy_time *= -log(uniform_random()); /* Eq. 23.2-32 User's Guide, characteristic eddy lifetime */
960     else
961     p->eddy_time *=2.; /* Eq. 23.2-31 User's Guide, characteristic eddy lifetime */
962     if (p->state.time == 0.0000000) p->eddy_time *= dpm_uniform_random(p);
963     if (p->eddy_time < te_min) p->eddy_time = te_min;
964
965     /* velocity fluctuations are calculated using a Gaussian deviate random number */
966     if (sg_rsm) /*WHAT VARIABLE IS SG_RSM? Presumably, if rsm-turb model*/
967     {
968         real chc11=0.;
969         real chc22=0., chc33=0.;
970         chc11 = sqrt(C_RUU(c0,t0));
971         chc22 = sqrt(C_RVV(c0,t0));
972         chc33 = sqrt(C_RWW(c0,t0));
973
974         /*independent zero-mean Gaussian random number */
975         for (i=0; i<3; i++) p->user[LAMBDA1+i] = dpm_gauss_random(p);
976         p->V_prime[0] = p->user[LAMBDA1] * chc11;
977         p->V_prime[1] = p->user[LAMBDA2] * chc22;
978         p->V_prime[2] = p->user[LAMBDA3] * chc33;
979
980     }
981     else /* if k-omega SST */
982     {
983         Vprime_rms = sqrt(2./3. * C_K(c0,t0)); /* Eq. 23.2.27 User's Guide, RMS fluctuating components */
984
985         /* Eq. 23.2.28-30 User's Guide, velocity fluctuations */
986         for (i=0; i<3; i++) p->V_prime[i] = dpm_gauss_random(p) * Vprime_rms;
987     }
988 } /* END new eddy */
989 else

```

```

990 {
991
992 /* If the eddy is still alive: */
993 /* rescale the remaining portion of eddy life time and rms values */
994
995 /* CORRECTION TO P->EDDY_TIME */
996 /* TL_plus is not valid for y+ > y+_tresh = 200*/
997 if (msg_count%(update_interval_old)==0)
998 {
999   CX_Message("tke,%e, p->old_tke,%e, eddy_time,%e\n", C_K(c0,t0), p->old_tke, p->eddy_time);
1000 }
1001 p->eddy_time *= (p->old_ted/p->old_tke) * (C_K(c0,t0)/C_D(c0,t0));
1002
1003 if (sg_rsm) /*If the rsm turbulence model is employed*/
1004 {
1005   real chc11=0.;
1006   real chc22=0., chc33=0.;
1007   chc11 = sqrt(C_RUU(c0,t0));
1008   chc22 = sqrt(C_RVV(c0,t0));
1009   chc33 = sqrt(C_RWW(c0,t0));
1010
1011   p->V_prime[0] = p->user[LAMBDA1] * chc11;
1012   p->V_prime[1] = p->user[LAMBDA2] * chc22;
1013   p->V_prime[2] = p->user[LAMBDA3] * chc33;
1014 }
1015 else
1016 {
1017   for (i=0;i<dim;i++) p->V_prime[i] *= sqrt(C_K(c0,t0)/p->old_tke);
1018 }
1019
1020 check_time = FALSE;
1021
1022 } /* END old eddy */
1023
1024 for (i=0; i<dim; i++) c->V[i] += p->V_prime[i];/* add fluctuating vel. to mean cont. phase vel*/
1025
1026
1027 } /* END do_stochastics */
1028
1029
1030 p->old_ted = C_D(c0,t0);
1031 p->old_tke = C_K(c0,t0);
1032
1033 /* c->V[i] is the new fluid velocity, including the instantaneous velocity fluctuations*/
1034 Vrel = 0.0;
1035 for (i=0; i<dim; i++)
1036 Vrel += SQR(c->V[i]-pv[i]);
1037
1038 /* The new relative velocity, which the drag has to take into account */
1039 Vrel = sqrt(Vrel);
1040
1041 /* New particle Reynolds number, taking the new Vrel into account*/
1042 p->Re = c->rho * P_DIAM(p) * Vrel / c->mu;
1043
1044 /* Defining variables to be used*/
1045 real Cd,Cc;
1046 Cc = get_Cc(C_P(c0,t0),C_T(c0,t0),P_DIAM(p), C_MU_L(c0,t0));
1047
1048 /*Shiller and Neumann correlation from Crowe et al. 2006 and Stokes-drag*/
1049 if (p->Re > 1) Cd = 24.0/(p->Re*Cc)*(1.0+0.15*pow(p->Re,0.687));
1050 else Cd = 24.0/(p->Re*Cc);
1051
1052 /* the DPM_DRAG macro requires to return in the following form (18 Cd Re)/24 */
1053 coeff =(18.0*Cd*p->Re/24.0); /* Return variable into DPM model*/
1054
1055 real tau_p = Cc*P_RHO(p)*pow(P_DIAM(p),2.)/(18.*C_MU_L(c0,t0));
1056 if (P_DIAM(p) != 0.0)
1057 drag_factor = coeff * c->mu / ( P_RHO(p) * P_DIAM(p) * P_DIAM(p));
1058 else
1059 drag_factor = 1.;
1060
1061
1062 if (check_time && (do_stochastics||do_wall_stoch) ) /* !!! */

```

```

1063 {
1064
1065 /* limit the eddy_time by the eddy crossing time too */
1066
1067 /* From Ahmadi: On random walk models for simulation of particle-laden turbulent flows */
1068 real Le = p->eddy_time*pow(2*C_K(c0,t0)/3,0.5);
1069 real t_R = -tau_p*log(1. - Le/(Vrel*tau_p));
1070
1071 if (Le < Vrel*tau_p)
1072 p->eddy_time = MIN(p->eddy_time,t_R); /* Eq. 23.2.33 User's Guide, particle eddy crossing time */
1073
1074 if (msg_count%(update_interval)==0)
1075 {
1076 CX_Message("t_R=%g,tau_e=%g,Cc=%g\n", t_R, p->eddy_time, Cc);
1077 msg_count++;
1078 }
1079
1080 }
1081 return coeff;
1082 }
1083
1084 /* name particle scalars for post-processing */
1085 DEFINE_DPM_SCALAR_UPDATE(dpm_sc_interact,cell,thread,initialize,p)
1086 {
1087 cell_t c = RP_CELL(&p->cCell); /* Get Cell and Thread from */
1088 Thread *t = RP_THREAD(&p->cCell); /* Particle Structure using new macros*/
1089 real pp[3] = {0.,0.,0.}; /* particle position vector */
1090 NV_V(pp, =, p->state.pos); /* position of particle, x,y,z-coord. */
1091 if (initialize)
1092 {
1093 /* this is the initialization call */
1094 p->user[E_PLUS] = 0.; /* e_plus */
1095 p->user[T_EDDY] = 0.; /* eddy lifetime */
1096 p->user[Y_PLUS_P] = get_yplus_particle(c,t,pp); /* y_plus value at particle location */
1097 p->user[LAMBDA1] = dpm_gauss_random(p);
1098 p->user[LAMBDA2] = dpm_gauss_random(p);
1099 p->user[LAMBDA3] = dpm_gauss_random(p);
1100 p->user[N_EDDY] = 0.; /* number of eddies */
1101 p->user[EDDY_DIR] = 0.; /* direction of the eddy */
1102 p->user[MOD] = 0.; /* memory of correction term */
1103 strcpy(user_particle_vars[E_PLUS].name,"e_plus");
1104 strcpy(user_particle_vars[E_PLUS].label,"e_Plus");
1105 strcpy(user_particle_vars[T_EDDY].name,"t_eddy");
1106 strcpy(user_particle_vars[T_EDDY].label,"t_Eddy");
1107 strcpy(user_particle_vars[Y_PLUS_P].name,"y_plus");
1108 strcpy(user_particle_vars[Y_PLUS_P].label,"Y_Plus");
1109 strcpy(user_particle_vars[LAMBDA1].name,"lambda_1");
1110 strcpy(user_particle_vars[LAMBDA1].label,"Lambda_1");
1111 strcpy(user_particle_vars[LAMBDA2].name,"lambda_2");
1112 strcpy(user_particle_vars[LAMBDA2].label,"Lambda_2");
1113 strcpy(user_particle_vars[LAMBDA3].name,"lambda_3");
1114 strcpy(user_particle_vars[LAMBDA3].label,"Lambda_3");
1115 strcpy(user_particle_vars[N_EDDY].name,"n_eddy");
1116 strcpy(user_particle_vars[N_EDDY].label,"N_Eddy");
1117 strcpy(user_particle_vars[EDDY_DIR].name,"eddy_dir");
1118 strcpy(user_particle_vars[EDDY_DIR].label,"Eddy_Dir");
1119 strcpy(user_particle_vars[MOD].name,"mod");
1120 strcpy(user_particle_vars[MOD].label,"Mod");
1121
1122 }
1123 else
1124 {
1125 /* not needed */
1126 }
1127 }
1128
1129 /* The particle trajectory integration time step size in the DPM can be controlled
1130 * by activating the following Fluent macro */
1131 DEFINE_DPM_TIMESTEP(dpm_ts_by_eddy_time,p, dt)
1132 {
1133
1134 cell_t c0 = RP_CELL(&(p->cCell)); /* index of cell in which currently tracked particle is in */
1135 Thread *t0 = RP_THREAD(&(p->cCell)); /* cell thread to which above cell belongs */

```

```

1136
1137 real Cc = get_Cc(C_P(c0,t0),C_T(c0,t0),P_DIAM(p), C_MU_L(c0,t0));
1138 real tau_p = Cc*P_RHO(p)*pow(P_DIAM(p),2.)/(18.*C_MU_L(c0,t0)); /* particle relaxation time */
1139
1140     if (dt > tau_p/2.)
1141     {
1142         return tau_p/2.;
1143     }
1144 return dt;
1145 }
1146
1147 /* User-defined function for initiating the particles with the velocity and temperature similar
1148 * to the fluid flow at the particle location. */
1149 DEFINE_DPM_INJECTION_INIT(init_particles, I)
1150 {
1151     Particle *p;
1152     loop (p,I->p)
1153     {
1154         cell_t c=P_CELL(p);
1155         Thread *t=P_CELL_THREAD(p);
1156         P_VEL(p)[0]=C_U(c,t); /* Velocity in x direction [0]*/
1157         P_VEL(p)[1]=0; /* Vel. in y dir. */
1158         P_T(p)=C_T(c,t);
1159     }
1160 }
1161 }
1162
1163
1164 /* User-defined capture boundary condition on walls for DPM with UDM location
1165 * The function is executed every time a particle touches a boundary of the domain*/
1166 DEFINE_DPM_BC(bc_capture, p, t, f, f_normal, dim)
1167 {
1168     int hit=0;
1169     if (p->type==DPM_TYPE_INERT)
1170     {
1171         if (((NNULLP(t)) && (THREAD_TYPE(t) == THREAD_F_WALL)))
1172         {
1173             Thread * tread_cell=P_CELL_THREAD(p);
1174             cell_t c=P_CELL(p);
1175             C_UDMI(c,tread_cell,DEP) += 1.0;
1176             return PATH_ABORT;
1177         }
1178     }
1179 }
1180 return PATH_ACTIVE;
1181 }
1182
1183 /* User-defined boundary condition for particles leaving domain and mark position of impact
1184 * DPM boundary condition at outlet for generating concentration profiles */
1185 DEFINE_DPM_BC(bc_escape,p,t,f,f_normal,dim)
1186 {
1187     cell_t c0;
1188     Thread *ct0; /*adjacent cell thread */
1189     c0 = F_C0(f,t);
1190     ct0 = THREAD_T0(t);
1191     C_UDMI(c0,ct0,WALL_HIT)++; /* mark cell as particle-containing*/
1192     F_UDMI(f,t,WALL_HIT)++; /* mark cell as particle-containing*/
1193     /* complete deposition, particles being removed from domain*/
1194     if(1)
1195     {
1196         p->stream_index = -1;
1197         p->gvtp.n_escaped++;
1198         return PATH_END;
1199     }
1200     return PATH_ABORT;
1201 }

```


NTNU	Hazardous activity identification process			Prepared by	Number	Date
				HSE section	HMSRV/2601E	09.01.2013
HSE				Approved by The Rector		Replaces 01.12.2006

Unit: (Department) **Department of Energy and Process Engineering** Date: **11.06.2021**
 Line manager:

Participants in the identification process (including their function): Silje Bordvik(PhD Candidate), Tarjei Vefring Stordal (student)
 Short description of the main activity/main process: Master project for student: Tarjei Vefring Stordal. Particle Deposition From Geothermal Supercritical Steam

Is the project work purely theoretical? (YES/NO): NO
 Answer "YES" implies that supervisor is assured that no activities requiring risk assessment are involved in the work. If YES, briefly describe the activities below. The risk assessment form need not be filled out.

Signatures: Responsible supervisor: *Erling Naess* Student: *Tarjei V Stordal*

ID nr.	Activity/process	Responsible person	Existing documentation	Existing safety measures	Laws, regulations etc.	Comment
1	Experimental investigation of silica deposition from pressurised superheated steam. Location: IFE (institute for energy technology)	Silje Bordvik, Morten Tjelta (IFE)	Provided by IFE	Provided by IFE	Provided by IFE	

NTNU		Prepared by		Number		Date	
		HSE section		HMSRV2603E		04.02.2011	
HSE/KS		Approved by				Replaces	
		The Rector				01.12.2006	

Risk assessment

Unit: (Department) **Department of Energy and Process Engineering**

Date: **11.06.2021**

Line manager:

Participants in the identification process (including their function): Sijje Bordvik(PhD Candidate), Tarjei Vefring Stordal (student)

Short description of the main activity/main process: Master project for student: Tarjei Vefring Stordal. *Particle Deposition From Geothermal Supercritical Steam*

Signatures: Responsible supervisor: *Sally Naess* Student: *Tarjei V Stordal*

Activity from the identification process form	Potential undesirable incident/strain	Likelihood (1-5)	Consequence:			Risk Value (human)	Comments/status Suggested measures
			Human (A-E)	Environment (A-E)	Economy/material (A-E)		
Experimental investigation of silica deposition from pressurised superheated steam.	Heat/burn	2	B	A	A	B2	Actions: PPE, isolation Safety measures: Wear gloves when handling the rig. Protective glasses required at the lab.
	Mechanical failure in the highly pressurised autoclave	1	C	A	D	C1	Actions: PPE, call emergency services Safety measures: Protective glasses required at the lab. IFE-property-equipment.
	Leakage of supercritical steam	2	A	A	A	A1	Actions: PPE, isolation Safety measures: Wear gloves when handling the rig. Protective glasses required at the lab. Low consequences due to low steam volumes in the rig.

Likelihood, e.g.:

1. Minimal
2. Low
3. Medium
4. High
5. Very high

Consequence, e.g.:

- A. Safe
- B. Relatively safe
- C. Dangerous
- D. Critical
- E. Very critical

Risk value (each one to be estimated separately):

$$\text{Human} = \text{Likelihood} \times \text{Human Consequence}$$

$$\text{Environmental} = \text{Likelihood} \times \text{Environmental consequence}$$

$$\text{Financial/material} = \text{Likelihood} \times \text{Consequence for Economy/material}$$

NTNU		Prepared by		Number	Date
		HSE section		HMSRV/2603E	04.02.2011
HSE/KS		Approved by			Replaces
		The Rector			01.12.2006
Risk assessment					
					

Potential undesirable incident/strain

Identify possible incidents and conditions that may lead to situations that pose a hazard to people, the environment and any materiel/equipment involved.

Criteria for the assessment of likelihood and consequence in relation to fieldwork

Each activity is assessed according to a worst-case scenario. Likelihood and consequence are to be assessed separately for each potential undesirable incident. Before starting on the quantification, the participants should agree what they understand by the assessment criteria:

Likelihood

Minimal 1	Low 2	Medium 3	High 4	Very high 5
Once every 50 years or less	Once every 10 years or less	Once a year or less	Once a month or less	Once a week

Consequence

Grading	Human	Environment	Financial/material
E Very critical	May produce fatality/ies	Very prolonged, non-reversible damage	Shutdown of work >1 year.
D Critical	Permanent injury, may produce serious health damage/sickness	Prolonged damage. Long recovery time.	Shutdown of work 0.5-1 year.
C Dangerous	Serious personal injury	Minor damage. Long recovery time	Shutdown of work < 1 month
B Relatively safe	Injury that requires medical treatment	Minor damage. Short recovery time	Shutdown of work < 1week
A Safe	Injury that requires first aid	Insignificant damage. Short recovery time	Shutdown of work < 1day


The unit makes its own decision as to whether opting to fill in or not consequences for economy/materiel, for example if the unit is going to use particularly valuable equipment. It is up to the individual unit to choose the assessment criteria for this column.

Risk = Likelihood x Consequence

Please calculate the risk value for "Human", "Environment" and, if chosen, "Economy/materiel", separately.

About the column "Comments/status, suggested preventative and corrective measures":

Measures can impact on both likelihood and consequences. Prioritise measures that can prevent the incident from occurring; in other words, likelihood-reducing measures are to be prioritised above greater emergency preparedness, i.e. consequence-reducing measures.

NTNU		Risk matrix		Date	
		HSE/KS		8 March 2010	
		prepared by		Number	
		HSE Section		HMSRV2604	
		approved by		Page	
		Rector		4 of 4	
				Replaces	
				9 February 2010	



MATRIX FOR RISK ASSESSMENTS at NTNU

		E1	E2	E3	E4	E5
Extremely serious						
Serious		D1	D2	D3	D4	D5
Moderate		C1	C2	C3	C4	C5
Minor		B1	B2	B3	B4	B5
Not significant		A1	A2	A3	A4	A5
		Very low	Low	Medium	High	Very high
		LIKELIHOOD				
CONSEQUENCE						

Principle for acceptance criteria. Explanation of the colours used in the risk matrix.

Colour	Description
Red	Unacceptable risk. Measures must be taken to reduce the risk.
Yellow	Assessment range. Measures must be considered.
Green	Acceptable risk Measures can be considered based on other considerations.

